Laser-engraved Wearable Sweat Sensor for Metabolic Monitoring

Thesis by

Yiran Yang

In Partial Fulfillment of the Requirements for

the Degree of

Doctor of Philosophy

CALIFORNIA INSTITUTE OF TECHNOLOGY

Pasadena, California

2023

(Defended January 17, 2023)

Yiran Yang
ORCID: 0000-0001-8770-8746

ACKNOWLEDGEMENTS

The past five years at Caltech have been a wonderful and extraordinary period of my life. The PhD "struggle-bus" has been exciting and full of physical, mental and intellectual challenges that made me a better person. It is also impossible to get to the end of this journey without support and help from many people at Caltech and beyond, and I will try my best to share my gratitude here or elsewhere in the event of any omissions.

This journey would not have been possible without my advisor, Wei Gao. When I first arrived on campus in Fall 2017, Wei just settled down in the Steele lab with a "temporary" office and the empty "temporary" lab space. The first conversation we had was full of excitement and he became my "tour guide" of this PhD journey. Even though I knew literally nothing at the beginning, Wei has been always a patient mentor in my research experiments and writings, showing me not only "what/how to do" in skills but also the "why/when to do" mindset. Wei was also very open-minded and supportive through my "side-gig" as a safety office/lab manager, and I really appreciate that I have gained much better communication skills within and beyond research through my time in Gao Lab.

I would also like to thank my colleagues in the Gao Lab. I would like to thank Here I would like to thank Dr. Yu Song, Dr. Xiangjie Bo, Dr. Minqiang Wang, and Jihong Min for being such great team members to co-lead our projects to the great fruition. I would like to thank Dr. You Yu, Dr. Zhiguang Wu, Dr. Joanna Nassar and Dr. Rebeca M. Torrente-Rodríguez for their mentoring and advice in my early PhD life. I would like to thank my mentees Adam Kogan, Chibuike Uwakwe, and Soyoung Shin who always offer me a new perspective looking at research problems. I would like to thank many other friends in the lab for their help and support in research and beyond.

Furthermore, I would like to thank my other thesis committee members, Prof. Yu-Chong Tai, Prof. Morteza Gharib and Prof. Azita Emami for guiding me through the process. I would like to thank Prof. Tai especially for introducing me to Wei when I first arrived at Caltech in Fall 2017 and teaching us MedE students how to ask and answer important questions when approaching a problem.

Moreover, I would like to thank staff at Caltech who provided me with tremendous support. Thank you to Dr. Nathan Dalleska for always helping me set up the HPLC/ GC-MS analyses. Thank you to all Caltech KNI staff for training me on the sophisticated tools. Thank you to Katie Pichotta for always giving me advice when I encountered problems in lab/research logistics. Thank you to Department of Medical Engineering and especially Christine Garske for always keeping us along with the awesome social events.

Outside Caltech, I would like to thank my project collaborators Dr. Tzung K. Hsiai, Dr. Zhaoping Li, and Dr. Jeannine S. McCune who provided us with so much support and advice on our human studies. I would also like to thank mentors and professors back in Houston who led me into the world of scientific research including Dr. Tomasz Tkaczyk, Dr. Michal Pawlowski, Dr. Janet Braam, Dr. John Liu, Dr. Bin Wang and Dr. Dan Su.

Thank you to my parents for always supporting me to ensure me with the best education possible both in school and beyond. Thank you to my distant family who always cheered me up these years. I want to thank Zi Wang for the continual support and love over the past 5 years.

ABSTRACT

Wearable sensors have shown great potential in health diagnostics and monitoring. Continuous monitoring of metabolites in sweat could potentially offer great insight into a person's health, but current sweat sensing technology faces challenges in different realms: The sensing strategies are limited and there is a need to achieve high sensitivity for low-concentration targets and widen the detection spectrum of chemical targets. The lack of efficient sweat sampling creates inaccurate sensing results from sweat mixing with skin contaminants or sensing byproducts. Moreover, the lack of evaluation of sweat metabolites with respect to relevant clinical conditions and the lack of scalable fabrication technique pose hurdles in the eventual applications of non-invasive sweat monitoring. In this thesis, efforts advancing progress in these fronts are presented. Chapter 1 establishes a brief topical overview of the sweat-sensing background. In Chapter 2, we demonstrate how to utilize laser-engraving technique to achieve high-performance graphene sensors for electroactive metabolite sensing and vital signs detection. Chapter 3 describes subsequent efforts built on laser-engraved graphene sensors to improve sensing selectivity and widen the detection spectrum to detect non-electroactive targets in sweat. In Chapter 4, design and performance of our laser-engraved microfluidics are described and shown to improve sweat sampling in both exercise-induced and iontophoresis-induced sweating individuals. Chapter 5 presents our endeavors in evaluating sweat biomarkers with clinical conditions in pilot studies involving individuals with gout and metabolic syndrome. In total, the works summarized here expand biology, chemistry, material science, and mechanical engineering, and could potentially facilitate future applications in precision nutrition.

PUBLISHED CONTENT AND CONTRIBUTIONS

1. Yang, Y.; Gao, W. Wearable and flexible electronics for continuous molecular monitoring. *Chemical Society Reviews* **48**, 1465–1491 (2019). https://doi.org/10.1039/C7CS00730B.

Y.Y. and W.G. prepared the manuscript and the figures.

2. Wang, M.; Yang, Y.; Gao, W. Laser-engraved graphene for flexible and wearable electronics. *Trends in Chemistry* **3**, 969–981 (2021). https://doi.org/10.1016/j.trechm.2021.09.001.

M.W., Y.Y., and W.G. prepared the manuscript. M. W. prepared the figures.

3. Yang, Y.; Song, Y.; Bo, X.; Min, J.; Pak, O. S.; Zhu, L.; Wang, M.; Tu, J.; Kogan, A.; Zhang, H.; Hsiai, T. K.; Li, Z.; Gao, W. A laser-engraved wearable sensor for sensitive detection of uric acid and tyrosine in sweat. *Nature Biotechnology* **38**, 217–224 (2020). https://doi.org/10.1038/s41587-019-0321-x.

W.G. and Y.Y. initiated the concept. W.G., Y.Y., Y.S., X.B., T.K.H., and Z.L. designed the experiments; Y.Y., Y.S., X.B., and J.M. led the experiments and collected the overall data; O.S.P., L.Z., and Y.Y. performed the flow simulation and modeling; J.M. performed the circuit design and test; M.W., J.T., and A.K. contributed to sensor characterization and validation; W.G., Y.Y., Y.S., X.B., J.M., O.S.P., L.Z., and H.Z. contributed the data analysis and co-wrote the paper. All authors provided the feedback on the manuscript. Y.Y., Y.S., X.B. contributed equally to this work.

4. Wang, M.; Yang, Y.; Min, J.; Song, Y.; Tu, J.; Mukasa, D.; Ye, C.; Xu, C.; Heflin, N.; McCune, J. S.; Hsiai, T. K.; Li, Z.; Gao, W. A wearable electrochemical biosensor for the monitoring of metabolites and nutrients. *Nature Biomedical Engineering* 1–11 (2022). https://doi.org/10.1038/s41551-022-00916-z.

W.G., M.W., Y.Y., and J.M. initiated the concept and designed the studies; W.G. supervised the work; M.W., Y.Y., and J.M. led the experiments and collected the overall data; Y.S., J.T., D.M., C.Y., and C.X. contributed to sensor characterization, validation and sample analysis; N.H. contributed to the signal processing and app development. J.S.M., T.K.H. and Z.L. contributed to the design of the human studies. W.G., M.W., Y.Y., and J.M. co-wrote the paper. All authors contributed to the data analysis and provided feedback on the manuscript. M.W., Y.Y., and J.M. contributed equally to this work.

5. Min, J.; Tu, J.; Xu, C.; Lukas, H.; Shin, S.; Yang, Y.; Solomon, S.; Mukasa, D.; Gao, W. Skin-interfaced wearable sweat sensors for precision medicine. *Chemical Reviews*, *Manuscript Submitted.*

All authors prepared the figures and prepared the manuscript.

TABLE OF CONTENTS

LIST OF ILLUSTRATIONS AND/OR TABLES

Table Number *Page*

ABBREVIATIONS

°C	degrees Celsius
3D	three-dimension(al)
AA	amino acids
ABS	acetate buffer saline
AChE	acetylcholinesterase
AQCA	anthraquinone-2-carboxylic acid
BCAA	branched-chained amino acid(s)
BMI	body mass index
BSA	bovine serum albumin
cAMP	Cyclic adenosine monophosphate
CE	counter electrode
COVID-19	corona virus disease 2019
CS	chemical sensor(s)
CV	cyclic voltammetry
CVD	cardiovascular diseases
DNA	deoxyribonucleic acid
DPV	differential pulse voltammetry
FDA	food and drug administration
FPCB	flexible printed circuit board
GC-MS	gas chromatography mass spectrometry
His	histidine

HPLC	high performance liquid chromatography
HR	heart rate
ILE	isoleucine
IR	infrared (wavelength range)
IRB	Institutional Review Board
IS	internal standard
IT	single-potential amperometry
LEG	laser-engraved graphene
Leu	leucine
LSV	linear sweeping voltammetry
Lys	lysine
MB	methylene blue
Met	methionine
MIP	molecularly imprinted polymer
NIP	non-imprinted polymer
NP	nanoparticle
NutriTrek	name of our nutritional monitoring device
PB	Prussian Blue
PBS	phosphate buffer saline
PCB	printed circuit board
PET	polyethylene terephthalate
Phe	phenylalanine

PI	polyimide
PPI	points per inch
PS	physical sensor(s)
RAR	redox-active nanoreporter(s)
RE	reference electrode
RR	respiration rate
RNA	ribonucleic acid
SAR	sudomotor axon reflex
SEM	scanning electron microscopy
TEM	transmission electron microscopy
Thr	threonine
Trp	tryptophan
Tyr	tyrosine
T2DM	Type 2 Diabetes Mellitus
UA	uric acid
UV	ultraviolet (wavelength range)
Val	valine
VB	vitamin B
VC	vitamin C
VD	vitamin D
VE	vitamin E
WE	working electrode

w/w	weight/weight ratio

Chapter 1

INTRODUCTION

Materials from this chapter appear in "Yang, Y.; Gao, W. Wearable and flexible electronics for continuous molecular monitoring. *Chemical Society Reviews* 48, 1465–1491 (2019) doi:10.1039/C7CS00730B" and "Min, J.; Tu, J.; Xu, C.; Lukas, H.; Shin, S.; Yang, Y.; Solomon, S.; Mukasa, D.; Gao, W. Skin-interfaced wearable sweat sensors for precision medicine. *Chemical Reviews*, Manuscript Submitted."

1.1 Wearable Chemical Sensors

The increasing research interest in personalized medicine — an innovative approach harnessing biomedical devices to deliver tailored diagnostics and therapeutics according to the individual characteristics of each patient — promises to revolutionize traditional medical practices.[1,2] This presents a tremendous opportunity for developing wearable devices toward predictive analytics and treatment. On the other hand, the Internet of Things (IoT) — sensors and actuators connected by networks— has received enormous attention in the past decade.[3] The IoT is expected to revolutionize future medicine by enabling highly personalized and accessible healthcare and will have an economic impact on the healthcare of over 1 trillion dollars in 2020.[3] As healthcare cost and the world's aging population increase, there has been a need for personalized wearable devices to continuously monitor the health status of patients while patients are out of hospital. In this case, wearable biosensors can sample physiological signals conveniently and noninvasively, and thus provide sufficient information for health monitoring and even preliminary medical diagnosis.[4–6]

Flexible electronics could serve as an ideal platform for personalized wearable devices, thanks to their unique properties such as light weight, high flexibility and great conformability.[7–10] In the past decade, wearable and flexible sensors have been demonstrated for tracking conventional physical signals continuously in real time, such as body motion, blood pressure, body and skin temperature, heart rate as well as electrophysiological activities including EEG (electroencephalography), ECG (electrocardiography) and EMG (electromyography).[11–15] However, the commercially available wearable devices at present fail to provide more insightful information on users' health state at the molecular level. Biomarkers from the human body fluids, molecules that can be objectively measured and evaluated as indicators of normal or disease processes, can provide a dynamic and powerful access to understand a broad spectrum of health conditions, and will aid in the prediction, screening, diagnosis and therapy of diseases.[16] However, many studies

using biomarkers never achieve their full potential due to the lack of continuous monitoring technologies that could identify the roles of biomarkers in a timely manner. The instantaneous and continuous detection of relevant biomarkers in the human body using wearable chemical sensors can provide more in-depth personal healthcare monitoring and medical diagnosis, as compared to the detection of physical activities and vital signs. The limited availability of wearable chemical sensors has hindered further progress towards continuous personalized health monitoring.

According to the International Union of Pure and Applied Chemistry (IUPAC), a chemical sensor is "a device that transforms chemical information, ranging from the concentration of a specific sample component to total composition analysis, into an analytically useful signal".[17] A typical chemical sensor usually consists of a recognition element (receptor) and a physicochemical transducer. The function of the receptor is to provide high selectivity towards the target analyte in the presence of potentially interfering chemicals while the transducer is the key component that converts the chemical information to a measurable analytical signal. Wearable and flexible chemical sensors could be used as attractive alternatives to the bulky and expensive analytical instruments used in the healthcare sector. In traditional clinical settings, urine and blood samples are routinely analyzed through standard analytical techniques, which are expensive, time-consuming and unable to provide continuous measurements of the concentration of an analyte of interest. In addition, although the current gold-standard fluid for diagnostics is blood, it requires invasive sampling that poses a major hurdle and is unsuitable for long-term continuous use. Recognizing the significance of non-invasive wearable and flexible sensors for continuous molecular monitoring, researchers have focused tremendous effort on wearable and flexible techniques that can sample and analyze the major electrolytes, metabolites, heavy metals, and toxic gases directly in alternative body fluids, such as sweat, tears, interstitial fluid and saliva, as well as exhaustion breath, particularly in the past 5 years; researchers have also developed wearable epidermal sensors that can monitor wound healing (**Fig. 1-1**). The transition from blood to other body

fluids and breath provides a noninvasive means of in situ sensing, which is more attractive toward continuous health monitoring in daily life. Based on the transduction technique, the wearable and flexible chemical sensors are mainly either electrochemical or optical in nature.

Figure 1-1. Wearable and flexible chemical sensors for non-invasive health monitoring.

At present, electrochemical biosensing is the most common wearable and flexible sensing strategy owing to its unique advantages of sensor miniaturization, high sensitivity and label-free direct measurement.[18,19] Some classic examples of electrochemical sensors have been developed and demonstrated on wearable or flexible platforms over the years: (1) amperometric sensors. Amperometric sensors measure current generated from the oxidation or reduction of an electroactive analyte in a chemical reaction. Enzymatic amperometric sensors have been used for continuous monitoring of glucose, lactate, ethanol and uric acid, where chemical reactions of the target metabolite catalyzed by a specific enzyme (e.g. glucose oxidase, lactate oxidase and urate oxidase) generate electrical current proportional to the target concentration. (2) Potentiometric sensors. Potentiometry is usually defined as a zero-current technique that measures the potential appearing between the working electrode and the reference electrode in an electrochemical cell.[20] The

ion selective electrode based potentiometric sensors have been widely used for selective ion quantification.[21] They usually contain a permselective membrane where the target ions interact with the corresponding ionophore (e.g. a sodium ionophore X for Na^+, valinomycin for K^+ and a calcium ionophore ETH 129 for Ca^{2+})in the sensing membrane and cause voltage changes. For potentiometric sensors, the relationship between the analyte concentration and voltage output can be described by the Nernst equation: $E = RT/zF \bullet \ln(A/A_1) = \text{const} + S \bullet \log(A)$, where A and A_1 are ion activities/concentrations outside and inside the membrane, z is the charge of the ion, and S is the sensor sensitivity. For sodium or potassium sensing at room temperature, theoretically an ion selective sensor should have a sensitivity of 59.16 mV per decade of concentration. (3) Voltammetric sensors. Voltammetry is a very versatile and well-explored electroanalytical method and a transduction principle for deriving information about one or multiple analytes dynamically by measuring the current as a function of the varied potential. For example, stripping voltammetry is suitable for monitoring the heavy metals in body fluids.[22] (4) Electrochemical biosensors including affinity-based immunosensors and DNA sensors which have widely been used for analyzing proteins, peptides and DNAs/RNAs.

1.2 Sweat Sensors

Sweat is a very important body fluid that contains rich information about our physiological state. The wide distribution of sweat glands in the human body and the abundant biochemical compounds in sweat have made sweat a feasible and ideal biofluid for non-invasive biosensing.[23,24] Eccrine sweat, which is easily accessible non-invasively, is excreted directly onto the surface of the skin and is composed of water and various electrolytes (e.g. sodium, potassium, calcium, and chloride), nitrogenous compounds (e.g. urea and amino acids), and metabolites such as glucose, lactate and uric acid. Xenobiotics such as drugs and ethanol can also be found in sweat.[25] Abnormal health conditions (e.g. electrolyte imbalance and physical stress) and diseases can alter sweat composition by either varying the

concentration of common components or leading to the presence of new components. Despite many advantages, sweat analysis remains an underrepresented solution for health monitoring and clinical diagnosis compared to blood and urine analysis due to the challenges of contamination, evaporation as well as the lack of real time sweat sampling and sensing devices.

While sweat analysis has attracted tremendous attention in recent years, novel wearable and flexible sweat sensing platforms based on different detection approaches have been developed for in situ sweat analysis toward continuous health monitoring. Specifically, sweat analytes are detected and quantified either with electrochemical and/or with optical methods on various flexible substrates.[26–30] The electrochemical sweat sensors use functionalized electrodes to transduce sweat analyte concentration into electrical signals (i.e. current or voltage) which are transmitted to the processing component and give quantitative results with high sensitivity.

1.3 Sweat Stimulation

Sweat is produced from glands located deep within the skin, the body's largest organ by surface area. The skin has a stratified structure including the stratum corneum, epidermis, dermis, and hypodermis. The dermis is the major component of the skin containing blood vessels, nerve endings, and the base of sweat glands, sebaceous glands, and hair follicles (**Fig. 1-2**). The average eccrine sweat gland density is 200/cm^2, but this varies between individuals and across the body with the highest density among the palms and soles (~400/cm^2).[23,31] The total number of eccrine sweat glands is on the order of 1.6–5 million.[23] Eccrine sweat glands secrete a highly filtered, aqueous fluid composed of electrolytes, metabolites, and additional molecules. The works in the thesis focus on eccrine sweat as eccrine sweat glands are the most abundant and active source of sweat.

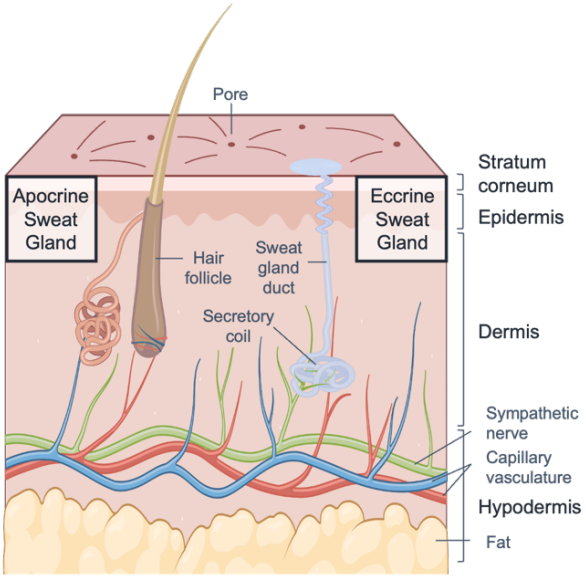

Figure 1-2. Structure of the skin with sweat glands.

Sweat secretion is stimulated by adrenergic and cholinergic innervation (**Fig. 1-3**).[32] When the secretory cell is stimulated, a signaling cascade occurs involving Ca^{2+} or cAMP as second messengers to trigger the efflux of Cl^- into the lumen of the secretory coil. Na^+ is pumped out at the basolateral membrane and diffuses down its electrochemical gradient into the lumen. The buildup of electrolytes in the lumen renders it hypertonic with respect to the cytosol; this osmotic gradient drives the primary sweat solution out of the cell and into the secretory lumen. Advective mass transport drives fluid up the eccrine sweat duct. Along the sweat duct, luminal cells reabsorb ions to produce a hypotonic sweat solution.

Thermoregulatory sweating is an autonomic response to signals from thermoreceptors in the preoptic-anterior hypothalamus area. Upon an increase in core temperature, thermoreceptors send through efferent pathways to postganglionic sympathetic neurons in the dermis.[31] Cholinergic nerve fibers around the secretory coil release acetylcholine, thus activating muscarinic receptors on the membrane of the eccrine secretory cell. Activation of muscarinic G-protein-coupled receptors (GPCRs) increases intracellular inositol trisphosphate (IP_3). IP_3 binds to receptors on the endoplasmic reticulum (ER) membrane to release Ca^{2+}

into the cytosol.[33] Stromal interaction molecule protein, STIM1, monitors the ER Ca^{2+} levels, and when Ca^{2+} stores are depleted STIM1 induces store-operated Ca^{2+} entry by binding to and activating Orai, a Ca^{2+} channel on the plasma membrane.[33] This influx of Ca^{2+} mediates the exchange of electrolytes resulting in sweat secretion.

Sweating is also adrenergically stimulated under the "fight or flight" response. The physical reaction to stress, anxiety, fear, and pain occurs mostly in the palms, soles, and axillary region and may have the selective advantage of increasing palmoplantar friction for fleeing.[23] "Emotional" sweating is controlled by the limbic system and efferent signals are sent to adrenergic nerve fibers in the sweat secretory coil. Release of epinephrine and norepinephrine in signaling stimulates α- and β-adrenoreceptors in sweat secretory cells. A synthetic sympathomimetic drug, isoproterenol, selectively stimulates β-adrenoreceptors and has been used to further differentiate the two pathways. β-adrenergic stimulation is the dominant pathway in emotional sweating. The magnitude of stimulated sweat secretion (measured by secretory rate) is 4:2:1 for cholinergic, β-adrenergic, and α-adrenergic pathways, respectively.[34] α-adrenergic stimulation results in Ca^{2+} influx similar to cholinergic pathways. β-adrenergic GPCRs activate adenylyl cyclase and increase the intracellular concentration of cyclic adenosine monophosphate (cAMP). cAMP activates protein kinase A (PKA), which in turn mediates Cl^- secretion by opening the cystic fibrosis transmembrane conductance regulator (CFTR).[35,36] In the case of cystic fibrosis, CFTR is defective or absent, resulting in blocked CFTR Cl^- secretion during β-adrenergic stimulation and inhibited Cl^- reabsorption. A "ratiometric" sweat rate test comparing adrenergic and cholinergic sweat rates may be used to assess CFTR functional activity.[37]

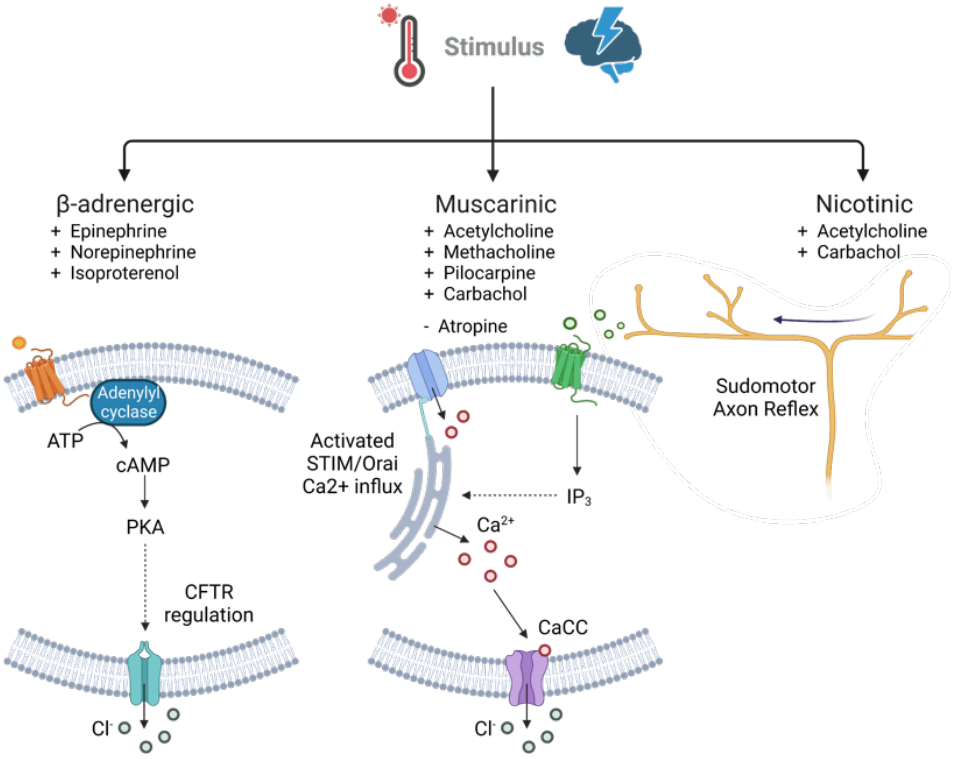

Figure 1-3. Stimulation of sweat.

Sweat may be generated at the periphery of a stimulated region via the sudomotor axon reflex (**Fig. 1-3**). Nicotinic agonists interact with receptors on postganglionic sudomotor terminals at the base of the sweat gland, causing antidromic axonal conduction towards a branch point followed by orthograde conduction down the branching fibers. Acetylcholine is then released at the nerve terminals and binds to muscarinic receptors on the eccrine sweat gland, resulting in sweat secretion similar to the direct iontophoretic response.[31,38] The spatial extension of this sweating could be millimeters beyond the periphery of the stimulation region.[39] The sudomotor axon reflex may be used to assess autonomic nervous system disorders, such as diabetic neuropathy.[31,40] The sudomotor axon reflex may also be used to separate drug-induced sweat stimulation and sweat sampling regions to prevent cross-contamination.[38] The sudomotor axon response has a longer latency than the direct cholinergic response by about 5 s, which accounts for axonal conduction and neuroglandular transmission. The sudomotor axon response and direct response

produce similar sweat volumes in the presence of nicotinic agonists. In contrast to the direct stimulated sweat response, which continues over an hour after cessation of the stimulus, the sudomotor axon response returns to baseline 3–5 minutes after stimulus cessation.[41]

Bibliography of Chapter 1

1. Hamburg, M. A. & Collins, F. S. The path to personalized medicine. *The New England Journal of Medicine* **363**, 301–304 (2010).
2. Larry Jameson, J. & Longo, D. L. Precision medicine—personalized, problematic, and promising. *Obstetrical & Gynecological Survey* **70**, 612 (2015).
3. Gubbi, J., Buyya, R., Marusic, S. & Palaniswami, M. Internet of things (iot): a vision, architectural elements, and future directions. *Future Generation Computer Systems* **29**, 1645–1660 (2013).
4. Hassanalieragh, M. *et al.* Health monitoring and management using internet-of-things (iot) sensing with cloud-based processing: opportunities and challenges. in *2015 IEEE International Conference on Services Computing* 285–292 (2015). doi:10.1109/SCC.2015.47.
5. Patel, S., Park, H., Bonato, P., Chan, L. & Rodgers, M. A review of wearable sensors and systems with application in rehabilitation. *Journal of NeuroEngineering and Rehabilitation* **9**, 21 (2012).
6. Mukhopadhyay, S. C. Wearable sensors for human activity monitoring: a review. *IEEE Sensors Journal* **15**, 1321–1330 (2015).

7. Kim, D.-H., Ghaffari, R., Lu, N. & Rogers, J. A. Flexible and stretchable electronics for biointegrated devices. *Annual Review of Biomedical Engineering* **14**, 113–128 (2012).

8. Sun, J.-Y. *et al.* Highly stretchable and tough hydrogels. *Nature* **489**, 133–136 (2012).

9. Kaltenbrunner, M. *et al.* An ultra-lightweight design for imperceptible plastic electronics. *Nature* **499**, 458–463 (2013).

10. Choi, S., Lee, H., Ghaffari, R., Hyeon, T. & Kim, D.-H. Recent advances in flexible and stretchable bio-electronic devices integrated with nanomaterials. *Advanced Materials* **28**, 4203–4218 (2016).

11. Liu, Y. *et al.* Epidermal mechano-acoustic sensing electronics for cardiovascular diagnostics and human-machine interfaces. *Science Advances* **2**, e1601185 (2016).

12. Chortos, A., Liu, J. & Bao, Z. Pursuing prosthetic electronic skin. *Nature Materials* **15**, 937–950 (2016).

13. Khan, Y., Ostfeld, A. E., Lochner, C. M., Pierre, A. & Arias, A. C. Monitoring of vital signs with flexible and wearable medical devices. *Advanced Materials* **28**, 4373–4395 (2016).

14. Sun, J.-Y., Keplinger, C., Whitesides, G. M. & Suo, Z. Ionic skin. *Advanced Materials* **26**, 7608–7614 (2014).

15. Trung, T. Q. & Lee, N.-E. Flexible and stretchable physical sensor integrated platforms for wearable human-activity monitoring and personal healthcare. *Advanced Materials* **28**, 4338–4372 (2016).

16. Strimbu, K. & Tavel, J. A. What are biomarkers? *Current Opinion in HIV and AIDS* **5**, 463–466 (2010).

17. Hulanicki, A., Glab, S. & Ingman, F. Chemical sensors: definitions and classification. *Pure and Applied Chemistry* **63**, 1247–1250 (1991).

18. Bandodkar, A. J. & Wang, J. Non-invasive wearable electrochemical sensors: a review. *Trends in Biotechnology* **32**, 363–371 (2014).

19. Matzeu, G., Florea, L. & Diamond, D. Advances in wearable chemical sensor design for monitoring biological fluids. *Sensors and Actuators B: Chemical* **211**, 403–418 (2015).

20. Potentiometry. in *Analytical Electrochemistry* 165–200 (John Wiley & Sons, Ltd, 2006). doi:10.1002/0471790303.ch5.

21. Bakker, E., Bühlmann, P. & Pretsch, E. Carrier-based ion-selective electrodes and bulk optodes. 1. General characteristics. *Chemical Reviews* **97**, 3083–3132 (1997).

22. Controlled-potential techniques. in *Analytical Electrochemistry* 67–114 (John Wiley & Sons, Ltd, 2006). doi:10.1002/0471790303.ch3.

23. Wilke, K., Martin, A., Terstegen, L. & Biel, S. S. A short history of sweat gland biology. *International Journal of Cosmetic Science* **29**, 169–179 (2007).

24. Mitsubayashi, K., Suzuki, M., Tamiya, E. & Karube, I. Analysis of metabolites in sweat as a measure of physical condition. *Analytica Chimica Acta* **289**, 27–34 (1994).

25. Sato, K., Kang, W. H., Saga, K. & Sato, K. T. Biology of sweat glands and their disorders. I. Normal sweat gland function. *Journal of the American Academy of Dermatology* **20**, 537–563 (1989).

26. Coyle, S. *et al.* Textile sensors to measure sweat ph and sweat-rate during exercise. in *2009 3rd International Conference on Pervasive Computing Technologies for Healthcare* 1–6 (2009). doi:10.4108/ICST.PERVASIVEHEALTH2009.5957.

27. Choi, J. *et al.* Soft, skin-integrated multifunctional microfluidic systems for accurate colorimetric analysis of sweat biomarkers and temperature. *ACS Sensors* **4**, 379–388 (2019).

28. Kim, J. *et al.* Noninvasive alcohol monitoring using a wearable tattoo-based iontophoretic-biosensing system. *ACS Sensors* **1**, 1011–1019 (2016).

29. Gao, W. *et al.* Fully integrated wearable sensor arrays for multiplexed in situ perspiration analysis. *Nature* **529**, 509–514 (2016).

30. Sempionatto, J. R., Moon, J.-M. & Wang, J. Touch-based fingertip blood-free reliable glucose monitoring: personalized data processing for predicting blood glucose concentrations. *ACS Sensors* **6**, 1875–1883 (2021).

31. Low, P. A. Evaluation of sudomotor function. *Clinical Neurophysiology* **115**, 1506–1513 (2004).

32. Cui, C.-Y. & Schlessinger, D. Eccrine sweat gland development and sweat secretion. *Experimental Dermatology* **24**, 644–650 (2015).

33. Bovell, D. L. The evolution of eccrine sweat gland research towards developing a model for human sweat gland function. *Experimental Dermatology* **27**, 544–550 (2018).

34. Sato, K. & Sato, F. Role of calcium in cholinergic and adrenergic mechanisms of eccrine sweat secretion. *American Journal of Physiology-Cell Physiology* **241**, C113–C120 (1981).

35. Quinton, P. M. Cystic fibrosis: lessons from the sweat gland. *Physiology* **22**, 212–225 (2007).

36. Mihályi, C., Iordanov, I., Töröcsik, B. & Csanády, L. Simple binding of protein kinase A prior to phosphorylation allows CFTR anion channels to be opened by nucleotides. *Proceedings of the National Academy of Sciences* **117**, 21740–21746 (2020).

37. Salinas, D. B. *et al.* Image-based β-adrenergic sweat rate assay captures minimal cystic fibrosis transmembrane conductance regulator function. *Pediatric Research* **87**, 137–145 (2020).

38. Sonner, Z., Wilder, E., Gaillard, T., Kasting, G. & Heikenfeld, J. Integrated sudomotor axon reflex sweat stimulation for continuous sweat analyte analysis with individuals at rest. *Lab on a Chip* **17**, 2550–2560 (2017).

39. Riedl, B., Nischik, M., Birklein, F., Neundörfer, B. & Handwerker, H. O. Spatial extension of sudomotor axon reflex sweating in human skin. *Journal of the Autonomic Nervous System* **69**, 83–88 (1998).

40. Kihara, M., Opfer-Gehrking, T. L. & Low, P. A. Comparison of directly stimulated with axon-reflex–mediated sudomotor responses in human subjects and in patients with diabetes. *Muscle & Nerve* **16**, 655–660 (1993).

41. Low, P. A., Opfer-Gehrking, T. L. & Kihara, M. In vivo studies on receptor pharmacology of the human eccrine sweat gland. *Clinical Autonomic Research* **2**, 29–34 (1992).

Chapter 2

LASER-ENGRAVED GRAPHENE SENSORS

Materials from this chapter appears in "Wang, M.; Yang, Y.; Gao, W. Laser-engraved graphene for flexible and wearable electronics. *Trends in Chemistry* 3, 969–981 (2021) doi:10.1016/j.trechm.2021.09.001" and "Yang, Y.; Song, Y.; Bo, X.; Min, J.; Pak, O. S.; Zhu, L.; Wang, M.; Tu, J.; Kogan, A.; Zhang, H.; Hsiai, T. K.; Li, Z.; Gao, W. A laser-engraved wearable sensor for sensitive detection of uric acid and tyrosine in sweat. *Nature Biotechnology* 38, 217–224 (2020) doi:10.1038/s41587-019-0321-x."

2.1 Introduction

Graphene has been broadly used in the development of flexible electronic devices and systems, thanks to its high theoretical specific surface area, mobility, flexibility, mechanical strength, conductivity, and biocompatibility.[1–4] The fabrication of graphene is commonly achieved by chemical vapor deposition, mechanical exfoliation, and wet chemical reduction of graphene oxide (GO).[5–7] Although conventional processing techniques, such as screen-printing, roll-to-roll printing, and inkjet printing, have been used to fabricate graphene-based devices,[8–10] in most cases, restacking of graphene sheets in the presence of additives hinders their performance.[11,12] An important frontier lies in the large-scale, low-cost production of high-performance and versatile graphene-based electronics for wide-range applications of graphene in consumer devices, and LEG has shown great potential to this end.

Laser processing technologies permit scalable patterning of graphene on various substrates, primarily either via laser-induced direct carbonization of polymeric substrates [e.g., polyimide (PI), polyethyleneimine] or laser-induced reduction of GO. In the 2010s, it was found that commercially available CO_2 laser cutters could be used to directly engrave and pattern porous graphene on various synthetic and natural carbon precursor (e.g., PI) substrates under ambient conditions,[13] without generating hazardous wastes.[14] Since then, LEG has shown tremendous potential for flexible electronics applications, as it has unique electrical and chemical properties and allows rapid customizable prototyping on a large scale and at low cost.[15–17]

Direct graphene patterning can be achieved with lasers of various wavelengths, spanning from UV to infrared (IR).[18] When the laser beam reaches the precursor of graphene (i.e., PI), graphene forms in a photochemical and/or photothermal process. The photochemical reaction usually appears when a short-wavelength (i.e., UV or blue) laser source is used, as its high photon energy absorbed can directly break chemical bonds and form a dense graphene structure.[18,19] The photothermal reaction could become predominant when a longer-wavelength (i.e., IR) laser source is used,

as the absorbed laser energy is converted into local heat and thus leads to a high localized temperature (>2500°C).[13] It should be noticed that multiple laser parameters (e.g., wavelength,[20–22] power,[23] pulse width,[24] and scanning speed) play a key role in the final graphene structure formation and should be considered concurrently during graphene fabrication. When engraving the PI with a 10.6-μm CO_2 laser cutter, chemical bonds in the PI network are broken and thermal reorganization of the carbon atoms occurs, resulting in sheets of graphene structures.[18] It has been shown that such LEG flakes are full of defects, expanding a hexagon lattice with two pentagons and one heptagon, which could lead to a porous structure.[25] With custom laser settings, different morphologies of the graphene structure can be directly patterned on PI, ranging from isotropic pores, cellular networks, and nanofibers.[23]

Current wearable sweat sensors are primarily focused on a limited number of electrolytes and metabolites monitored via ion-selective sensors or enzymatic electrodes.[26–28] Among the analytes for which wearable sensors do not exist are uric acid (UA) and tyrosine (Tyr). UA is a risk factor for cardiovascular disease,[29,30] type 2 diabetes[31,32] and renal disease,[33] and has been widely used in clinical settings for the management of gout,[34,35] the most common inflammatory arthritis affecting tens of millions of people worldwide.[36] Tyr is a conditionally essential amino acid involved in brain signaling and in the production of dopamine and stress hormones (for example, noradrenaline and adrenaline).[37] Abnormal Tyr concentrations are linked to metabolic disorders such as tyrosinemia,[38,39] liver diseases,[39] neuropsychiatric, and eating disorders.[40,41] Measurement of UA and Tyr in sweat is challenging because of their low concentrations in micromolar ranges that are difficult to detect with existing methods.

To tackle the low-concentration sensing challenge, LEG is a promising new candidate in electrochemical biosensors due to its attractive electrochemical properties such as large surface area, excellent stability, and abundant catalytic active sites, which significantly improve the electron transfer kinetics and thereby enable

the sensitive detection of biomarkers in biofluids. Moreover, considering that scalable manufacture is crucial for widespread implementation of wearable sensors, a promising fabrication technology is CO_2 laser engraving, which may allow rapid engraving of patterns in ambient conditions and reduce personnel training and process optimization. The use of CO_2 laser-engraving technology has not been used to fabricate a multimodal wearable system. The sweat sensor presented in this thesis is entirely laser engraved to facilitate scalable manufacture and flexibility for the wearer's comfort.

2.2 Materials and Methodology

Materials and reagents

Uric acid, l-tyrosine, silver nitrate, iron chloride (III), dopamine hydrochloride, choline chloride, creatinine, pantothenic acid calcium salt, citrulline, pyridoxine and lactic acid were purchased from Alfa Aesar. Sodium thiosulfate pentahydrate, sodium bisulfite, tryptophan, leucine, alanine, isoleucine, methionine, valine, lysine, thiamine hydrochloride and serine were purchased from Sigma Aldrich. Potassium ferricyanide (III) was purchased from Acros Organics. Acetic acid, sodium acetate, sodium chloride, urea, l-ascorbic acid and dextrose (d-glucose) anhydrous, glycine, arginine, inositol, ornithine, aspartic acid, threonine, histidine, riboflavin, creatine, phenylalanine, nicotinic acid, folic acid and glutamic acid were purchased from Thermo Fisher Scientific. Polyimide film (75 μm thick) and PET (12 μm and 75 μm thick) were purchased from DuPont and McMASTER-CARR, respectively. Glassy carbon electrodes were purchased from CH Instruments, screen-printed carbon electrodes were purchased from Metrohm AG and gold electrodes were fabricated on a PET substrate by photolithography followed by 30 nm Cr/100 nm gold deposition via electron-beam evaporation and lift-off in acetone.

Fabrication and characterization of the LEG

For sensor patterning, a polyimide film (DuPont) was attached onto a supporting substrate in a 50-W CO_2 laser cutter (Universal Laser System). The optimized

parameters for the chemical sensor were power 6.3%, speed 5.5%, points per inch (PPI) 1,000 and raster mode. After graphene electrodes were scribed, silver was electrodeposited onto one pattern to function as the reference electrode at −0.2 mA for 100 s using a plating solution containing 250 mM silver nitrate, 750 mM sodium thiosulfate and 500 mM sodium bisulfite. The physical sensors had their contact pads scribed with the same parameters as the chemical sensors. For the active sensing area of the strain sensor, the optimized parameters were power 0.3%, speed 1.0% (1.4%, 1.2% and 1.0% were described as higher speed, medium speed and lower speed, respectively, in **Fig.2-6i** and **Appendix A, Fig. A-11**), PPI 400, vector mode; for the active sensing area of the temperature sensor, the optimized parameters were power 1.5%, speed 11%, PPI 1,000 and vector mode. Scanning electron microscopy (SEM) images were taken with a field emission scanning electron microscope (FEI Sirion). The surface properties of the laser-induced graphene were characterized by X-ray photoelectron spectroscopy (Escalab 250xi, Thermo Fisher Scientific). The Raman spectrum of graphene was recorded using a 532.8-nm laser with an inVia Reflex (Renishaw).

Characterization of the UA and Tyr sensors

All sensor characterizations were performed in 0.01 M acetate buffer saline (ABS) (pH 4.6 with the addition of 50 mM NaCl) unless otherwise noted. DPV analysis was performed through an electrochemical workstation (CHI 832D). The detailed parameters were: range, 0–0.9 V; incremental potential, 0.004 V; pulse amplitude, 0.05 V; pulse width, 0.05 s; pulse period, 0.5 s; and sensitivity, 1×10^{-5} A/V. The selectivity study of the LEG was tested in ABS containing physiological concentrations of analytes. The dependence of the sensor response on pH was studied by DPV tests in 0.3× PBS with solution pHs adjusted by lactic acid.

Characterization of the strain and temperature sensors

The temperature sensor characterization was performed on a ceramic hot plate (Thermo Fisher Scientific) (**Fig.2-6f,g** and **Appendix A, Fig.A-10**). The sensor response was recorded using a parameter analyzer (Keithley 4200A-SCS) and

compared with the readings from an infrared thermometer (LASERGRIP 800; Etekcity). The response of the strain sensor was recorded using the parameter analyzer (Keithley 4200A-SCS) in a controlled temperature atmosphere (23 ± 1 °C). The accuracy of the strain sensor for heart rate and respiration rate monitoring was validated on a healthy subject with a commercially available vital-sign monitor (Masimo MightySat; **Appendix A, Fig. A-11**). Under repetitive bending under a 0.1% strain for 10,000 cycles (performed using a Lynxmotion AL5D 4DOF Robotic Arm), the mechanical deformation effect on LEG-based electrode was evaluated (**Fig. 2-8**).

2.3 Results and Discussion

With the use of the CO_2 laser engraving technique, we have developed a laser-engraved sensor patch for multiplex sensing of uric acid, tyrosine and vital signs.

Characterization of the LEG-based UA and Tyr sensor

Owing to its unique electrochemical properties arising from the fast electron mobility, high current density and ultra large surface area, graphene is an appropriate candidate for building high-performance sensors to detect ultralow levels of electroactive analytes in body fluids. Laser cutting has been used to directly obtain graphene structures from a variety of substrates toward energy storage and fluid capture applications.[13,15,42] Here we manufactured highly sensitive LEG-CS on polyimide via raster mode (**Fig.2-1a-d** and **Appendix A, Fig. A-1).** The three-electrode LEG-CS could selectively catalyze the oxidation of UA and Tyr at specific potentials (**Fig.2-1b**). After optimization on the basis of the DPV peak amplitudes of UA and Tyr in the standard solutions (**Fig. 2-2 and Table 2-1**) and electrochemical impedance spectroscopy (**Appendix A, Fig. A-2**), the electrocatalytic activity and reproducibility of LEG-CS for direct oxidation of UA and Tyr at physiological concentrations had sensitivities of 3.50 $\mu A\ \mu M^{-1}\ cm^{-2}$ and 0.61 $\mu A\ \mu M^{-1}\ cm^{-2}$, and low detection limits of 0.74 μM and 3.6 μM, respectively (**Fig. 2-1e,f** and **Appendix A, Fig. A-3**). Two distinct current peaks at ~0.39 V and

~0.64 V from the DPV scans correspond to the oxidation reactions of UA and Tyr, respectively.

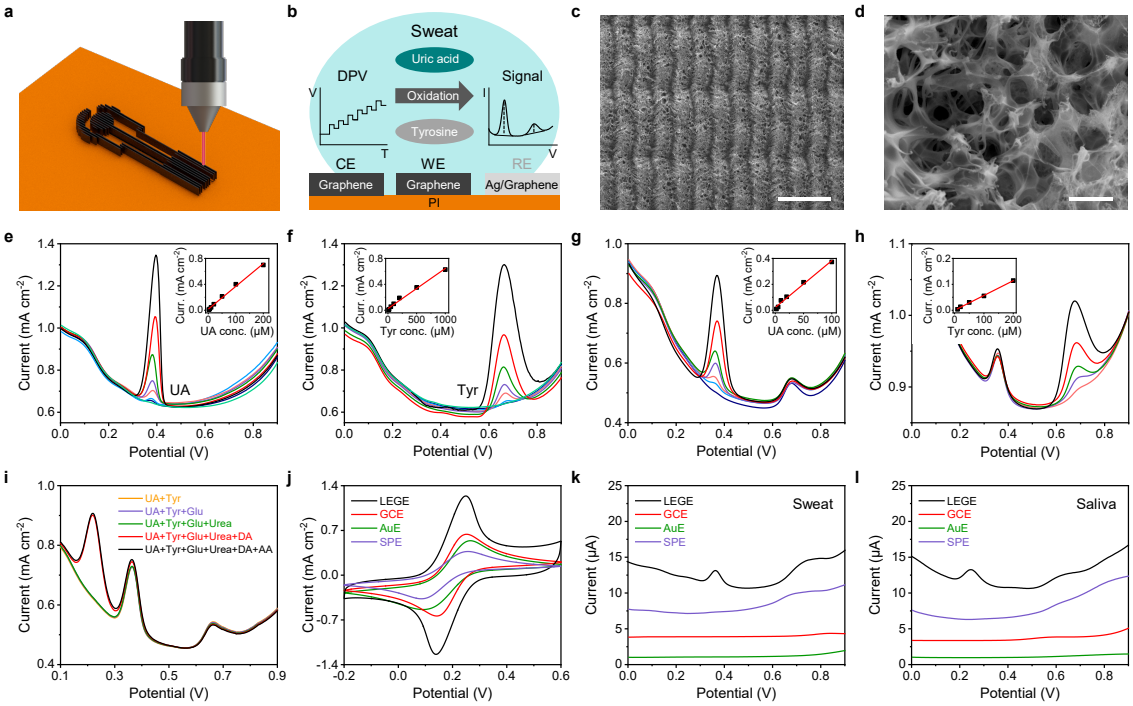

Figure. 2-1: Schematics and characterization of the LEG-based UA and Tyr sensor. a, Schematic of the raster mode for LEG-CS fabrication. **b,** A three-electrode LEG-based flexible sensor for simultaneous UA and Tyr detection. CE, counter electrode; WE, working electrode; RE, reference electrode. c,d, SEM images of the LEG-CS. Scale bars, 200 µm (c) and 3 µm (d). e,f, UA (e) and Tyr (f) detection with the LEG-CS in a 0.01 M ABS solution. Insets are the corresponding calibration plots. Curr., current. g,h, Simultaneous and selective detection of UA in the presence of 50 µM Tyr (g) and Tyr in the presence of 50 µM UA (h). i, Simultaneous detection of 50 µM UA and 50 µM Tyr in the presence of common interferences: 170 µM glucose (Glu), 10 mM urea, 25 µM dopamine (DA) and 50 µM ascorbic acid (AA). j, Cyclic voltammetry scans of an LEG electrode (LEGE), a glassy carbon electrode (GCE), a gold electrode (AuE), and a screen-printed carbon electrode (SPE) in a solution containing 5 mM $[Fe(CN)_6]^{3-}$ and

0.2 M KCl. k,l, DPV signals in raw sweat (k) and saliva (l) samples from an LEG electrode, a glassy carbon electrode, a gold electrode and a screen-printed carbon electrode. Experiments in e–l were repeated five times independently with similar results.

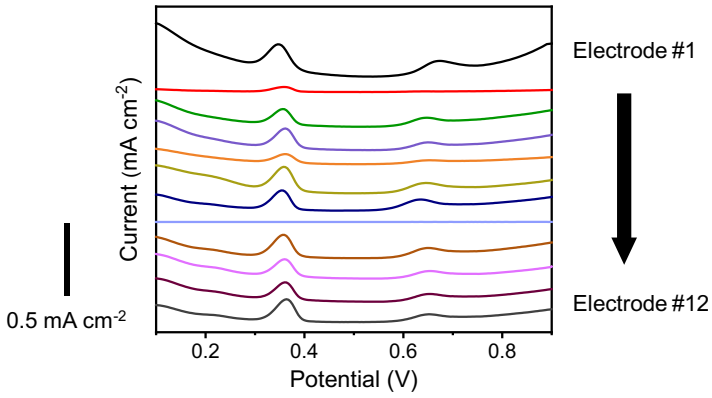

Figure 2-2. Optimization of the LEG-based chemical sensor under different laser parameters. Condition, 50 μM UA and 50 μM Tyr. Five experiments were performed independently with similar results.

Electrode #	Power (%)	Speed (%)	PPI	UA Peak (mA cm^{-2})	Tyr Peak (mA cm^{-2})
1	6.3	5.5	1000	0.142	0.061
2	6	5	1000	0.003	0
3	6	6	1000	0.091	0.035
4	6	7	1000	0.113	0.029
5	6	8	1000	0.05	0.013
6	5.5	5	1000	0	0
7	6.5	5	1000	0.132	0.043
8	7.5	5	1000	0.101	0.032
9	6	5	250	0.138	0.045
10	6	5	500	0.115	0.049
11	6	5	750	0.1	0.033
12	6	5	1000	0.131	0.031

Table 2-1. Optimization of the LEG-CS with different laser parameters.

The LEG-based UA and Tyr sensor shows excellent selectivity over other analytes in sweat at physiologically relevant concentrations[43] (**Fig.2-1g-i**, **Fig. 2-3,2-4**, **Appendix A, Fig. A-4-6, Note A-1**, **Table A-1**).

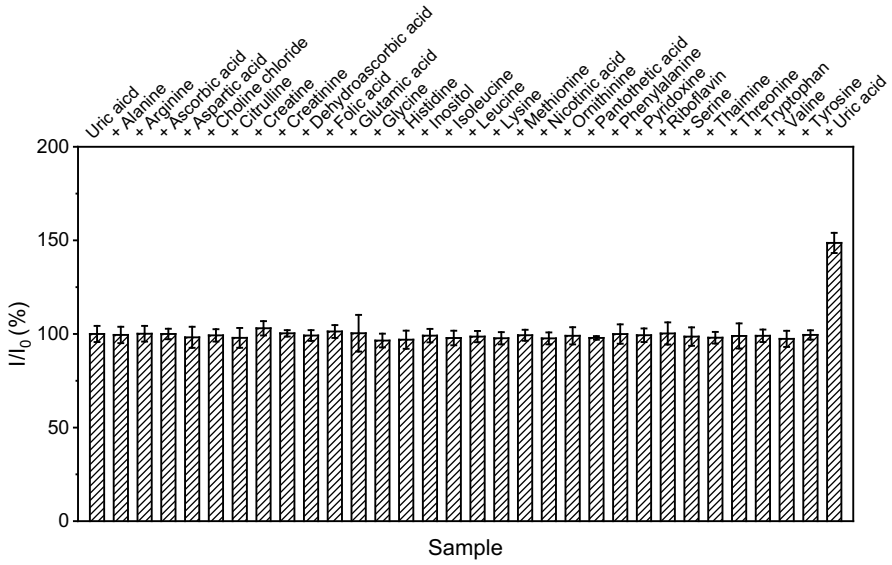

Figure 2-3. The selectivity of the LEG-CS to UA over other analytes in human sweat. I and I_0 represent the peak amplitude of the DPV plot of an LEG-CS, and the average peak amplitude obtained from the initial UA solution, respectively. The concentrations of the initial UA and other analytes are based on **Appendix A, Table A-1**. UA concentration was increased by 50% in the end. Error bars represent the standard deviations of four measurements.

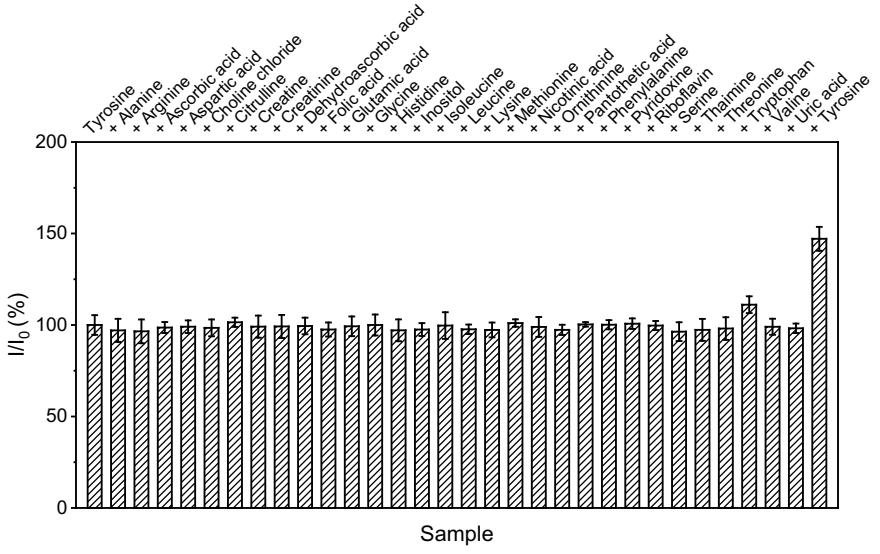

Figure 2-4. The selectivity of the LEG-CS to Tyr over other analytes in human sweat. I and I_0 represent the peak amplitude of the DPV plot of an LEG-CS, and the

average peak amplitude obtained from the initial Tyr solution, respectively. The concentrations of the initial Tyr and other analytes are based on **Appendix A, Table A-1**. Tyr concentration was increased by 50% in the end. Error bars represent the standard deviations of four measurements.

The LEG-CS displays superior electrochemical performance over commercial glassy carbon, screen-printed carbon and gold electrodes (**Fig. 2-1j**). Moreover, it enables direct detection of UA and Tyr in raw body fluids (that is, sweat and saliva) (**Fig. 2-1k,l**). The response of UA and Tyr sensing can be wirelessly recorded using the as-designed FPCB (**Appendix A, Fig. A-7,8**). Although we focus on the detection of UA and Tyr in this work, LEG-CS is able to detect ultralow levels of other electroactive molecules such as ascorbic acid and dopamine (**Appendix A, Fig. A-9**). The LEG-CS is mechanically flexible, fully compliant with the skin and exhibits mechanical and electrochemical stability (**Fig. 2-5**).

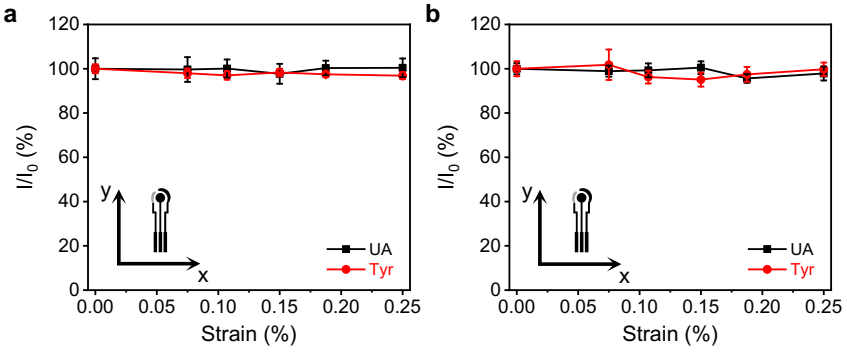

Figure 2-5. Stability of the LEG-CS during the bending tests. a,**b**, The long term stability of an LEG-based sensor during the bending test. 0–0.25 % strains were applied for both x (**a**) and y (**b**) axis. I and I_0 represent the current amplitude of the DPV plot during the bending, and the average current amplitude without bending, respectively. The error bars represent the standard deviation of 10 measurements. Conditions, 50 μM UA and 100 μM Tyr.

Design and characterization of the LEG-based vital-sign monitor

The LEG has unique properties for designing resistive physical sensors: as the temperature rises, its conductivity increases owing to increased electron–phonon scattering and thermal velocity of electrons in the sandwiched layers [44] (**Fig. 2-6a**);

when an external strain is applied, its three-dimensional porous structure is compressed, resulting in decreased resistance (**Fig. 2-6b**). Here the LEG-based temperature and piezoresistive strain sensors are fabricated in vector mode (**Fig. 2-6c,d** and **Appendix A, Fig. A-1**). Both material morphology and sensor layout are important in achieving the desired sensor performance: the fiber-like structure resulted from a high dose of local laser power (**Fig. 2-6d** and **Fig.2-7**) coupled with a straight-line design (strain sensor) yields the highest strain response; the compact structure (**Fig. 2-6c**) coupled with serpentine line design (temperature sensor) is less susceptible to strain variations (**Fig. 2-6e**).

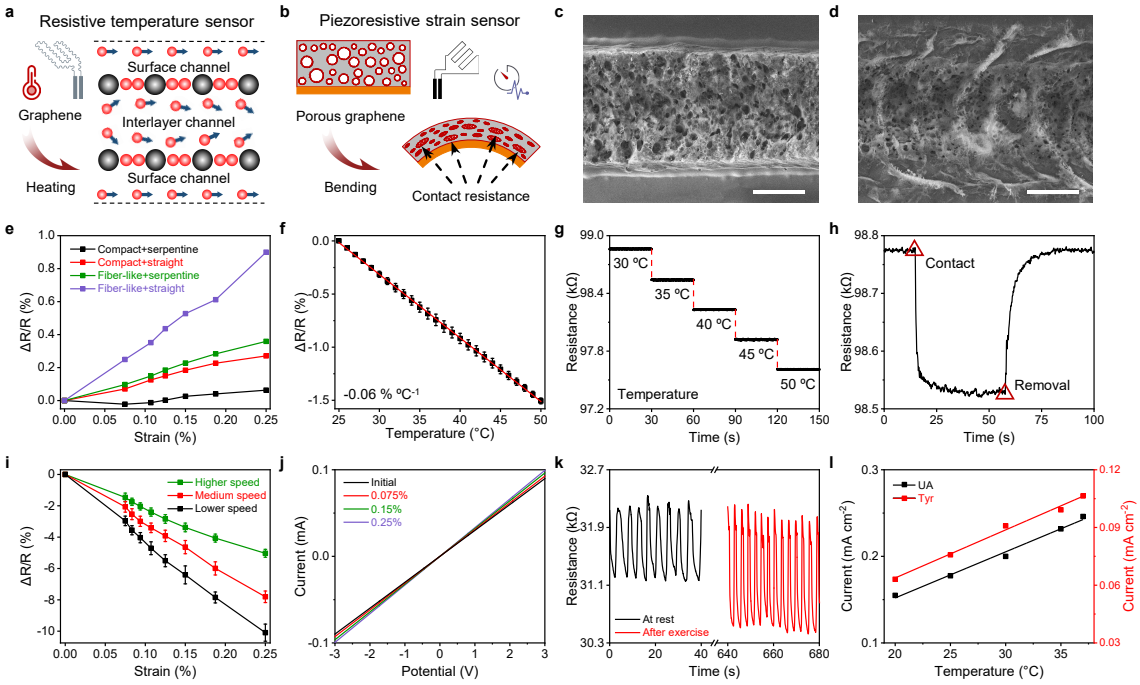

Figure. 2-6: Design and characterization of the LEG-based vital-sign sensors. **a**,**b**, Mechanisms of temperature sensing (**a**) and strain sensing (**b**) using LEG. **c**,**d**, SEM images of an LEG-based temperature sensor (**c**) and an LEG-based strain sensor (**d**). Scale bars, 100 μm. **e**, Strain responses of LEG with different morphologies and layouts. **f**,**g**, Calibration plot (**f**) and dynamic response (**g**) of the LEG-based temperature sensor in the physiological temperature range. Error bars represent the s.d. from ten sensors of different batches (ten measurements per sensor). **h**, Dynamic

response of an LEG-based temperature sensor upon contact with and removal from the human body. **i**, Strain responses of the LEG-based strain sensors prepared with varied laser scanning speeds. Error bars represent the s.d. from ten sensors of different batches (ten measurements per sensor). **j**, *I*–*V* curves of a strain sensor under different strains. **k**, Real-time respiration rate measurement with a strain sensor, at rest and after exercise. **l**, Dependence of the response of LEG-CS on the temperature. Condition, 50 μM UA and 100 μM Tyr in ABS. $\Delta R/R$ represents the ratio of the resistance change to the flat state resistance of the vital-sign sensor at 25 °C. Experiments in **e** and **g** were repeated ten times independently with similar results. Experiments in **h** and **j**–**l** were repeated five times independently with similar results.

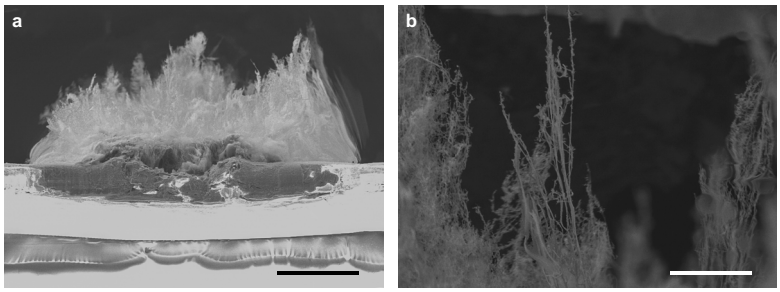

Figure 2-7. Porous fiber-like graphene structure for strain sensing. a, Cross-section SEM image of the fiber-like LEG. Scale bar, 100 μm. **b**, Magnified view of the fiber-like LEG structure. Scale bar, 10 μm.

The temperature sensor shows a fast, accurate and stable response to temperature variations with a sensitivity of −0.06% $°C^{-1}$ and a low detection limit of 0.051 °C (**Fig. 2-6f-h** and **Appendix A, Fig.A-10**), which indicates the negative temperature coefficient behavior of the LEG. The strain sensor is fabricated at a low laser speed for large strain response and high stability (**Fig. 2-6i,j** and **Appendix A, Fig. A-11),** which is ideally suited for accurate monitoring of respiration rate (**Fig. 2-6k**) and heart rate (**Appendix A, Fig. A-12**), as validated with commercial vital monitors (**Appendix A, Fig. A-13**). After 10,000 bending cycles, the flat-state resistance of the strain sensor remains stable (**Fig. 2-8**). The temperature and strain sensor response can be accurately monitored by the FPCB (**Appendix A, Fig. A-14**).

Considering that the response of the UA and Tyr sensor can be influenced by temperature variations (**Fig. 2-6l**), the temperature sensor readings could be used for real-time chemical sensor calibration during on-body use.

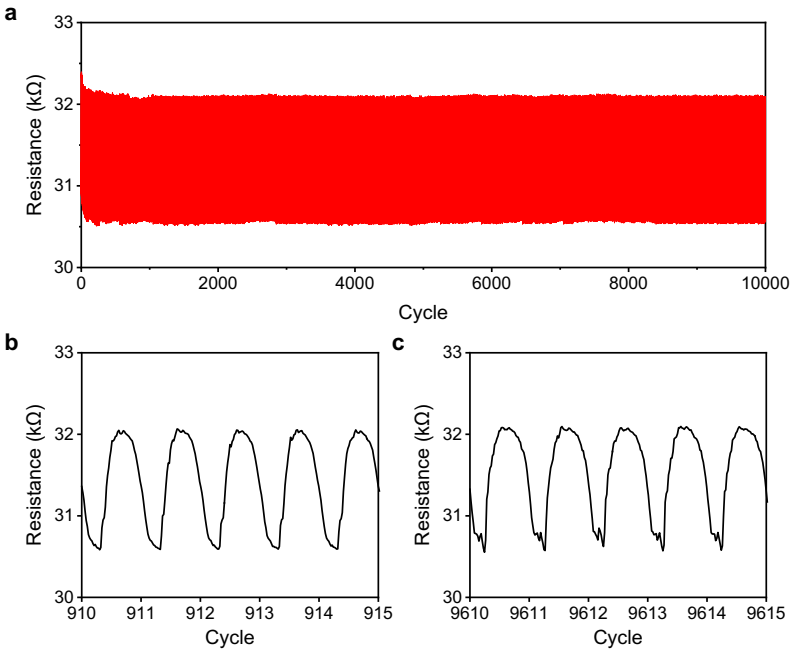

Figure 2-8. The long-term stability of the LEG-based strain sensor. a, The measurement was performed during a bending test of a strain sensor (10,000 cycles with strains alternated between 0% and 0.1%). **b**,**c**, The resistive sensor response during 910–915 cycles (**b**) and 9610–9615 cycles (**c**) of bending.

2.4 Conclusion

Our laser-engraved multimodal sensor enables efficient and sensitive molecular sensing and multiplexed vital-sign sensing. Owing to its fast electron mobility, high current density and ultralarge surface area, the graphene-based chemical sensor achieves rapid and accurate detection of UA and Tyr in human sweat in situ. The vital sign physical sensors also exhibit excellent stability and sensitivity for temperature and strain sensing. Moreover, the fabrication of the sensor with a widely available CO_2 laser engraving approach sets great potential for the mass production and the eventual use of these sensors for biomedical sensing.

Bibliography of Chapter 2

1. Geim, A. K. Graphene: status and prospects. *Science* **324**, 1530–1534 (2009).
2. Han, T.-H., Kim, H., Kwon, S.-J. & Lee, T.-W. Graphene-based flexible electronic devices. *Materials Science and Engineering: R: Reports* **118**, 1–43 (2017).
3. You, R. *et al.* Laser fabrication of graphene-based flexible electronics. *Advanced Materials* **32**, 1901981 (2020).
4. Khan, U., Kim, T.-H., Ryu, H., Seung, W. & Kim, S.-W. Graphene tribotronics for electronic skin and touch screen applications. *Advanced Materials* **29**, 1603544 (2017).
5. Chen, Z. *et al.* Three-dimensional flexible and conductive interconnected graphene networks grown by chemical vapour deposition. *Nature Materials* **10**, 424–428 (2011).
6. Xu, Y., Sheng, K., Li, C. & Shi, G. Self-assembled graphene hydrogel via a one-step hydrothermal process. *ACS Nano* **4**, 4324–4330 (2010).
7. Eigler, S. *et al.* Wet chemical synthesis of graphene. *Advanced Materials* **25**, 3583–3587 (2013).
8. Bae, S. *et al.* Roll-to-roll production of 30-inch graphene films for transparent electrodes. *Nature Nanotechnology* **5**, 574–578 (2010).
9. Hyun, W. J., Secor, E. B., Hersam, M. C., Frisbie, C. D. & Francis, L. F. High-resolution patterning of graphene by screen printing with a silicon stencil for highly flexible printed electronics. *Advanced Materials* **27**, 109–115 (2015).

10. Capasso, A. *et al.* Ink-jet printing of graphene for flexible electronics: An environmentally-friendly approach. *Solid State Communications* **224**, 53–63 (2015).

11. Zhang, Y., Zhang, J., Wu, H., Guo, S. & Zhang, J. Glass carbon electrode modified with horseradish peroxidase immobilized on partially reduced graphene oxide for detecting phenolic compounds. *Journal of Electroanalytical Chemistry* **681**, 49–55 (2012).

12. Wang, F., Wu, Y., Lu, K., Gao, L. & Ye, B. A simple, rapid and green method based on pulsed potentiostatic electrodeposition of reduced graphene oxide on glass carbon electrode for sensitive voltammetric detection of sophoridine. *Electrochimica Acta* **141**, 82–88 (2014).

13. Lin, J. *et al.* Laser-induced porous graphene films from commercial polymers. *Nature Communications* **5**, 5714 (2014).

14. Chyan, Y., Ye, R., Li, Y., Singh, S.P., Arnusch, C.J. and Tour, J.M. Laser-induced graphene by multiple lasing: toward electronics on cloth, paper, and food. *ACS Nano*. https://pubs.acs.org/doi/10.1021/acsnano.7b08539.

15. Ye, R., James, D. K. & Tour, J. M. Laser-induced graphene. *Accounts of Chemical Research.* **51**, 1609–1620 (2018).

16. Ye, R., James, D. K., & Tour, J. M. Laser-induced graphene: from discovery to translation. *Advanced Materials* **31**(1), 1803621(2019).

17. Luong, D. X. *et al.* Laser-induced graphene composites as multifunctional surfaces. *ACS Nano* **13**, 2579–2586 (2019).

18. Direct laser writing of graphene electrodes: *Journal of Applied Physics* **127**, 1. https://aip.scitation.org/doi/10.1063/1.5120056.

19. Tao, L.-Q. *et al.* An intelligent artificial throat with sound-sensing ability based on laser induced graphene. *Nature Communications* **8**, 14579 (2017).

20. Carvalho, A. F. *et al.* Laser-induced graphene strain sensors produced by ultraviolet irradiation of polyimide. *Advanced Functional Materials* **28**, 1805271 (2018).

21. Duy, L. X. *et al.* Laser-induced graphene fibers. *Carbon* **126**, 472–479 (2018).

22. Wang, L., Wang, Z., Bakhtiyari, A. N. & Zheng, H. A comparative study of laser-induced graphene by CO_2 infrared laser and 355 nm ultraviolet (UV) laser. *Micromachines* **11**, 1094 (2020).

23. Abdulhafez, M., Tomaraei, G. N. & Bedewy, M. Fluence-dependent morphological transitions in laser-induced graphene electrodes on polyimide substrates for flexible devices. *ACS Applied Nano Materials* **4**, 2973–2986 (2021).

24. Garland, N. T. *et al.* Flexible laser-induced graphene for nitrogen sensing in soil. *ACS Applied Materials and Interfaces* **10**, 39124–39133 (2018).

25. Ma, J., Alfè, D., Michaelides, A. & Wang, E. Stone-Wales defects in graphene and other planar sp2-bonded materials. *Physical Review B* **80**, 033407 (2009).

26. Bariya, M., Nyein, H. Y. Y. & Javey, A. Wearable sweat sensors. *Nature Electronics* **1**, 160–171 (2018).

27. Choi, J., Ghaffari, R., Baker, L. B. & Rogers, J. A. Skin-interfaced systems for sweat collection and analytics. *Science Advances* **4**, eaar3921 (2018).

28. Jia, W. *et al.* Electrochemical tattoo biosensors for real-time noninvasive lactate monitoring in human perspiration. *Analytical Chemistry* **85**, 6553–6560 (2013).

29. Feig, D. I., Kang, D.-H. & Johnson, R. J. Uric acid and cardiovascular risk. *New England Journal of Medicine* **359**, 1811–1821 (2008).

30. Gagliardi, A. C. M., Miname, M. H. & Santos, R. D. Uric acid: A marker of increased cardiovascular risk. *Atherosclerosis* **202**, 11–17 (2009).

31. Bhole, V., Choi, J. W. J., Woo Kim, S., de Vera, M. & Choi, H. Serum uric acid levels and the risk of type 2 diabetes: a prospective study. *The American Journal of Medicine* **123**, 957–961 (2010).

32. Kodama, S. *et al.* Association between serum uric acid and development of type 2 diabetes. *Diabetes Care* **32**, 1737–1742 (2009).

33. Kohagura, K. *et al.* An association between uric acid levels and renal arteriolopathy in chronic kidney disease: a biopsy-based study. *Hypertension Research* **36**, 43–49 (2013).

34. Terkeltaub, R. Update on gout: new therapeutic strategies and options. *Nature Reviews Rheumatology* **6**, 30–38 (2010).

35. Major, T. J., Dalbeth, N., Stahl, E. A. & Merriman, T. R. An update on the genetics of hyperuricaemia and gout. *Nature Reviews Rheumatology* **14**, 341–353 (2018).

36. Smith, E. *et al.* The global burden of gout: estimates from the Global Burden of Disease 2010 study. *Annals of the Rheumatic Diseases* **73**, 1470–1476 (2014).

37. Fernstrom, J. D. & Fernstrom, M. H. Tyrosine, phenylalanine, and catecholamine synthesis and function in the brain. *The Journal of Nutrition* **137**, 1539S-1547S (2007).

38. Russo, P. A., Mitchell, G. A. & Tanguay, R. M. Tyrosinemia: A Review. *Pediatric and Developmental Pathology* **4**, 212–221 (2001).

39. Levine, R. J. & Conn, H. O. Tyrosine Metabolism in Patients with Liver Disease. *Journal of Clinical Investigation* **46**, 2012–2020 (1967).

40. D'Andrea, G. *et al.* Study of tyrosine metabolism in eating disorders. Possible correlation with migraine. *Neurological Sciences* **29**, 88 (2008).

41. Capuron, L. *et al.* Chronic low-grade inflammation in elderly persons is associated with altered tryptophan and tyrosine metabolism: role in neuropsychiatric symptoms. *Biological Psychiatry* **70**, 175–182 (2011).

42. Li, G., Mo, X., Law, W.-C. & Chan, K. C. Wearable fluid capture devices for electrochemical sensing of sweat. *ACS Applied Materials and Interfaces* **11**, 238–243 (2019).

43. Harvey, C. J., LeBouf, R. F. & Stefaniak, A. B. Formulation and stability of a novel artificial human sweat under conditions of storage and use. *Toxicology in Vitro* **24**, 1790–1796 (2010).

44. Shao, Q., Liu, G., Teweldebrhan, D. & Balandin, A. A. High-temperature quenching of electrical resistance in graphene interconnects. *Applied Physics Letters* **92**, 202108 (2008).

A p p e n d i x A

SUPPLEMENTARY INFORMATION FOR CHAPTER 2

Materials from this chapter appear in “Yang, Y.; Song, Y.; Bo, X.; Min, J.; Pak, O. S.; Zhu, L.; Wang, M.; Tu, J.; Kogan, A.; Zhang, H.; Hsiai, T. K.; Li, Z.; Gao, W. A laser-engraved wearable sensor for sensitive detection of uric acid and tyrosine in sweat. *Nature Biotechnology* 38, 217–224 (2020) doi:10.1038/s41587-019-0321-x”.

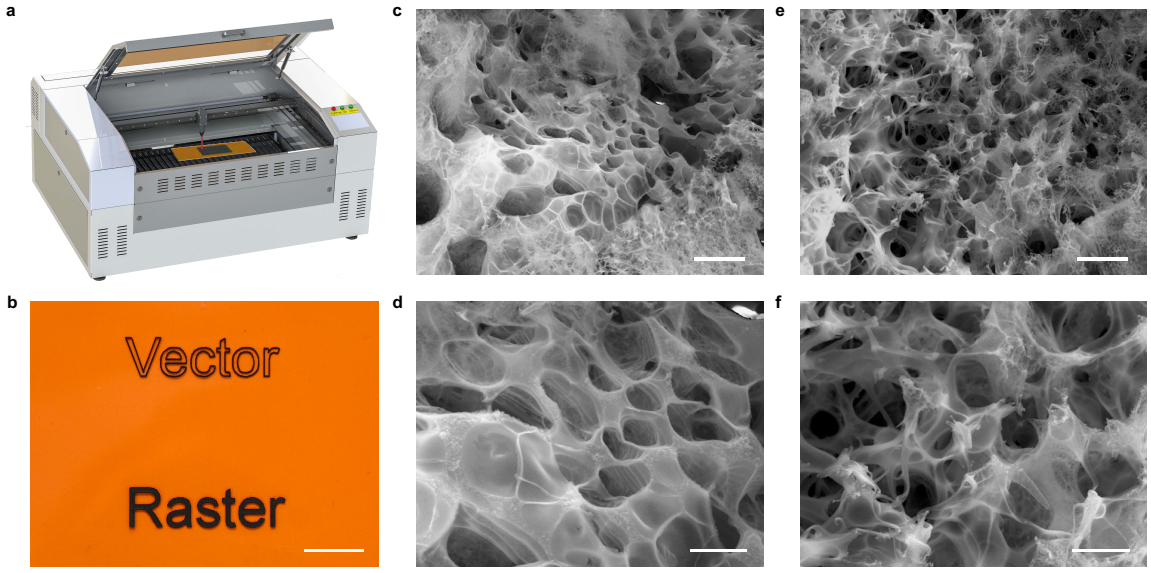

Figure A-1. Vector and raster modes of the laser cutting process. a, A CO_2 laser cutting machine. b, Optical image of laser-scribed graphene patterns via vector mode and raster mode, respectively. Scale bar, 1 cm. c,d, SEM images of vector mode-scribed graphene structure. Scale bars represent 5 μm (c) and 2 μm (d), respectively. e,f, SEM images of raster mode-scribed graphene structure. Scale bars represent 5 μm (e) and 2 μm (f), respectively.

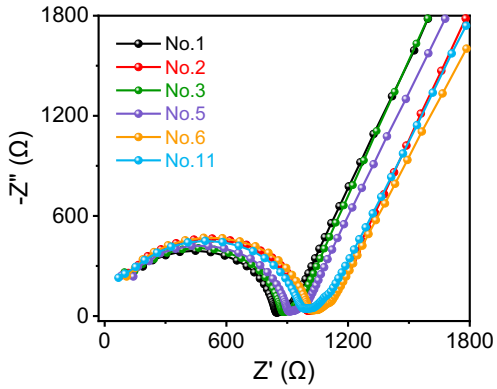

Figure A-2. Electrochemical impedance spectroscopy (EIS) for LEG-based electrodes prepared with different laser-engraving parameters. EIS tests were performed in a solution containing 0.2 M KCl and 5 mM $[Fe(CN)_6]^{3-}$ at open circuit potentials with an AC amplitude of 5 mV in the range of 0.1–1000000 Hz.

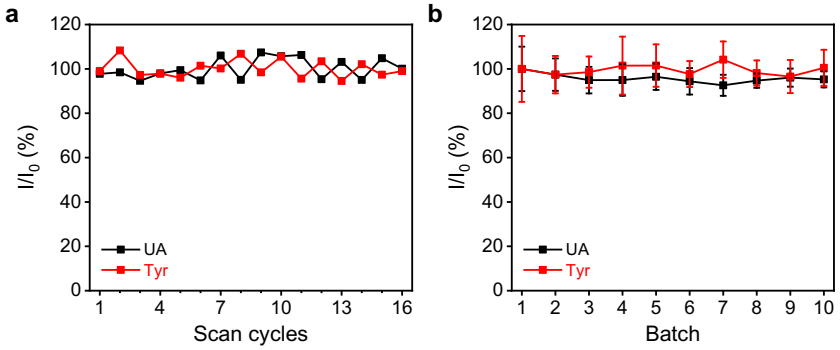

Figure A-3. Reproducibility of the LEG-based chemical sensors for Tyr and UA sensing. a, Continuous successive detection of UA and Tyr using an LEG-CS for 16 cycles. I and I_0 represent the peak amplitudes of the DPV plot obtained from a give scan cycle and the first cycle, respectively. b, Batch to batch variation of the LEG-based chemical sensor performance (10 batches). I and I_0 represent the peak amplitude of the DPV plot, and the average peak amplitude obtained from the first batch, respectively. Measure of the center is the mean value of each batch. Error bars represent the standard deviations of the peak amplitudes measured from 16 sensors. Conditions: 50 and 100 µM of UA and Tyr.

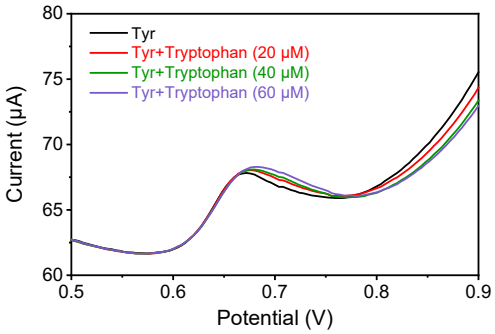

Figure A-4. The selectivity of the LEG-CS to Tyr over tryptophan. The DPV plots were obtained from solutions containing physiologically relevant levels of Tyr (170 µM) and tryptophan (20, 40 and 60 µM). The experiment was repeated 5 times independently with similar results.

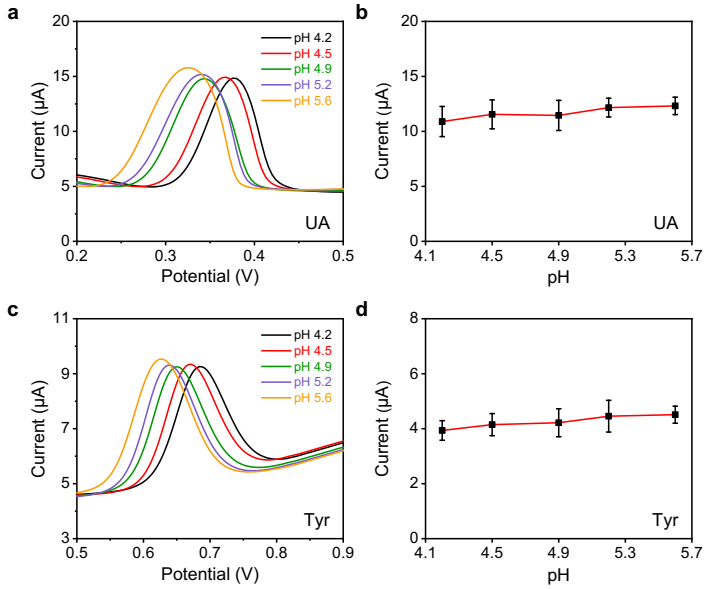

Figure A-5. The dependence of sensor response on the solution pH levels. **a**,**b**, The DPV responses (**a**) and the corresponding peak amplitudes (**b**) of the LEG-based chemical sensors (3 mm in diameter) for UA sensing in solutions with different pHs. **c**,**d**, The DPV responses (**a**) and the corresponding peak amplitudes (**b**) of the LEG-based chemical sensors for Tyr sensing in solutions with different pHs. To prepare the artificial sweat samples with different pH, lactic acid was used to adjust the pH of the PBS buffer (0.3X) solutions to physiologically relevant pHs. The UA and Tyr concentrations are 100 and 100 μM, respectively. Error bars represent the standard deviations of measurements from 5 sensors.

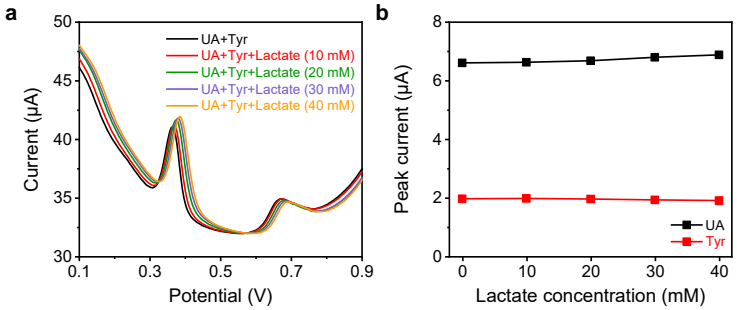

Figure A-6. The selectivity of the LEG-CS to lactate. Physiologically relevant levels of lactic acid (10, 20, 30, and 40 mM) were added to 0.1 M ABS (pH 4.6)

containing 50 µM UA and 50 µM Tyr. The experiment was repeated 5 times independently with similar results.

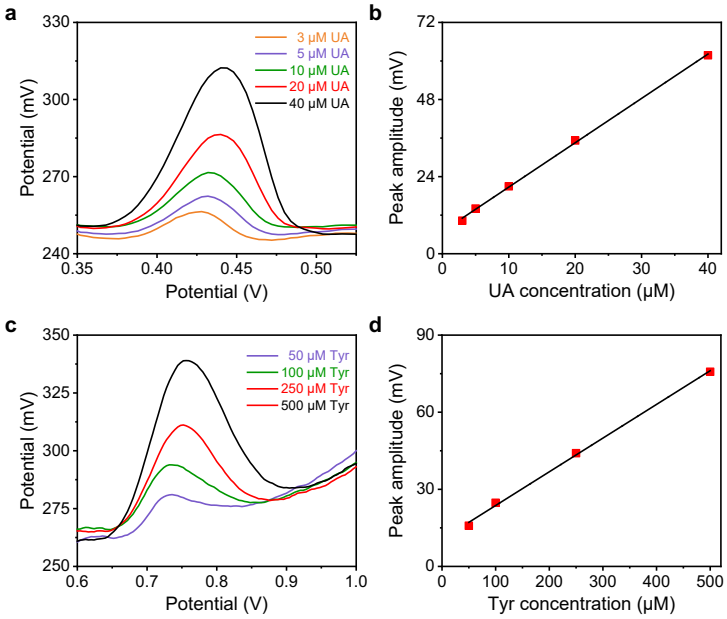

Figure A-7. Characterization and calibration of LEG-CS using the FPCB. a,b, DPV curves in ABS solutions containing varied UA concentrations (a) their corresponding

calibration curve (b). c,d, DPV curves of Tyr in ABS solutions containing varied Tyr concentrations (c) and their corresponding calibration curve (d). The experiment was repeated 5 times independently with similar results.

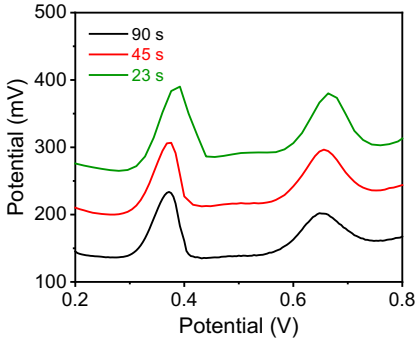

Figure A-8. Control of the DPV scan cycle lengths by varying the scan steps. Varied incremental potentials (4, 8, and 16 mV) were used to achieve the scan cycle

lengths of 90, 45, 23 seconds. Conditions, 50 µM UA and 250 µM Tyr. The experiment was repeated 5 times independently with similar results.

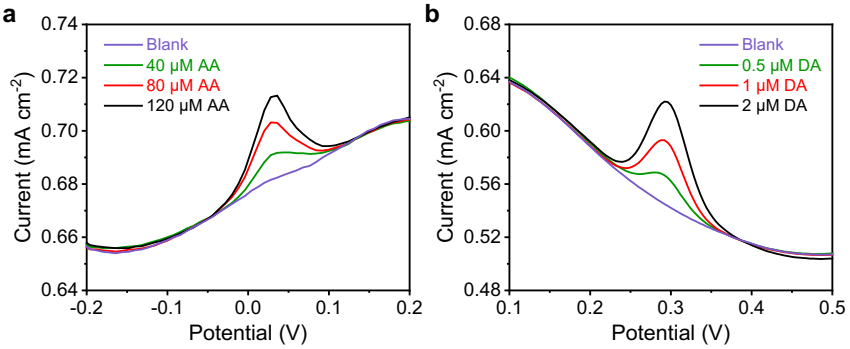

Figure A-9. Sensor performance for detection of ultra-low levels of other electroactive compounds. a,b, the LEG electrodes show excellent sensitivity to AA (40, 80, and 120 µM) (a) and DA (0.5, 1, and 2 µM) (b). A commercial Ag/AgCl was used as the reference electrode. The experiment was repeated 5 times independently with similar results.

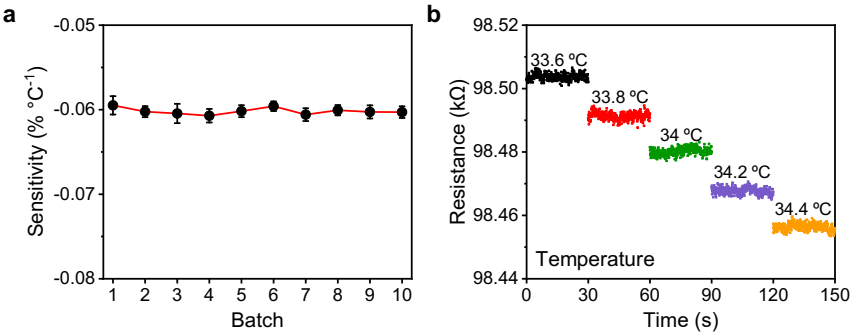

Figure A-10. Characterization of the LEG-based temperature sensors. a, Batch to

batch variation of the LEG-based temperature sensor performance (10 batches). Error bars

represent the standard deviations of 10 measurements from a temperature sensor; the mean of the 10 measurements is measure of the centre. b, The response of an LEG-

based temperature sensor to small temperature changes. The experiment was repeated 5 times independently with similar results.

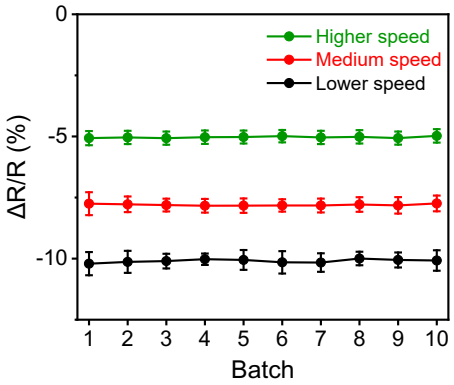

Figure A-11. Batch to batch variation of the LEG-based strain sensors prepared with varied laser scanning speeds. Error bars represent the standard deviations of 10

measurements from a strain sensor under 0.25% strain; the mean of the 10 measurements is the center of measure.

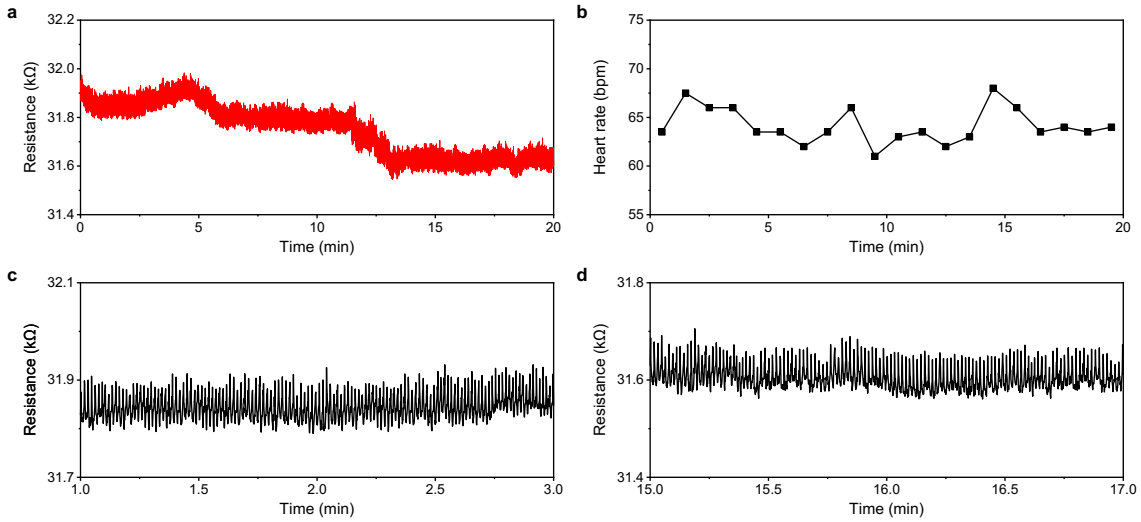

Figure A-12. Heart rate (HR) monitoring using an LEG-based strain sensor. a,b, The resistive response of an LEG-based strain sensor (a) and extracted heart rate information (b) during long term continuous pulse monitoring on a healthy subject. c,d, The resistive responses of the LEG-based strain sensor at 1–3 minutes and at 15–17 minutes during this test.

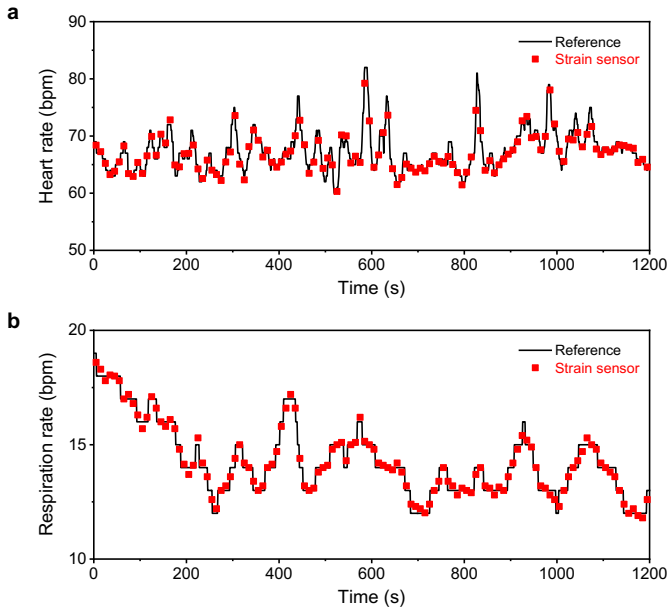

Figure A-13. Heart rate (HR) monitoring using an LEG-based strain sensor. a,b, The resistive response of an LEG-based strain sensor (a) and extracted heart rate information (b) during long term continuous pulse monitoring on a healthy subject. c,d, The resistive responses of the LEG-based strain sensor at 1–3 minutes and at 15–17 minutes during this test.

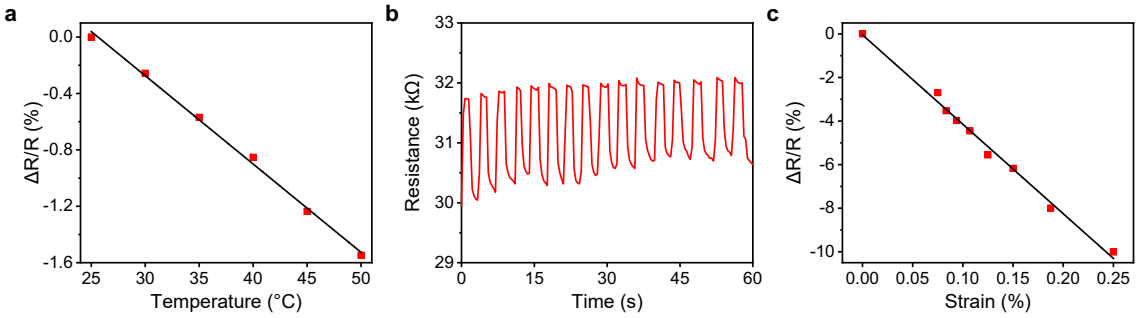

Figure A-14. Characterization and calibration of the temperature and strain sensors using the FPCB. a, Calibration curve for the temperature sensor. b,c, Characterization in response to pulsed strains (b) and the calibration plot of the strain sensor (c). Throughout the figure, the experiments were repeated 3 times independently and similar results were obtained.

Number	Constituents	Concentration (μM)	Number	Constituents	Concentration (μM)
1	Alanine	360	17	Lysine	150
2	Arginine	780	18	Methionine	50
3	Ascorbic acid	10	19	Nicotinic acid	50
4	Aspartic acid	340	20	Ornithine	150
5	Choline chloride	50	21	Pantothetic acid	50
6	Citrulline	400	22	Phenylalanine	130
7	Creatine	15	23	Pyridoxine	0.01
8	Creatinine	84	24	Riboflavin	50
9	Dehydroascorbic acid	11	25	Serine	50
10	Folic acid	50	26	Thiamine	50
11	Glutamic acid	370	27	Threonine	450
12	Glycine	390	28	Tryptophan	55
13	Histidine	520	29	Tyrosine	170
14	Inositol	1.6	30	Uric acid	60
15	Isoleucine	16	31	Valine	250
16	Leucine	210			

Table A-1. Sweat analytes and their concentrations used for the selectivity studies. The values were chosen based on the mean physiological levels of the analytes.[1]

Note A-1. The selectivity of the LEG-CS for sweat UA and Tyr sensing

Current wearable electrochemical sweat sensors are primarily focused on a limited number of electrolytes (e.g., Na^+, K^+ , Cl^-) and metabolites (e.g., lactate and glucose) at high concentrations (usually at mM levels) monitored via ion-selective sensors or enzymatic electrodes; biosensors based on bioreceptors (e.g., antibodies) could be highly sensitive, but usually require multiple washing steps and detection in standard buffer or redox solutions in order to transduce the bioaffinity interactions. The approach we utilize here for continuous monitoring of UA and Tyr is based on their selective oxidation reaction at a specific potential. The selectivity is based on the oxidation peak position for the LEG-CS. We evaluate here the selectivity of the LEG-CS over the common amino acids, vitamins and other potential interfering chemicals at physiologically relevant concentrations in human sweat listed in **Table A-1**. Our

electrochemical sensing data in **Figs. 3,4** show that the physiological level sweat analytes have minimal influence on the detection of UA and Tyr using the LEG-CS.

There are few electroactive molecules reported to be present in human sweat with comparable concentrations with UA and Tyr. Dopamine is a well-known electroactive neurotransmitter present at high concentration in cerebrospinal fluid. Our data in Fig. 1i shows that at the same conditions, the dopamine oxidation peak appears at a more negative potential than UA and doesn't affect the UA monitoring. In fact, to our knowledge, there is no literature report on the presence of dopamine in human sweat. Another electroactive molecule tryptophan has a close oxidation peak position to Tyr. However, tryptophan is present at a much lower concentration compared to Tyr. Our selectivity study (**Fig. A-4**) shows that physiologically relevant concentrations of tryptophan do not significantly affect our Tyr measurement.

As pH is usually a key factor that could influence electrochemical sweat sensor performance, we try to evaluate here the influence of pH on the sensor performance in artificial sweat (with pH values adjusted by varying lactic acid as lactic acid is the main contributing factors for sweat pH). Considering the normal sweat pH range in the literature and from our human subjects (pH ranges from 4 to 6), the dependence of the chemical sensor performance in artificial sweat with pHs between 4 to 6 was examined. Our results in **Fig. A-5** show that, although the oxidation peak positions slightly shift under different pHs, the peak amplitudes of UA and Tyr sensing remain stable in the range of pH 4 to pH 6. Considering that we are essentially measuring the peak heights, the influence of the pH is small to our sensors. Moreover, it is worth noting that the variations of pH values of an individual's sweat at different time points during biking session and at different biking sessions are small.

Bibliography of Appendix A

1. Harvey, C. J., LeBouf, R. F. & Stefaniak, A. B. Formulation and stability of a novel artificial human sweat under conditions of storage and use. *Toxicology in Vitro* **24**, 1790–1796 (2010).

Chapter 3

MOLECULAR IMPRINTED POLYMER-BASED LASER-ENGRAVED GRAPHENE SENSORS

Materials from this chapter appears in "Wang, M.; Yang, Y.; Min, J.; Song, Y.; Tu, J.; Mukasa, D.; Ye, C.; Xu, C.; Heflin, N.; McCune, J. S.; Hsiai, T. K.; Li, Z.; Gao, W. A wearable electrochemical biosensor for the monitoring of metabolites and nutrients. *Nature Biomedical Engineering* 1–11 (2022) doi: 10.1038/s41551-022-00916-z" .

3.1 Introduction

Circulating nutrients are essential indicators for overall health and body function. Amino acids (AAs), sourced from dietary intake and gut microbiota synthesis, and influenced by personal lifestyles, are important biomarkers for a number of health conditions (**Fig.3-1**). [1] Metabolic profiling and monitoring are a key approach to enabling precision nutrition and precision medicine.[2] Current gold standards in medical evaluation and metabolic testing heavily rely on blood analyses that are invasive and episodic, often requiring physical visits to medical facilities, labor-intensive sample processing and storage, and delicate instrumentation (for example, gas chromatography–mass spectrometry (GC–MS)).[3] As the current COVID-19 pandemic remains uncontrolled around the world, there is a pressing need for developing wearable and telemedicine sensors to monitor an individual's health state and to enable timely intervention under home- and community-based settings[4–10]; it is also increasingly important to monitor a person's long-term cardiometabolic and nutritional health status after recovery from severe COVID-19 infection using wearables to capture early signs of potential endocrinological complications such as T2DM.[11]

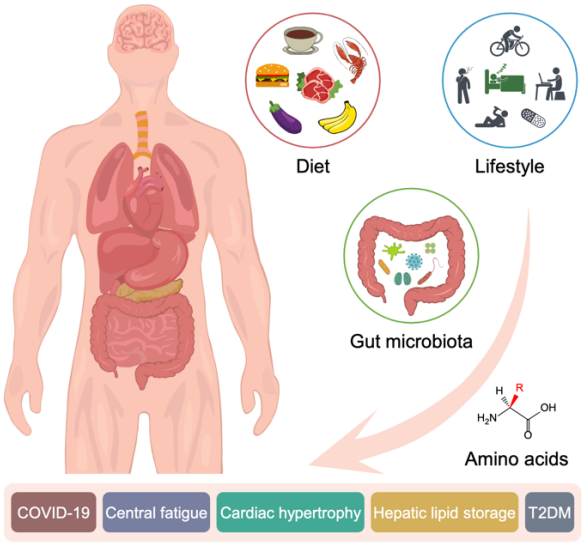

Figure 3-1. Circulating nutrients such as AAs are associated with various physiological and metabolic conditions.

Sweat is an important body fluid containing a wealth of chemicals reflective of nutritional and metabolic conditions.[10,12–14]The progression from blood analyses to wearable sweat analyses could provide great potential for non-invasive, continuous monitoring of physiological biomarkers critical to human health.[15–20] However, currently reported wearable electrochemical sensors focus primarily on a limited number of analytes including electrolytes, glucose and lactate, owing to the lack of a suitable continuous monitoring strategy beyond ion-selective and enzymatic electrodes or direct oxidation of electroactive molecules.[12–14,19,20] Thus, most clinically relevant nutrients and metabolites in sweat are rarely explored and undetectable by existing wearable sensing technologies.

In this chapter, we present a universal wearable biosensing strategy based on a judicious combination of the mass-producible laser-engraved graphene (LEG), electrochemically synthesized redox-active nanoreporters (RARs) and molecularly imprinted polymer (MIP)-based 'artificial antibodies', as well as unique in situ regeneration and calibration technologies. Unlike bio-affinity sensors based on antibodies or classic MIPs, which are generally for one-time use and require multiple washing steps to transduce the bio-affinity interactions in standard ionic solutions[21,22] , this approach enables the demonstration of sensitive, selective and continuous monitoring of a wide range of trace-level biomarkers in biofluids including all nine essential AAs as well as vitamins, metabolites and lipids commonly found in human sweat.

3.2 Materials and Methodology

Methodology of Sensing Electroactive Targets

For electroactive molecules in sweat, the oxidation of bound target molecules in the MIP template can be directly measured by differential pulse voltammetry (DPV) in

which the peak current height correlates with analyte concentration (**Fig. 3-2a**). Considering that multiple electroactive molecules can be oxidized at similar potentials, this LEG–MIP approach addresses both sensitivity and selectivity issues.

Methodology of Sensing non-Electroactive Targets

As the majority of metabolites and nutrients (for example, BCAAs) are non-electroactive and cannot easily be oxidized under operational conditions, we herein utilize an indirect detection approach involving a redox-active nanoreporter(s) (RAR) layer sandwiched between the LEG and MIP layers to enable rapid quantitation (**Fig. 3-2e**). The selective adsorption of the target molecules onto the imprinted polymeric layer decreases the exposure of the RAR to the sample matrix. Controlled-potential voltammetric techniques such as DPV or linear sweeping voltammetry (LSV) can be applied to measure the RAR's oxidation or reduction peak, where the decrease in peak height current density corresponds to an increase in analyte levels. Considering that a total level of multiple nutrients (for example, total BCAAs) is often an important health indicator, a multi-template MIP approach can be used to enable accurate and sensitive detection of the total concentration of multiple targets with a single sensor (**Fig.3-2i**).

Materials and reagents

Uric acid, l-tyrosine, silver nitrate, iron(III) chloride, dopamine hydrochloride, choline chloride, creatinine, pantothenic acid calcium salt, citrulline, pyridoxine and lactic acid were purchased from Alfa Aesar. Sodium thiosulfate pentahydrate, sodium bisulfite, tryptophan, leucine, alanine, isoleucine, methionine, valine, lysine, thiamine hydrochloride, serine, sulfuric acid, hydrochloric acid, AQCA, 3-aminophenylboronic acid (APBA), aniline, *o*-phenylenediamine, methylene blue, thionine, 2-(*N*-morpholino)ethanesulfonic acid hydrate (MES), ethanolamine, *N*-(3-dimethyl-aminopropyl)-*N*′-ethylcarbodiimide (EDC), *N*-hydroxysulfosuccinimide sodium salt (sulfo-NHS), bovine serum albumin (BSA),

tris(hydroxymethyl)aminomethane hydrochloride (Tris–HCl), streptavidin–peroxidase conjugate (Roche) and hydroquinone were purchased from Sigma-Aldrich. Carboxylic-acid-modified magnetic beads (MBs; Dynabeads, M-270) were obtained from Invitrogen. Potassium ferricyanide and potassium ferrocyanide were purchased from Acros Organics. Acetic acid, methanol, sodium acetate, sodium chloride, sodium dihydrogen phosphate, potassium chloride, potassium hydrogen phosphate, urea, l-ascorbic acid and dextrose (d-glucose) anhydrous, glycine, arginine, inositol, ornithine, aspartic acid, threonine, histidine, riboflavin, creatine, phenylalanine, nicotinic acid, folic acid, glutamic acid and hydrogen peroxide (30% (w/v)) were purchased from Thermo Fisher Scientific. Insulin capture antibody and biotinylated detector antibody were purchased from R&D systems (Human/Canine/Porcine Insulin DuoSet ELISA). Screen printed carbon electrodes and magnetic holder were purchased from Metrohm DropSens. Medical adhesives were purchased from 3 M and Adhesives Research. PI films (75 μm thick) were purchased from DuPont. PET films (12 μm thick) were purchased from McMaster-Carr.

Fabrication and preparation of the LEG sensors

The LEG electrodes were fabricated on a PI film with a thickness of 75 μm (DuPont) with a 50 W CO_2 laser cutter (Universal Laser System). When engraving the PI with a CO_2 laser cutter, the absorbed laser energy is converted to local heat and thus leads to a high localized temperature (>2,500 °C), chemical bonds in the PI network are broken and thermal re-organization of the carbon atoms occurs, resulting in sheets of graphene structures. The optimized parameters for the graphene electrodes and electronic connections were power 8%, speed 15%, and points per inch (PPI) 1,000 in raster mode with three-time scan. For the active sensing area of the temperature sensor, the optimized parameters were power 3%, speed 18%, and PPI 1,000 in vector mode with one-time scan. To prepare the reference electrode, Ag was first modified on the corresponding graphene electrode by multi-current electrodeposition with electrochemical workstation (CHI 832D) at −0.01 mA for

150 s, −0.02 mA for 50 s, −0.05 mA for 50 s, −0.08 mA for 50 s and −0.1 mA for 350 s using a plating solution containing 0.25 M silver nitrate, 0.75 M sodium thiosulfate and 0.5 M sodium bisulfite. To obtain the Ag/AgCl electrode, 0.1 M $FeCl_3$ solution was further dropped on the Ag surface for 30 s, and then 3 µl polyvinyl butyral (PVB) reference cocktail prepared by dissolving 79.1 mg of PVB and 50 mg of NaCl in 1 ml of methanol was dropped on the Ag/AgCl electrode and dried overnight. The Na^+-selective electrode was prepared as follows: 0.6 µl of Na^+-selective membrane cocktail prepared by dissolving 1 mg of Na ionophore X, 0.55 mg sodium tetrakis[3,5-bis(trifluoromethyl)phenyl]borate, 33 mg polyvinyl chloride and 65.45 mg bis(2-ethylhexyl) sebacate into 660 µl of tetrahydrofuran was drop-casted onto the graphene electrode and dried overnight. To obtain the desired stable Na^+-sensing performance for long-term continuous measurements, the obtained Na^+ sensor was conditioned overnight in 100 mM NaCl.

The fabrication process of the LEG–MIP sensor array is illustrated in **Fig. 3-3**. All the MIP layers are synthesized by electro-polymerization. The polymerization solution was prepared by dissolving 5 mM template (for example, target AA), 12.5 mM APBA and 37.5 mM pyrrole into 0.01 M phosphate-buffered saline (PBS) (pH 6.5). For multi-MIP BCAA sensor, 5 mM of each target (that is, Leu, Ile and Val) was used. Before MIP deposition, the LEG was activated in 0.5 M H_2SO_4 with CV scans for 60 segments (−1.2 to 1 V with a scan rate of 500 mV s^{-1}). For the direct-detection LEG–MIP sensors, the target imprinted polymer was electrochemically synthesized on the LEG electrode with CV deposition (0–1 V for ten cycles, 50 mV s^{-1}) using the prepared polymerization solution. The target molecules were extracted by soaking the electrode into an acetic acid/methanol mixture (7:3 v/v) for 1 h. Subsequently, the resulting electrode was immersed into 0.01 M PBS (pH 6.5) for repetitive CV scans (0.4–1 V with a scan rate of 50 mV s^{-1}) until a stable response was obtained. For LEG-non-imprinted polymer, the electrode was prepared following the same procedure as LEG–MIP except that no template was added in the polymerization solution.

For the indirect-detection MIP sensors, electrochemically synthesized RARs (for example, PBNPs or AQCA) were first modified on the LEG electrode. The PBNP RAR on the LEG was prepared with CV (20 cycles) (−0.2 to 0.6 V with a scan rate of 50 mV s^{-1}) in an aqueous solution containing 3 mM $FeCl_3$, 3 mM $K_3Fe(CN)_6$, 0.1 M HCl and 0.1 M KCl. A PBNP layer with appropriate redox signal is necessary to produce a good sensitivity for the final MIP sensors; to achieve this stable and suitable redox signal, the LEG electrode was rinsed with distilled water after the initial Prussian blue (PB) deposition, and the PB electrodeposition step was repeated two more times until a stable 70 µA LSV peak in 0.1 M KCl solution was achieved. Subsequently, the LEG–PB was rinsed with distilled water and immersed in a solution containing 0.1 M HCl and 0.1 M KCl for repetitive CV scans (−0.2 to 0.6 V with a scan rate of 50 mV s^{-1}) until a stable response was obtained. To prepare the AQCA RAR on the LEG, the LEG electrode was first incubated in 50 µl PBS (pH 6.5) with 5 mM AQCA at 4 °C overnight. Subsequently, the LEG–AQCA was rinsed with distilled water and immersed into a phosphate buffer solution for repetitive CV scans (−0.8 to 0 V with a scan rate of 50 mV s^{-1}) until a stable response was obtained. For the indirect-detection LEG–PB–MIP sensors, an additional PB activation process was conducted right after the template extraction (IT scan at 1 V in 0.5 M HCl for 600 s), followed by an LEG–PB–MIP sensor stabilization process in 0.1 M KCl (CV scans at −0.2 to 0.6 V with a scan rate of 50 mV s^{-1}). It should be noted that, for the LEG–AQCA–MIP sensor, only three CV cycles of polymerization were used to prepare the MIP layer, and the sensor was stabilized in 0.01 M PBS (pH 6.5) (CV scans at −0.8 to 0 V with a scan rate of 50 mV s^{-1}).

The morphology of materials was characterized by scanning electron microscopy (Nova Nano SEM 450) and transmission electron microscopy (Talos S-FEG FEI, USA). The Raman spectrum of the electrodes with different modification was recorded using a 532.8 nm laser with an inVia Reflex (Renishaw). Fourier-transform infrared spectra were measured using infrared spectrometry (Nicolet 6700).

Characterization of the LEG sensor performance

A set of electrochemical sensors were characterized in solutions of target analytes. All the in vitro sensor characterizations were performed through CHI 832D. The response of the Na^+ sensor was characterized with open circuit potential measurements in the solutions containing varied Na^+ levels. DPV analysis was performed for all the direct-detection LEG–MIP sensor characterizations in 0.01 M PBS (pH 6.5) or in raw sweat. The DPV conditions were as follows: range, 0.4–1 V; incremental potential, 0.01 V; pulse amplitude, 0.05 V; pulse width, 0.05 s; pulse period, 0.5 s; and sensitivity, 1×10^{-5} A V^{-1}. For in vitro indirect detection of the target molecules based on the LEG–PB–MIP sensors, LSV analysis (0.4–0 V) was performed in 0.1 M KCl. The LSV conditions were as follows: range, 0.4–0 V; scan rate, 0.005 V s^{-1}; sample interval, 0.001 V; quiet time, 2 s; and sensitivity, 1×10^{-4} A V^{-1}. For in vitro indirect detection of the target molecules based on the LEG–AQCA–MIP sensors, negative DPV analysis (0 to −0.8 V) was performed in 0.01 M PBS. The negative DPV conditions were as follows: 0 to −0.8 V; incremental potential, 0.01 V; pulse amplitude, 0.05 V; pulse width, 0.05 s; pulse period, 0.5 s; and sensitivity, 1×10^{-5} A V^{-1}.

To evaluate the performance of the various electrode substrates for MIP-based AA sensing, LEG, printed carbon electrode, Au electrode and glassy carbon electrode were chosen. The glassy carbon electrodes were purchased from CH Instruments. The printed carbon electrodes were printed on the PI substrate using a Dimatix Materials Printer DMP-2850 (Fujifilm, Minato, Japan) with a commercial carbon ink from NovaCentrix. The Au electrodes were fabricated via E-beam evaporation: 20 nm of Cr and 100 nm of Au were deposited onto an O_2-plasma pre-treated PET substrate. MIP films were prepared with CV deposition (0–1 V for ten cycles, 50 mV s^{-1}).

GC–MS analysis for sensor validation

GC–MS analysis of the AAs in sweat and serum samples was performed using EZ:Faast kit from Phenomenex, which enables sample preparation, derivatization

and GC–MS analysis of free AAs. A Varian Saturn 2000 was used for the GC–MS runs. One microlitre of prepared sample solution was injected for GC in helium carrier gas at 1.0 ml min^{-1} constant flow with a pulse pressure of 20 pounds per square inch for 0.2 min, with the oven programmed from 110 °C to 320 °C at 32 °C min^{-1}. The mass chromatography was set with source at 240 °C, quad at 180 °C and auxiliary at 310 °C with a scan range of 45–450 *m*/*z* at a sampling rate of 3.5 scans s^{-1}. Selected ion monitoring was used, which records the ion current at selected masses that are characteristic of the certain AA in an expected retention time.[23] For example, after the derivatization of the EZ:Faast kit, Trp has a characteristic mass at 130 with a retention time at around 5.1 min, and peak height is recorded for Trp measurements at ion number 130 and at 5.1 min from the raw data spectrum. The internal standard (IS; norvaline) was added during the sample derivatization process to account for potential evaporation-induced increase in peak detection; the IS norvaline peak height is recorded at its ion number 158 at 1.65 min (**Appendix B, Fig. B-13**). The Trp peak height recorded from raw data spectrum was calibrated with respect to the IS in the same run: normalized Trp peak height = Trp peak height/IS peak height. With normalized peak heights of different levels of Trp standards, calibration plots were constructed. For other samples, the normalized peak height of Trp was used to calculate the concentration.

3.3 Results and Discussion

Biosensor design and evaluation for universal metabolic and nutritional analysis

Universal detection of AAs and other metabolites/nutrients with high sensitivity and selectivity was achieved through careful design of the selective binding MIP layer on the LEG. MIPs are chemically synthesized receptors formed by polymerizing functional monomer(s) with template molecules. Although MIP technology has been proposed for sensing, separation and diagnosis[22,24], it has not yet been demonstrated for continuous wearable sensing as classic MIP sensors require washing steps for sensor regeneration and the detection is generally performed in standard buffer or redox solutions. In our case, the functional monomer (for example, pyrrole) and

crosslinker (for example, APBA) initially form a complex with the target molecule; following polymerization, their functional groups are embedded in the polymeric structure on the LEG (**Appendix B, Fig. B-1**); subsequent extraction of the target molecules reveals binding sites on the LEG-MIP electrode that are complementary in size, shape, and charge to the target analyte (**Figs. 3-2,3-3**).

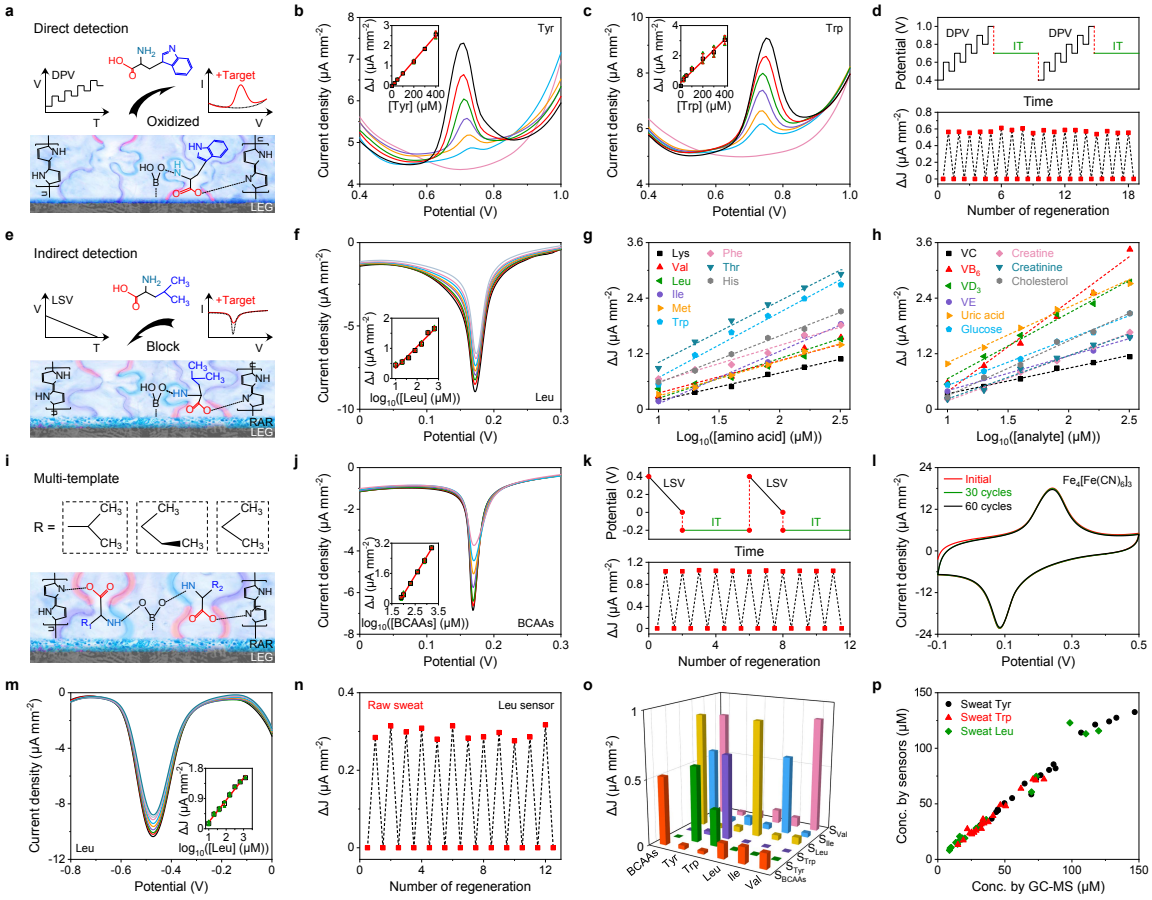

Figure 3-2. Schematics and characterizations of the biomimetic LEG-MIP sensors. a, Direct detection of electroactive molecules using LEG-MIP sensors. **b**,**c**, DPV voltammograms of the LEG-MIP sensors for direct Tyr (**b**) and Trp (**c**) detection. Insets, the calibration plots. ΔJ, peak height current density. **d**, *In situ* continuous sensing and regeneration of an LEG-MIP Trp sensor in 50 μM Trp. **e**, Indirect molecular detection using LEG-RAR-MIP sensors. **f**, LSV voltammograms of indirect Leu detection with LEG-PBNP-MIP sensors. Inset, the calibration plot. **g**,**h**, Indirect detection of all essential AAs (**g**) and multiple vitamins, lipids, and

metabolites (**h**) using LEG-PBNP-MIP sensors. **i**, Schematic of multi-MIP AA sensors. **j**, LSV voltammograms of a LEG multi-MIP sensor for BCAA quantification. Inset, the calibration plot. **k**, *In situ* continuous sensing and regeneration of an LEG-PBNP-MIP Leu sensor in 50 μM Leu. **l**, Repetitive CV scans of an LEG-PBNP electrode in 0.1 M KCl. **m**, DPV voltammograms of indirect Leu detection with LEG-AQCA-MIP sensors. Inset, the calibration plot. **n**, *In situ* regeneration of an LEG-AQCA-MIP Leu sensor in a raw sweat sample. **o**, Selectivity of the Trp, Tyr, Leu, Ile, Val, and BCAA sensors against other AAs. **p**, Validation of Tyr, Trp, and Leu sensors for analyzing raw exercise sweat samples (n=20) against GC-MS. All error bars represent the s.d. from 3 sensors.

Two detection strategies—direct and indirect—are designed on the basis of the electrochemical properties of the target molecules (**Fig. 3-2a,e, Fig. 3-3**). Optimizations and characterizations of the LEG–MIP sensors are detailed in **Appendix B, Note B-1** and **Fig. B-2-6**.

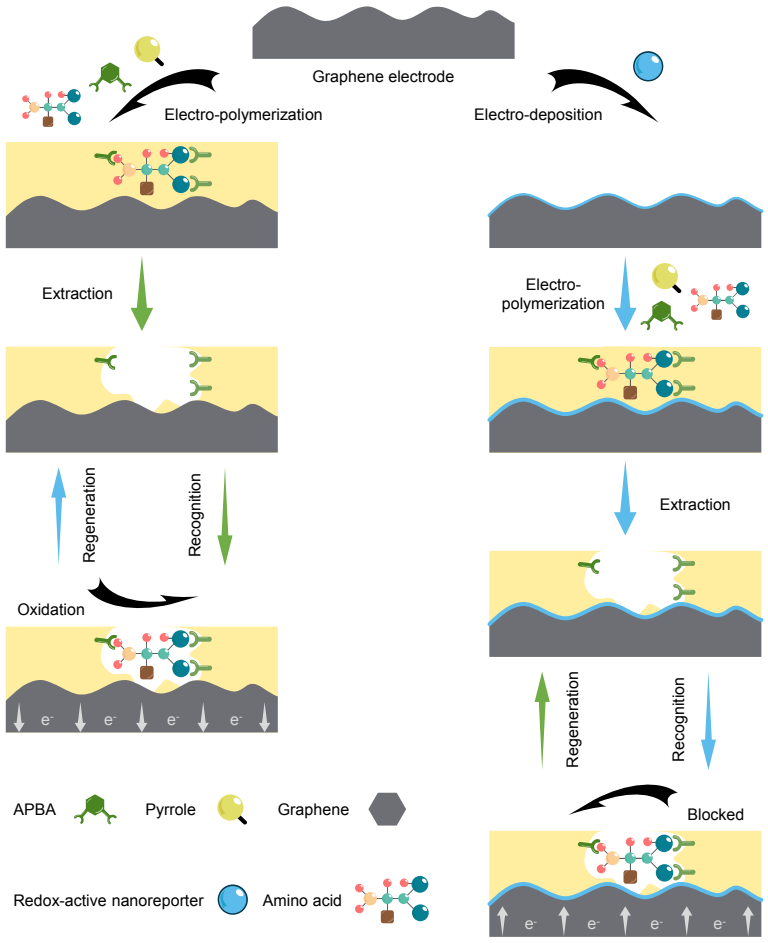

Figure 3-3. Schematic of the preparation procedure and detection mechanism of the LEG-MIP AA sensors. Left panel, electroactive AA sensor with direct detection mechanism; Right panel, AA sensor with indirect detection mechanism.

For electroactive molecules in sweat, (e.g. Tyr and Trp) , two AAs with close redox potentials (~0.7 V), could be detected selectively with this strategy (**Fig. 3-2b,c** and **Fig. 3-4**).

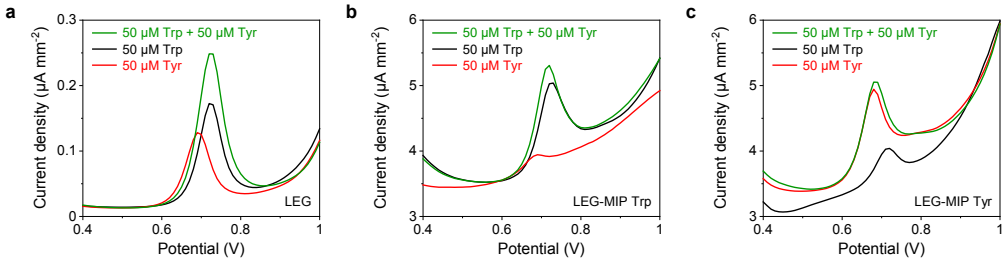

Figure 3-4. Selectivity studies of the LEG-MIP sensors for detecting two electroactive amino acids: Trp and Tyr. a–**c**, DPV voltammograms of a bare LEG electrode (**a**), an LEG-MIP Trp electrode (**b**), and an LEG-MIP Tyr electrode (**c**) in 50 μM Trp, 50 μM Tyr, and 50 μM Trp + 50 μM Tyr.

Linear relationships between peak height current densities and target concentrations with sensitivities of 0.63 μA μM^{-1} cm^{-2} and 0.71 μA μM^{-1} cm^{-2} respectively for the LEG–MIP Tyr and Trp sensors were observed (**Fig. 3-5**).

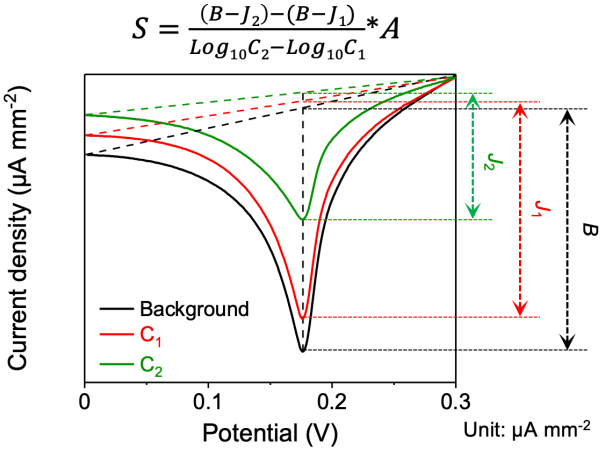

Figure. 3-5. Schematic illustration of the sensitivity calculation of the LEG-RAR-MIP sensor. S, sensitivity of the sensor; B, background peak current height; A, the electrode area; J_1 and J_2: peak current height of the LSV obtained in the presence of the analyte with concentrations of C_1 and C-2, respectively.

It is worth noting that choices of monomer/crosslinker/template ratios and incubation periods have substantial influences on sensor response while sample volume does not (**Fig. 3-6**). The Tyr and Trp sensors can be readily and repeatably regenerated in situ without any washing step with a high-voltage amperometry current–time (*IT*) that oxidizes the bound targets at their redox potentials (**Fig. 3-2d**).

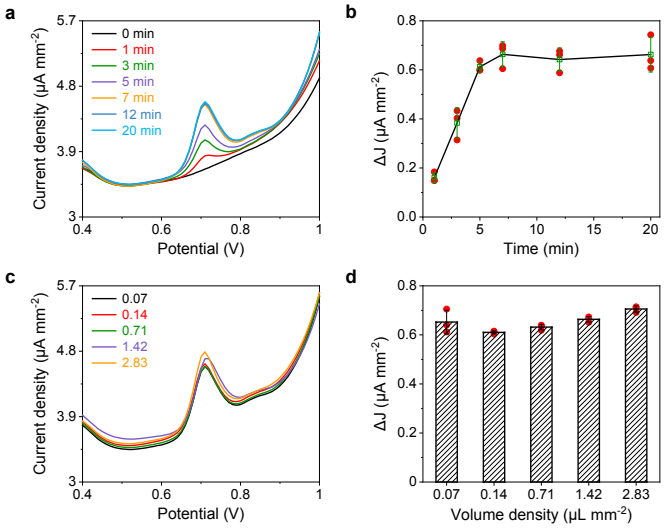

Figure 3-6. Evaluation of the effect of incubation time and sample volume on the LEG-MIP sensor performance. a,**b**, DPV voltammograms (**a**) and current density of the peak height (ΔJ) (**b**) of the Trp sensors in 50 μM Trp with varied 1–20 min incubation time. **c**,**d**, DPV voltammograms (**c**) and current density of the peak height (ΔJ) (**d**) of the Trp sensors in 50 μM Trp with varied sample volumes. Error bars in **b** and **d** represent the s.d. from 3 sensors.

For non-electroactive targets such as BCAAs, an indirect detection approach was utilized involving an RAR layer sandwiched between the LEG and MIP layers. The selective adsorption of the target molecules onto the imprinted polymeric layer decreases the exposure of the RAR to the sample matrix. Controlled-potential voltammetric techniques such as DPV or linear sweeping voltammetry (LSV) can be applied to measure the RAR's oxidation or reduction peak, where the decrease in peak height current density corresponds to an increase in analyte levels. For

example, using Prussian Blue nanoparticles (PBNPs) as the RAR, we developed an MIP–LEG Leu sensor with a log-linear relationship between the peak height decrease and Leu concentration and a sensitivity of 702 nA mm^{-2} per decade of concentration (**Fig. 3-2f**). We established this approach to quantify the physiologically relevant range of all nine essential AAs (that is, Leu, Ile, Val, Trp, Phe, histidine (His), lysine (Lys), methionine (Met) and threonine (Thr)) (**Fig. 3-2g** and **Appendix B, Fig. B-7**) as well as a number of vitamins, metabolites and lipids (vitamins B-6, C, D_3 and E, glucose, uric acid, creatine, creatinine and cholesterol) (**Fig. 3-2h** and **Appendix B, Fig. B-8**). In addition to these nutrients and metabolites, this approach can be easily reconfigured to enable the monitoring of a broad spectrum of biomarkers ranging from hormones (for example, cortisol) to drugs (for example, immunosuppressive drug mycophenolic acid) (**Appendix B, Fig. B-9** and **Table B-1 and 2**). Most of these targets are undetectable continuously by any existing wearable technology. Considering that a total level of multiple nutrients (for example, total BCAAs) is often an important health indicator, a multi-template MIP approach can be used to enable accurate and sensitive detection of the total concentration of multiple targets with a single sensor (**Fig. 3-2i,j**). These indirect LEG–RAR–MIP sensors can be regenerated in situ by applying constant potential to the working electrode, which repels the bound target molecules from the MIP layer, achieving prolonged re-usability (**Fig. 3-2k**).

The LEG–MIP sensors show stable responses during repeatable use: the PBNP-based RAR showed stable redox signals throughout 60 repetitive cyclic voltammetry (CV) scans (**Fig. 3-2l** and **Appendix B, Fig. B-5**). Compared with traditional MIP preparation processes, the electrodeposited MIP layer on the mass-producible LEG leads to high reproducibility in selectivity, sensitivity and device-to-device consistency (**Appendix B, Fig. B-10 and 11**). The choice of LEG as the MIP deposition substrate also showed advantages in sensor sensitivity compared with classic electrodes such as glassy carbon electrode, printed carbon electrode and Au electrode (**Fig. 3-7**).

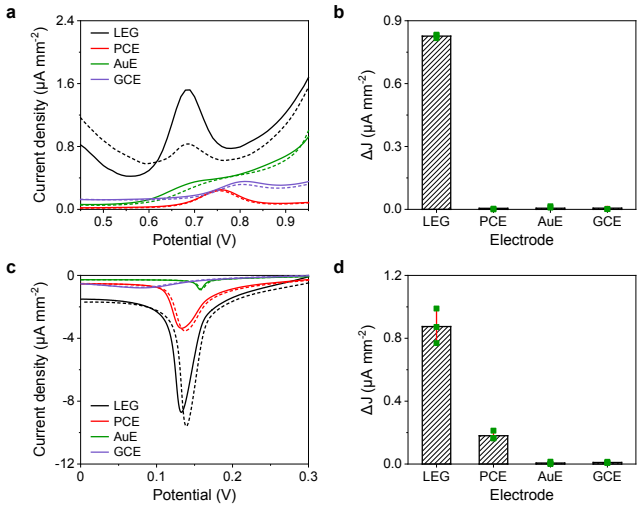

Figure 3-7. Comparison of the performance of the MIP sensors based on different electrodes: LEG, printed carbon electrode (PCE), Au electrode (AuE), and glassy carbon electrode (GCE). a,b, DPV voltammograms **(a)** and ΔJ (**b**) of the Trp MIP sensors before (dotted line) and after (solid line) incubation in 50 μM Trp. **c,d,** LSV voltammograms **(c)** and ΔJ (**d**) of the Leu PB-MIP sensors before (dotted line) and after (solid line) incubation in 50 μM Leu. Error bars represent the s.d. from 3 electrodes.

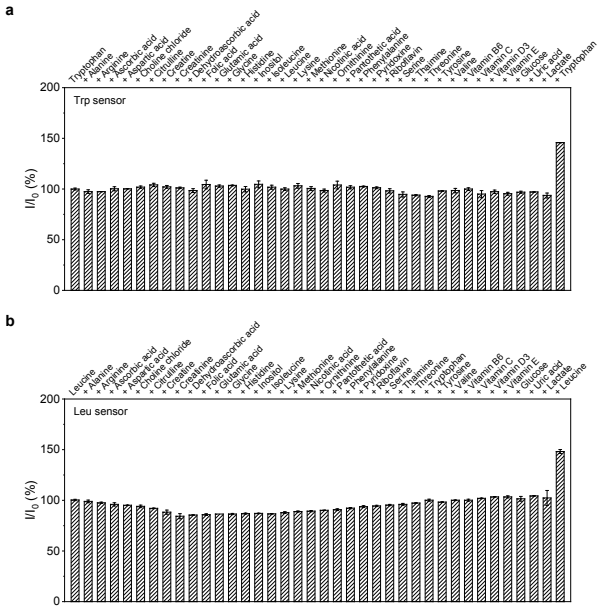

Figure 3-8. Selectivity of the LEG-MIP Trp sensors and the LEG-PB-MIP Leu sensors over other major analytes in human sweat. a,**b**, The selectivity of the Trp LEG-MIP sensors (**a**) and the Leu LEG-MIP sensors (**b**). I and I_0 represent the peak amplitude obtained from the LEG-MIP sensors, and the average peak amplitude obtained from the starting target solution, respectively. The concentrations of the initial Trp, Leu and other sweat analytes are based on **Appendix B, Table B-2**. Trp and Leu concentrations were increased by 50% in the end. Error bars represent the s.d. from 3 independent measurements.

Other RARs such as anthraquinone-2-carboxylic acid (AQCA) can also be used for indirect AA sensing with stable performance (negatively scanned DPV was used here to monitor AQCA reduction) (**Fig. 3-2m** and **Appendix B, Fig. B-12**). As illustrated in **Fig. 3-2n**, the LEG–AQCA–MIP sensors could be directly regenerated in a raw human sweat sample, resolving a main bottleneck of wearable biosensing. The MIP–LEG AA sensors have excellent selectivity for other analytes in sweat (including AAs with similar structures) at physiologically relevant concentrations (**Fig. 3-2o**, **Fig. 3-8**, and **Appendix B, Table B-2**). The LEG–MIP technology showed a comparable sensitivity with the current gold-standard laboratory-based GC–MS[25]; the sensor measurements in raw human sweat samples have been validated against GC–MS (**Fig.3-2p** and **Appendix B, Fig. B-13,14**).

3.4 Conclusion

As current wearable electrochemical sensors are limited to a narrow range of detection targets owing to lack of continuous sensing strategies beyond ion-selective and enzymatic electrodes. Though various bio-affinity-based sensors have been developed to detect a broader spectrum of targets using antibodies or MIPs, they generally require multiple washing steps or provide only one-time use; these limitations have hampered their useability in wearable devices. By integrating mass-producible LEG, electrochemically synthesized RARs and ‘artificial antibodies’, we have demonstrated a powerful universal wearable biosensing strategy that can achieve selective detection of a broad range of biomarkers (including all essential

AAs, vitamins, metabolites, lipids, hormones and drugs) and reliable in situ regeneration.

Bibliography of Chapter 3

1. Wu, G. Amino acids: metabolism, functions, and nutrition. *Amino Acids* **37**, 1–17 (2009).
2. Wishart, D. S. Emerging applications of metabolomics in drug discovery and precision medicine. *Nature Reviews Drug Discovery* **15**, 473–484 (2016).
3. Dettmer, K., Aronov, P. A. & Hammock, B. D. Mass spectrometry-based metabolomics. *Mass Spectrometry Reviews* **26**, 51–78 (2007).
4. Ray, T. R. *et al.* Bio-integrated wearable systems: a comprehensive review. *Chemical Reviews* **119**, 5461–5533 (2019).
5. Hollander, J. E. & Carr, B. G. Virtually Perfect? Telemedicine for Covid-19. *New England Journal of Medicine* **382**, 1679–1681 (2020).
6. Ni, X. *et al.* Automated, multiparametric monitoring of respiratory biomarkers and vital signs in clinical and home settings for COVID-19 patients. *Proceedings of the National Academy of Sciences* **118**, e2026610118 (2021).
7. Jeong, H. *et al.* Differential cardiopulmonary monitoring system for artifact-canceled physiological tracking of athletes, workers, and COVID-19 patients. *Science Advances* **7**, eabg3092 (2021).
8. Sempionatto, J. R. *et al.* An epidermal patch for the simultaneous monitoring of haemodynamic and metabolic biomarkers. *Nature Biomedical Engineering* **5**, 737–748 (2021).

9. Xu, C., Yang, Y. & Gao, W. Skin-interfaced sensors in digital medicine: from materials to applications. *Matter* **2**, 1414–1445 (2020).

10. Heikenfeld, J. *et al.* Accessing analytes in biofluids for peripheral biochemical monitoring. *Nature Biotechnology* **37**, 407–419 (2019).

11. Stefan, N., Birkenfeld, A. L. & Schulze, M. B. Global pandemics interconnected — obesity, impaired metabolic health and COVID-19. *Nature Reviews Endocrinology* **17**, 135–149 (2021).

12. Bariya, M., Nyein, H. Y. Y. & Javey, A. Wearable sweat sensors. *Nature Electronics* **1**, 160–171 (2018).

13. Yang, Y. & Gao, W. Wearable and flexible electronics for continuous molecular monitoring. *Chemical Society Reviews* **48**, 1465–1491 (2019).

14. Kim, J., Campbell, A. S., de Ávila, B. E.-F. & Wang, J. Wearable biosensors for healthcare monitoring. *Nature Biotechnology* **37**, 389–406 (2019).

15. Gao, W. *et al.* Fully integrated wearable sensor arrays for multiplexed in situ perspiration analysis. *Nature* **529**, 509–514 (2016).

16. Emaminejad, S. *et al.* Autonomous sweat extraction and analysis applied to cystic fibrosis and glucose monitoring using a fully integrated wearable platform. *Proceedings of the National Academy of Sciences of the United States of America.* **114**, 4625–4630 (2017).

17. Torrente-Rodríguez, R. M. *et al.* Investigation of cortisol dynamics in human sweat using a graphene-based wireless mhealth system. *Matter* **2**, 921–937 (2020).

18. Ray, T. R. *et al.* Soft, skin-interfaced sweat stickers for cystic fibrosis diagnosis and management. *Science Translational Medicine* **13**, eabd8109 (2021).

19. Lee, H. *et al.* A graphene-based electrochemical device with thermoresponsive microneedles for diabetes monitoring and therapy. *Nature Nanotechnology* **11**, 566–572 (2016).

20. Kim, J. *et al.* Noninvasive alcohol monitoring using a wearable tattoo-based iontophoretic-biosensing system. *ACS Sensors* **1**, 1011–1019 (2016).

21. Wang, J. Electrochemical biosensors: Towards point-of-care cancer diagnostics. *Biosensors and Bioelectronics* **21**, 1887–1892 (2006).

22. Uzun, L. & Turner, A. P. F. Molecularly-imprinted polymer sensors: realising their potential. *Biosensors and Bioelectronics* **76**, 131–144 (2016).

23. Sparkman, O. D., Penton, Z. & Kitson, F. G. *Gas chromatography and mass spectrometry: a practical guide*. (Academic Press, 2011).

24. Parlak, O., Keene, S. T., Marais, A., Curto, V. F. & Salleo, A. Molecularly selective nanoporous membrane-based wearable organic electrochemical device for noninvasive cortisol sensing. *Science Advances* **4**, eaar2904 (2018).

25. Kaspar, H., Dettmer, K., Gronwald, W. & Oefner, P. J. Automated GC–MS analysis of free amino acids in biological fluids. *Journal of Chromatography B* **870**, 222–232 (2008).

Appendix B

SUPPLEMENTARY INFORMATION FOR CHAPTER 3

Materials from this chapter appears in "Wang, M.; Yang, Y.; Min, J.; Song, Y.; Tu, J.; Mukasa, D.; Ye, C.; Xu, C.; Heflin, N.; McCune, J. S.; Hsiai, T. K.; Li, Z.; Gao, W. A wearable electrochemical biosensor for the monitoring of metabolites and nutrients. *Nature Biomedical Engineering* 1–11 (2022) doi: 10.1038/s41551-022-00916-z".

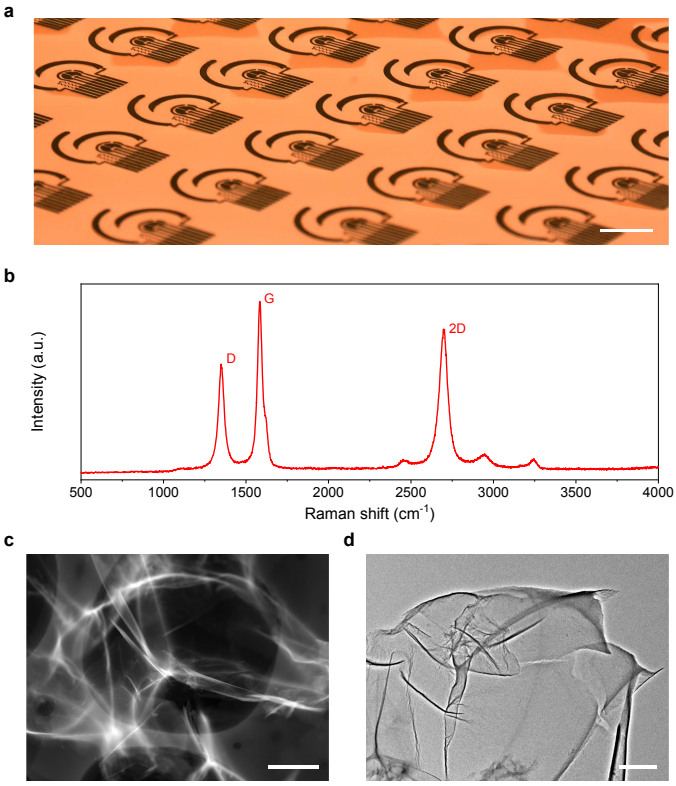

Figure B-1. Characterization of the LEG. a, Optical image of a flexible LEG sensor patch array fabricated via low-cost and mass-producible CO2 laser engraving. Scale bar, 1 cm. b, Raman spectra of the LEG. c,d, High-angle annular dark-field scanning transmission electron microscopy (HAADF-STEM) (c) and bright-field transmission electron microscopy (TEM) image (d) of the LEG. Scale bars, 1 μm and 500 nm, respectively.

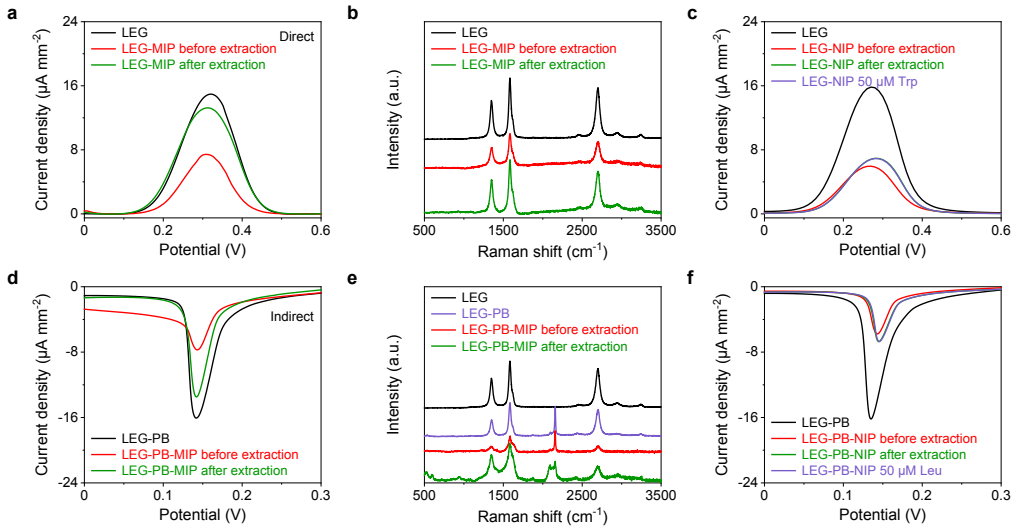

Figure B-2. Characterization and validation of the MIP sensor preparation. a, DPV voltammograms of the LEG, the LEG-MIP before template (Trp) extraction, and the LEG-MIP after template (Trp) extraction in 0.1 M KCl solution containing 2.0 mM $K_4Fe(CN)_6/K_3Fe(CN)_6$ (1:1). **b**, Raman spectra of the LEG, the LEG-MIP before template (Trp) extraction, and the LEG-MIP after template (Trp) extraction. **c**, DPV voltammograms of the LEG, the LEG-non-imprinted polymer (NIP), the LEG-NIP after template extraction procedure, and the LEG-NIP after extraction procedure (followed by a 7-min incubation in 50 μM Trp) in 0.1 M KCl solution containing 2.0 mM $K_4Fe(CN)_6/K_3Fe(CN)_6$ (1:1). **d**, LSV voltammograms of the LEG, the LEG-PB-MIP before template (Leu) extraction, and the LEG-PB-MIP after template (Leu) extraction in 0.1 M KCl. **e**, Raman spectra of the LEG, the LEG-PB, the LEG-PB-MIP before template (Leu) extraction, and the LEG-PB-MIP after template (Leu) extraction. **f**, LSV voltammograms of the LEG, the LEG-PB-NIP, the LEG-PB-NIP after template extraction procedure, and the LEG-PB-NIP after template extraction procedure (followed by a 7-min incubation in 50 μM Leu) in 0.1 M KCl.

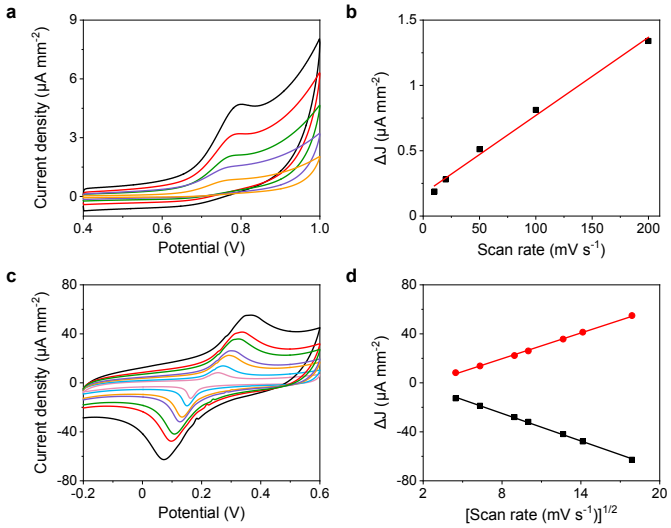

Figure B-3. Characterization of the electrochemical kinetics of the LEG-MIP electrodes. a,**b**, Cyclic voltammograms (**a**) of an LEG-MIP Trp sensor at the scan rates from 10 to 200 mV s^{-1} in 50 μM Trp, and the corresponding plot (**b**) of anodic peak current densities versus scan rate. **c**,**d**, Cyclic voltammograms (**c**) of an LEG-PB-MIP Leu sensor in 0.1 M KCl at the scan rates from 10 to 300 mV s^{-1} and the corresponding plot (**d**) of anodic and cathodic peak current densities versus square-root of scan rate. Solid lines in **b**,**d** represent linear fit trendlines.

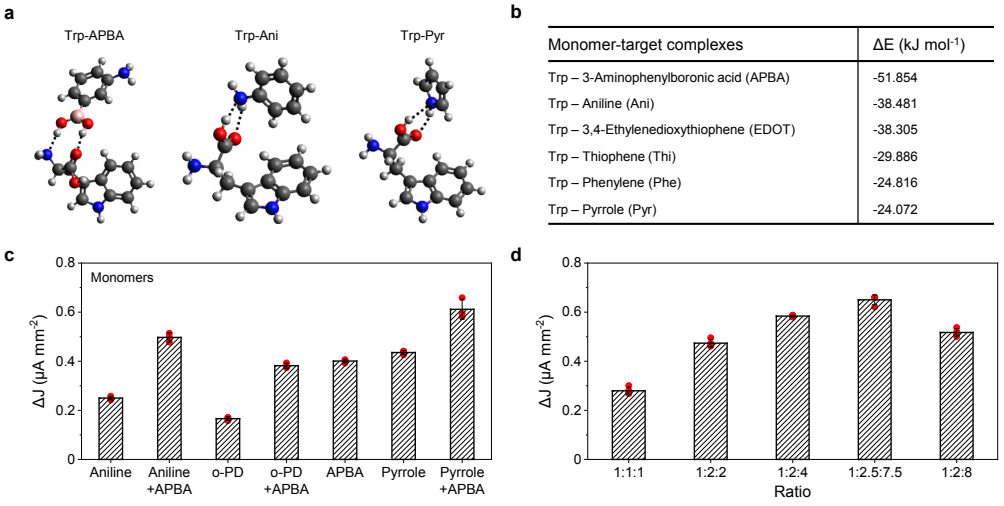

Monomer-target complexes	ΔE (kJ mol^{-1})
Trp – 3-Aminophenylboronic acid (APBA)	-51.854
Trp – Aniline (Ani)	-38.481
Trp – 3,4-Ethylenedioxythiophene (EDOT)	-38.305
Trp – Thiophene (Thi)	-29.886
Trp – Phenylene (Phe)	-24.816
Trp – Pyrrole (Pyr)	-24.072

Figure B-4. Theoretical and experimental optimization of the MIP composition. **a**, Density functional theory (DFT)-optimized geometries of the monomer

(Pyr)/target (Trp) bonding. **b**, DFT simulated bonding energies of the monomer-target complexes. **c**,**d**, Current density of the peak height (ΔJ) of the Trp MIP sensors based on different monomer/target combinations (**c**) and different target/crosslinker/monomer ratios (**d**) in 50 μM Trp. Ratios of target/(crosslinker)/monomer in **c**, 1:(2.5):7.5; APBA was used as the crosslinker for **c** and **d**. Error bars represent the s.d. from 3 sensors.

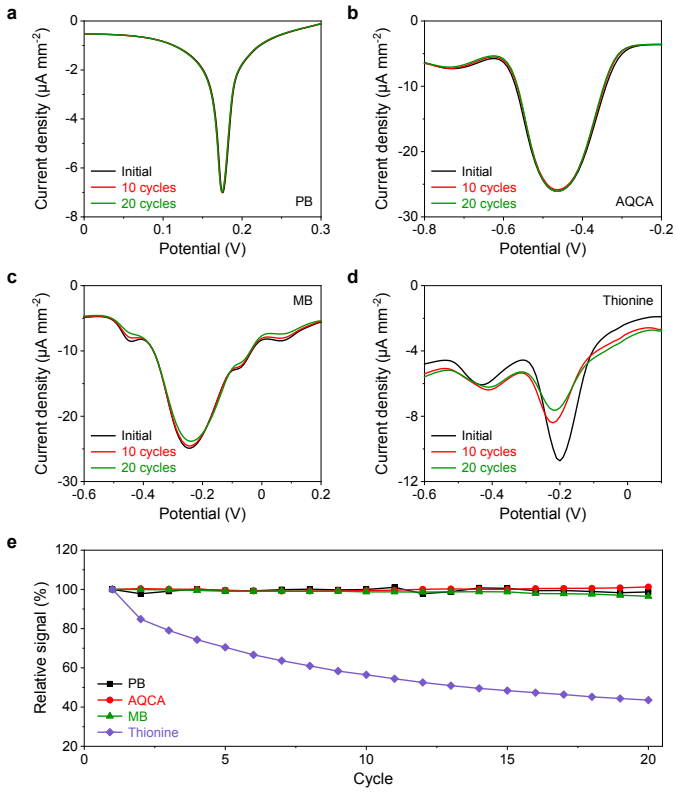

Figure B-5. Electrochemical characterization of the RARs on the LEG. a, Repetitive LSVs of the PB modified LEG electrodes. **b**–**d**, Repetitive negative DPVs of the AQCA (**b**), MB (**c**), and thionine (**d**) modified LEG electrodes. **e**, Relative peak signal changes of PB, AQCA, MB, and thionine RAR-modified LEG electrode under repeating voltammetric scans. DPV conditions for **b**–**e**: scan range, -0.2–-0.8 V, 0.2–-0.6 V and 0.1–-0.6 V, respectively, for AQCA, MB, and Thionine; scan rate, 5 mV s^{-1}; sample interval, 1 mV; quiet time, 2 s; sensitivity, 1×10^{-4} A V^{-1}.

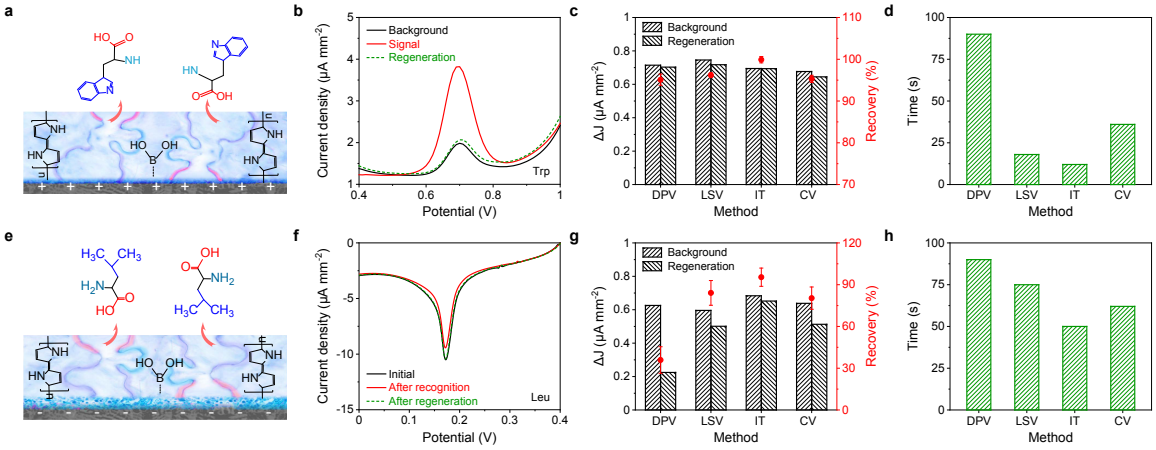

Figure B-6. Characterizations of the LEG-MIP sensor regeneration. a, Schematic of the LEG-MIP sensor regeneration for direct electroactive molecule detection. **b**, DPV voltammograms of an LEG-MIP Trp sensor before and after regeneration in 50 μM Trp (IT under a fixed potential of 0.7 V for 12 s). **c**, Comparison of regeneration efficiency of the LEG-MIP Trp sensors using controlled voltammetry (i.e., DPV, LSV, IT, CV) after 12 s. **d**, Time consumption of the LEG-MIP Trp sensors to reach 100 % recovery. **e**, Schematic of the LEG-PB-MIP sensor regeneration for indirect detection. **f**, LSV voltammograms of an LEG-PB-MIP Leu sensor before and after regeneration in 50 μM Leu (IT under a fixed potential of -0.2 V for 50 s). **g**, Comparison of regeneration efficiency of the LEG-PB-MIP Leu sensors using controlled voltammetry (i.e., DPV, LSV, IT, CV) after 50 s. **h**, Time consumption of the LEG-PB-MIP Leu sensors to reach 80% signal change recovery. Error bars in **c** and **g** represent the s.d. from 3 sensors.

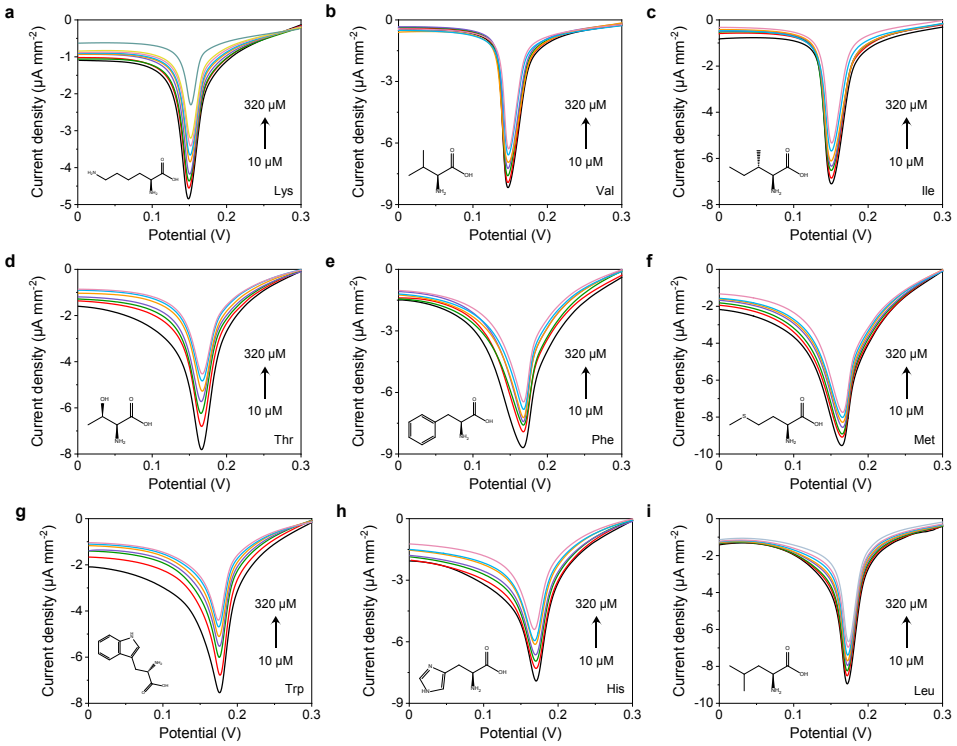

Figure B-7. LSV voltammograms of the LEG-PB-MIP sensors for indirect detection of all nine essential amino acids.

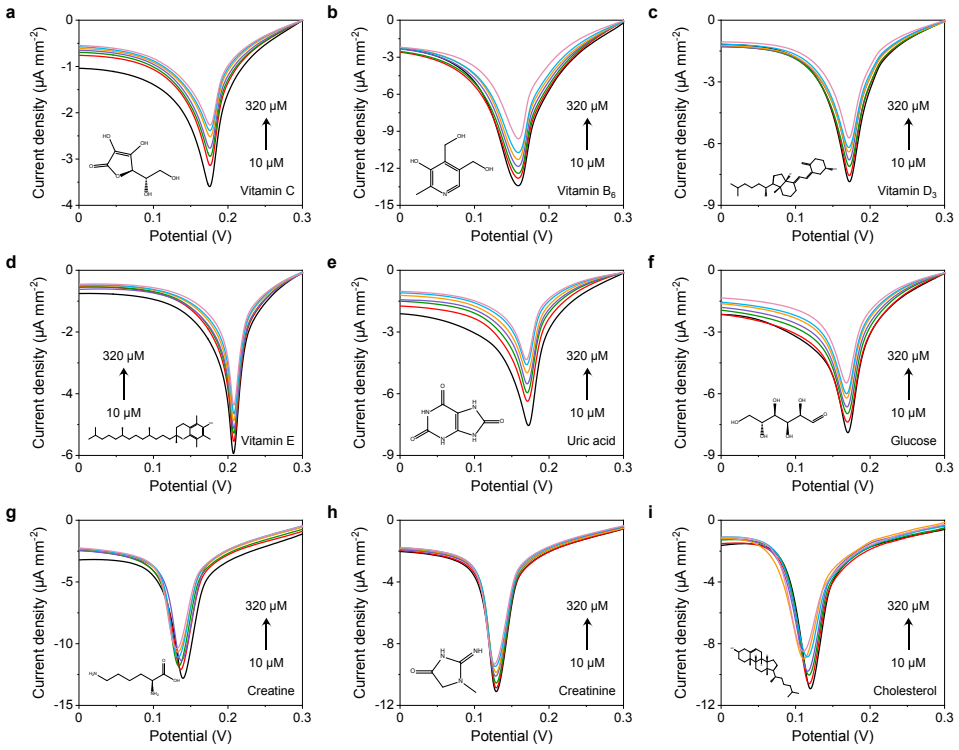

Figure B-8. LSV voltammograms of the LEG-PB-MIP sensors for indirect detection of multiple vitamins, metabolites, and lipids.

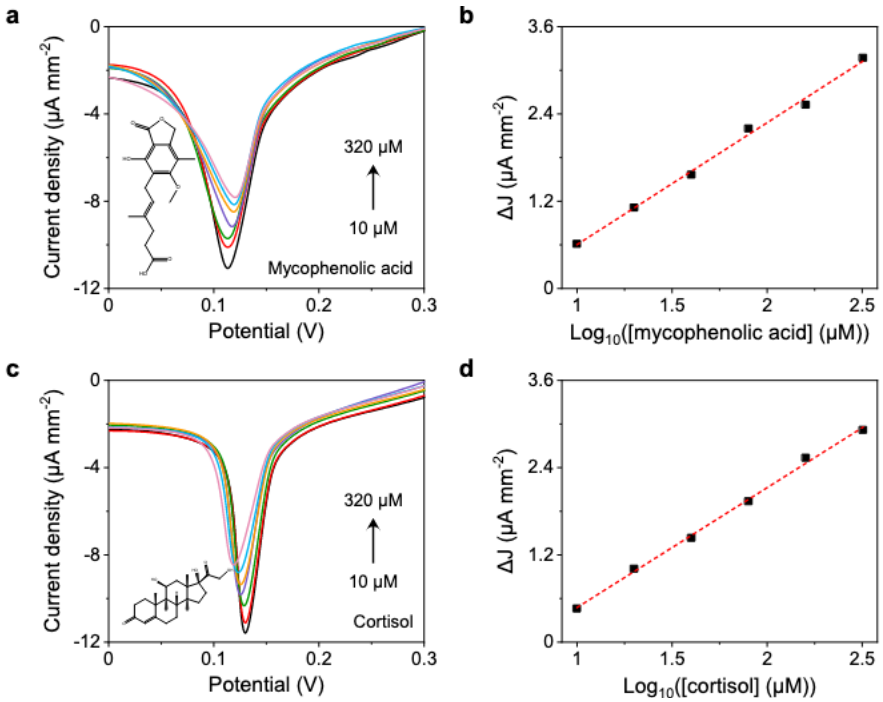

Figure B-9. LSV voltammograms and the corresponding calibration curves of the LEG-PB-MIP sensor for indirect detection of cortisol and mycophenolic acid. Dashed lines in b,d represent linear fit trendlines.

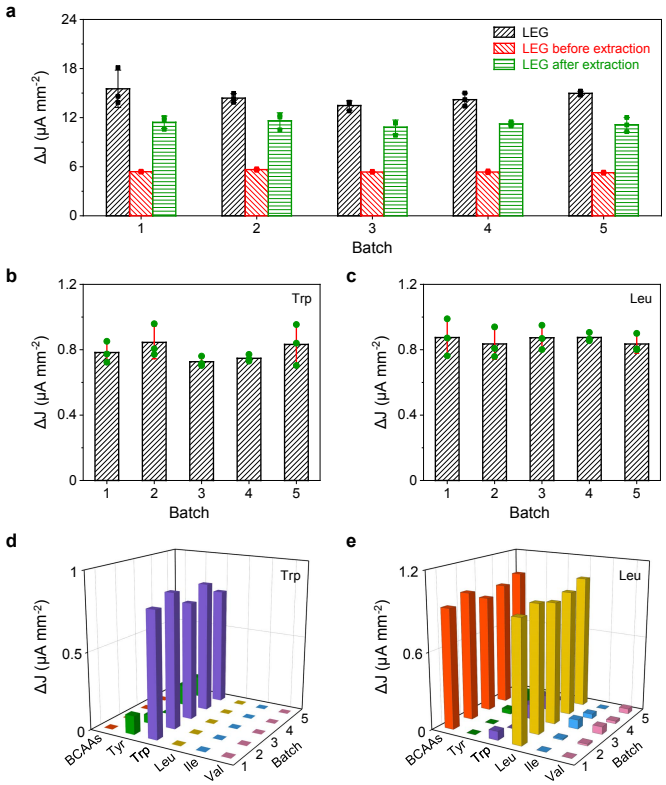

Figure B-10. Characterization of the reproducibility of the LEG-MIP sensors from five different batches. a, Device-to-device variations in MIP film preparation on LEG. ΔJ represents current density of the peak height in the voltammograms (DPV here) of the LEG, the LEG-MIP before template (Trp) extraction, and the LEG-MIP after template (Trp) extraction in 0.1 M KCl solution containing 2.0 mM K4 Fe(CN)6 /K3 Fe(CN)6 (1:1). Error bars represent the s.d. from 3 sensors. b,c, Sensitivity reproducibility of the LEG-MIP sensors. Batch-to-batch comparison of the sensitivity (ΔJ) of the Trp LEG-MIP sensors (b) and the Leu LEG-PB-MIP sensors (c) in the presence of 50 μM target. Error bars represent the s.d. from 3 sensors. d,e, Selectivity reproducibility of the LEG-MIP sensors. Batch-to-batch comparison of the selectivity of the Trp LEG-MIP sensors (d) and the Leu LEG-PB-MIP sensors (e) over other amino acids. 50 μM was used for each amino acid.

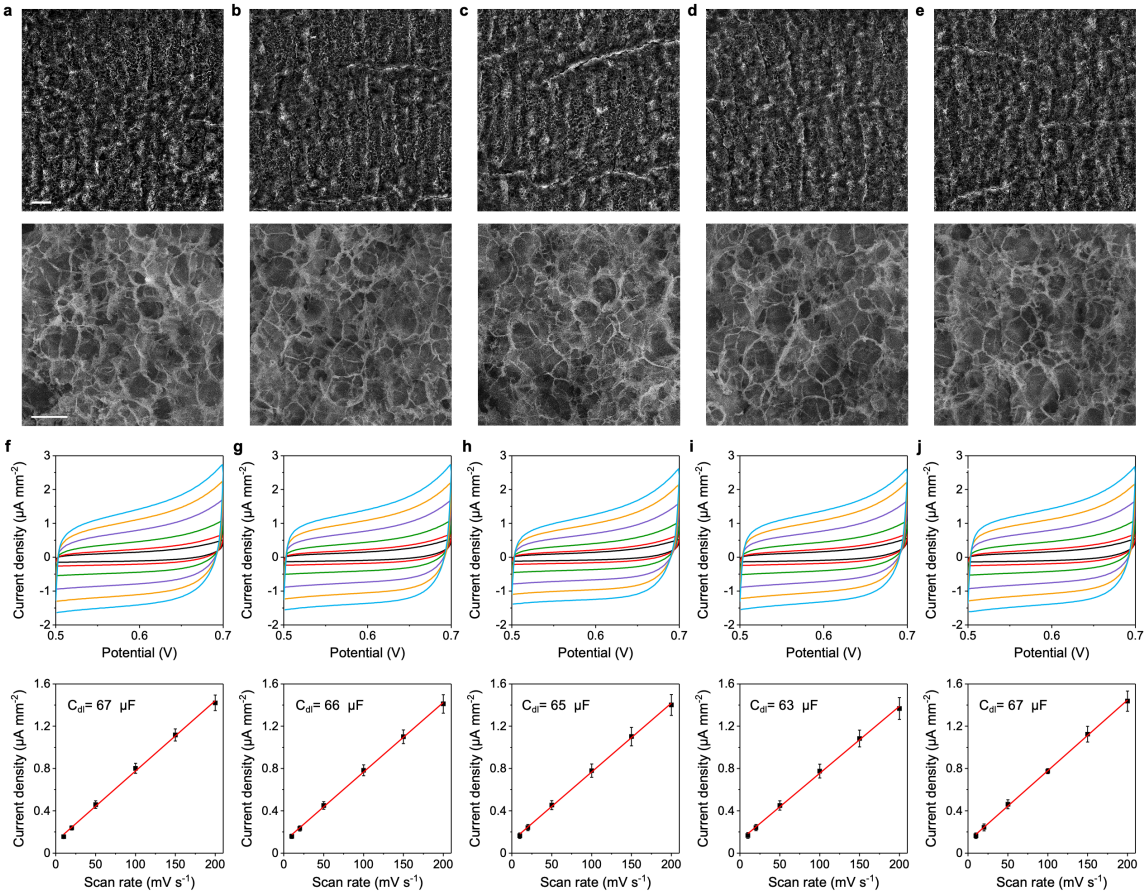

Figure B-11. Microscopic and electrochemical characterization of the surface of the LEG-MIP electrodes. a–e, SEM characterization of the surface of LEG-MIP Trp electrodes from 5 different batches. Scale bars, 100 μm and 10 μm for upper and lower rows, respectively. f–j, Electrochemical characterization of the surface of LEG-MIP Trp electrodes from 5 different batches. Cdl, electrochemical double layer capacitance. Cyclic voltammograms were obtained for each LEG-MIP Trp electrode at the scan rates in PBS (pH 6.5). Current density in the calibration plot represents the oxidation current height at 0.6 V. Error bars represent the s.d. from 3 sensors. Solid lines in calibration plots represent linear fit trendlines.

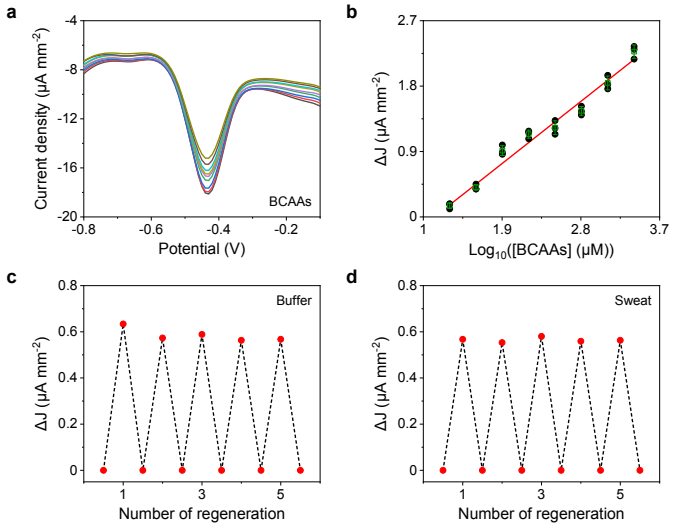

Figure B-12. Characterization of the performance of the LEG-AQCA-multi-MIP BCAA sensor. a,b, Negative DPV voltammograms (a) and the corresponding calibration plot (b) of an LEG-AQCA-multi-MIP sensor for BCAA quantification. Error bars represent the s.d. from 3 sensors. Solid line in b represent a linear fit trendline. c,d, In situ regeneration of an LEG-AQCA-MIP BCAAs sensor in PBS buffer containing 60 μM total BCAAs (1:1:1) (c) and a raw sweat sample collected from a healthy subject (d).

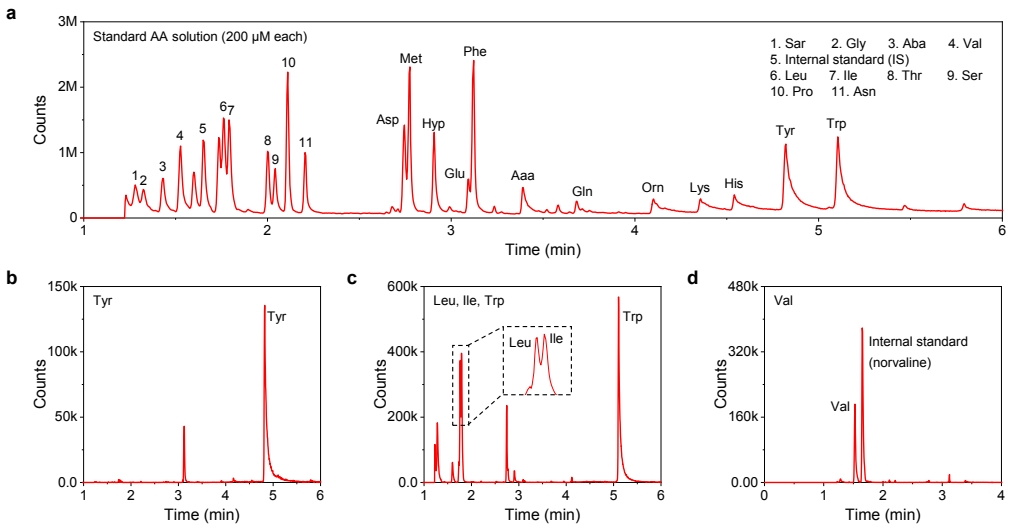

Figure B-13. GC-MS analyses of the Tyr, Try, Leu, Ile and Val in standard analyte solution. Each amino acid (200 μM added) displays a characteristic specific

peak at its specific ion number. a, Merged spectrum of all ion numbers displaying all amino acids detectable by the EZ:Faast amino acid kit. b, Characteristic peak of Tyr in Ion 164. c, Characteristic peak of Leu, Ile and Trp in Ion 130. d, Characteristic peak of Val in Ion 158

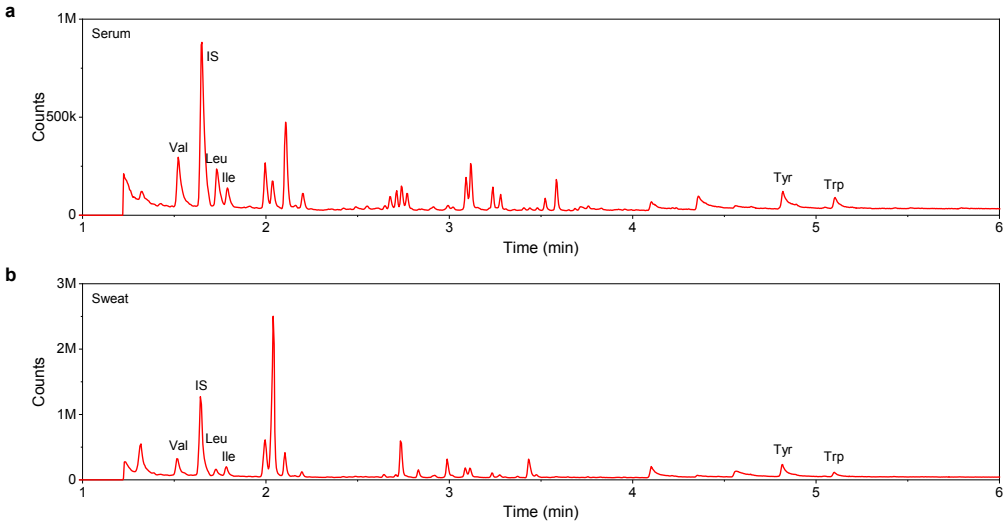

Figure B-14. GC-MS analyses of human sweat and serum samples collected at the same time. Serum and sweat samples are diluted for 4 and 6.66 times, respectively. Merged spectra of all ion numbers are shown here. Compared to sweat, merged spectra of all ion numbers in serum displayed more peaks showing more amino acids.

Table B-1. Sweat analytes and their concentrations used for the selectivity studies. The values were chosen based on the mean physiological levels of the analytes[1]

Number	Constituents	Concentration (μM)	Number	Constituents	Concentration (μM)
1	Alanine	360	20	Ornithine	150
2	Arginine	780	21	Pantothetic acid	50
3	Ascorbic acid	10	22	Phenylalanine	130
4	Aspartic acid	340	23	Pyridoxine	0.01
5	Choline chloride	50	24	Riboflavin	50
6	Citrulline	400	25	Serine	50
7	Creatine	15	26	Thiamine	50
8	Creatinine	84	27	Threonine	450
9	Dehydroascorbic acid	11	28	Tryptophan	55
10	Folic acid	50	29	Tyrosine	170
11	Glutamic acid	370	30	Uric acid	50
12	Glycine	390	31	Valine	250
13	Histidine	520	32	Vitamin B6	20
14	Inositol	1.6	33	Vitamin C	20
15	Isoleucine	16	34	Vitamin D3	20
16	Leucine	210	35	Vitamin E	20
17	Lysine	150	36	Glucose	40
18	Methionine	50	37	Lactate	2000
19	Nicotinic acid	50			

Table B-2. The sensitivities (normalized by electrode area) of the LEG-PB-MIP sensors for
small molecule quantification.

Number	Targets	Sensitivity (nA mm^{-2} decade $(\mu M)^{-1}$)	Number	Targets	Sensitivity (nA mm^{-2} decade $(\mu M)^{-1}$)
1	Lysine	596.2	11	Vitamin B_6	748.3
2	Valine	1134.9	12	Vitamin E	748.3
3	Leucine	701.6	13	Vitamin D_3	1416.9
4	Methionine	753.8	14	Uric acid	1197.4
5	Phenylalanine	788.3	15	Glucose	1005.7
6	Threonine	1330.7	16	Creatine	974.2
7	Histidine	1014.4	17	Creatinine	936.1
8	Tryptophan	1407.9	18	Cholesterol	1188.3
9	Isoleucine	860.2	19	Mycophenolic acid	1676.7
10	Vitamin C	552.9	20	Cortisol	1648.2

Note B-1. Optimization and characterization of the LEG-MIP biosensors Characterization of the MIP sensor preparation. *The preparation of the LEG-MIP sensors was characterized electrochemically with differential pulse voltammetry (DPV) in 0.1 M KCl solution containing 2.0 mM $K_4Fe(CN)_6/K_3Fe(CN)_6$ (1:1) (Appendix B, Fig. B-2a). The LEG displayed a high oxidation peak owing to its large electrochemically active surface area. The redox peak substantially decreased after the MIP film deposition (co-polymerization of APBA and pyrrole in the presence of Trp here) due to the fact that the less conducting polymer layer blocked the LEG from the redox reporter solution. The template molecules were removed during template extraction step, leaving behind imprinted cavities that are complementary, both chemically and sterically to the template molecules. These cavities allow reporter ions to reach the electrolyte/electrode interface, resulting in a rise of the redox peak current.*

Raman spectrum was also used to study the surface roughness of the LEG-MIP sensor during preparation process. Raman intensity is influenced by the scattering of the exciting light from the sample surface, and thus decreases with the increase of surface roughness. As shown in **Appendix B, Fig. B-2b**, Raman intensity of C=C backbone stretching increased after polymerization (smooth surface), and then decreased after template extraction (rough surface), indicating the residual cavities on the surface resulted from the template extraction[1]. To further validate the successful preparation of the MIP layer, a non-imprinted polymer (NIP) film was prepared on the LEG as the control. The standard MIP template extraction procedure and further incubation in 50 μM Trp did not lead to substantial signal change of the LEG-NIP in the standard redox solution (**Appendix B, Fig. B-2c**).

For the preparation of the LEG-RAR-MIP sensors, redox reporters such as Prussian blue (PB) and anthraquinone-2-carboxylic acid (AQCA) were deposited between the MIP and graphene layers. For the PB RAR, the preparation process was characterized electrochemically with linear sweep voltammetry (LSV) in 0.1 M KCl as illustrated in **Appendix B, Fig. B-2d**. The LEG-PB displayed a high

reduction peak of PB which decreased after deposition of the polymer film (co-polymerization of APBA and pyrrole in the presence of Leu here) due to the PB blockage by the polymer. The extraction of the template molecules (with CV sweeping in 0.1 M HCl and 0.1 M KCl) leads to the target selective cavities and increases the exposure of the PB film to the electrolyte solution, resulting an increased redox signal.

The Raman spectra of the LEG-PB-MIP Leu showed similar behavior as the LEG-MIP Trp sensor: Raman intensity of C=C backbone stretching increased after polymerization on LEG-PB, and then decreased after template extraction, the residual cavities were left on the surface resulted from the template extraction (**Appendix B, Fig. B-2e**). To further validate the successful preparation of the MIP layer on the LEG-PB, a NIP film was prepared on the LEG-PB as the control. The standard MIP template extraction procedure and further incubation in 50 μM Leu did not lead to substantial signal change of the LEG-PB-NIP (**Appendix B, Fig. B-2f**).

Electrochemical kinetics of the LEG-MIP electrodes. The electrochemical kinetic process on the modified electrode plays an important role in understanding whether the reaction process at the modified electrode is controlled by adsorption and/or diffusion. Cyclic voltammetry (CV) was used to study the effect of scan rate on the peak current for both the direct and indirect detection LEG-MIP sensors (**Appendix B, Fig. B-3**). Since the electroactive target (e.g., Trp) can be directly oxidized at a given voltage, the LEG-MIP Trp sensor was evaluated in 0.01 M PBS containing 50 μM Trp (**Appendix B, Fig. B-3a,b**). A linear dependence was obtained between the anodic peak current and scan rate, indicating that the oxidation of Trp on the direct detection MIP sensor is controlled by adsorption processes. On the other side, the redox peak of the RAR (e.g., PB) can be directly used to study the electrode kinetics in 0.1 M KCl (**Appendix B, Fig. B-3c,d**). In this case, both anodic and cathodic peak currents showed proportional relationships to square root of the scan rate, suggesting that electrochemical redox reactions at

LEG-PB-MIP Leu sensor were a diffusion-controlled process[2]. The relation between measured peak height current density J_{pa} (μA mm^{-2}) and scan rate v (mV s^{-1}) for direct and indirect detection MIP sensors are as follows:

LEG-MIP Trp sensors:

$J_{pa} = 0.1718 + 0.006v$

LEG-PB MIP Leu sensors:

$J_{pa,\ anodic} = -8.338 + 3.5031\sqrt{v}$

$J_{pa,\ cathodic} = 5.007 - 3.7458\sqrt{v}$

The above results explain the reasons why the current signal has a linear relationship with the concentration of the target in direct detection, while it is log-linear with the target levels in indirect detection. To minimize the influence of oxidation reactions of common sweat interferants, the reduction peak of PB is chosen for further analyzing of in direct detection.

Theoretical and experimental optimization of MIP composition. MIPs can either rely on covalent or non-covalent interactions. In the case of a wearable sensor which should be capable of regeneration for continuous monitoring, weak reversible non-covalent interactions are ideal. There are multiple of monomers which are capable of forming non-covalent bonds with amino acids (e.g., Trp and Leu), however we narrowed our search to electroactive monomers since sensor fabrication with such monomers requires only electropolymerization on the working electrode in the presence of the desired template molecules. In addition, electroactive monomers efficiently transduce binding events, thus improving detectability[3]. Thus, the formulations such as choices of monomers and monomer/template ratios have substantial influence on the sensitivity and the selectivity of the MIP sensor.

Taking the Trp sensor design as an example, we utilized density functional theory (DFT) calculations to quantify the binding energy between Trp and six commonly

used electroactive monomers: aminophenylboronic acid (APBA), aniline, ethylenedioxythiophene (EDOT), phenylene, pyrrole, and thiophene (**Appendix B, Fig. B-4**). The calculations were carried out using the ORCA software[4]. The semiempirical Austin Model 1 (AM1) was used first to achieve a rough estimate of geometric optimal configurations. The higher level B3LPY functional with a 6-31(d,p) basis set was then used to calculate final geometric configurations and binding energies. Binding energies were calculated with the typical formula:

$$\Delta E = E_{Monomer\text{-}Template} - (E_{Template} + E_{Monomer})$$

The DFT simulated bonding energies of the monomer-target complexes were demonstrated in **Appendix B, Fig. B-4b**. To maximize sensitivity of the MIP it is common to select the monomer which has the highest binding affinity to Trp. Further, it has been previously demonstrated that the co-polymerization of a monomer with high affinity and a monomer with low affinity (crosslinker) to the template can produce highly selective MIPs by mitigating non-selective binding[5]. APBA exhibits the highest interaction energy with the Trp, indicating that APBA is an ideal crosslinker or co-monomer for Trp MIP. The choice of pyrrole (which has lowest interaction energy) and APBA as the monomer and crosslinker could leads to MIPs with both high selectivity and high regeneration capability.

Our experimental data demonstrates that the choice of APBA/aniline also leads to high sensitivity (reflected by the current peak height of the LEG-MIP sensor in 50 μM Trp) compared to other individual monomers and other monomer/crosslinker combinations (**Appendix B, Fig. B-4c**). The ratio of template, crosslinker, and monomer is another key parameter MIP quality. Based on the experimental data illustrated in **Appendix B, Fig. B-4d**, the ratio of 1:2.5:7.5 (template/crosslinker/monomer) led to the optimal sensitivity for Trp detection.

Optimization of the LEG-MIP recognition *in vitro.* To obtain the optimal sensor performance for rapid sample analysis, the influences of sample incubation time and volume were evaluated experimentally. As demonstrated in **Fig.3-6a,b**, the current density of the peak height of the LEG-MIP Trp sensors increases rapidly

with the increase of incubation time initially, and then gradually stabilizes after 5 min (with an optimal incubation time of 7 min), indicating the saturated adsorption for Trp. Unlike the incubation time, sample volumes (between 0.028–1.1 μL mm^{-2}) didn't show substantial influence on the sensor response as illustrated in **Fig. 3-6c,d**.

Characterization of the RARs for indirect MIP detection. The high demand for electrochemical stability of wearable sensors in practical applications poses high requirements for RARs. Therefore, the performance of four RARs including PB, AQCA, MB, and thionine before and after repetitive LSV or DPV scans was investigated (**Appendix B, Fig. B-5**). As summarized in **Appendix B, Fig. B-5e**, PB and AQCA displayed best stability among these four.

***In situ* regeneration of the LEG-MIP sensors.** Sensor regeneration is the major hurdle that limits the applicability of current bioaffinity sensing technologies for wearable continuous monitoring. We have investigated the possibility of using various controlled voltammetric techniques to realize the repeatable, wash-free, *in situ* regeneration of the LEG-MIP sensors.

For direct detection of the electroactive targets (e.g., Trp) using LEG-MIP sensors, as the molecule is specifically fixed in the receptor site, the molecule can be oxidized once a proper redox voltage is applied to the electrode; the oxidation product doesn't have good binding affinity to the MIP receptor site, leading to sensor regeneration (**Appendix B, Fig. B-6a**). After the detection DPV scan, applying a fixed redox potential of 0.7 V for 12 s can reset the sensor response to the background current with a ~100% recovery ratio (**Appendix B, Fig. B-6b**). Considering that high temporal resolution (regeneration speed) and high accuracy (recovery ratio) are both critical for continuous wearable sensing, we evaluated various electrochemical voltammetric methods such as DPV, LSV, IT and CV for the LEG-MIP sensor regeneration (**Appendix B, Fig. B-6c,d**): the results show that IT offers the best performance in recovery rate.

The regeneration for the LEG-RAR-MIP sensors for detection of general targets, particularly non-electroactive targets such as BCAAs, is based on a different mechanism. After the extraction of the AA template from the MIP layer, the complementary cavity of corresponding AA exists within a polymer backbone or scaffold[6]. The negatively charged target AA will be specifically adsorbed into the shape imprinted cavity. A negative electrical signal applied on the working electrode will repel the negatively charged AA from the receptor site (**Appendix B, Fig. B-6e**). The LSV curve shows that the sensor can be restored to the same level as background signal under an applied negative voltage (-0.2 V) (**Appendix B, Fig. B-6f**). The regeneration method and the regenerate time was optimized by using various electrochemical voltammetric methods such as DPV, LSV, IT and CV. The results in **Appendix B, Fig. B-6g,h** show that IT method under the potential of -0.2V for 50 s is optimal for regeneration of the LEG-PB-MIP sensor.

Evaluation of the batch-to-batch sensor reliability and reproducibility. Traditional MIP was synthesized commonly using less controllable thermal or optical approaches in a bulk solution, which could have the limitations such as the production of irregular particles[7–9]. In this work, the MIP layer is electrochemically deposited on the surface of our mass-producible, highly consistent laser-engraved graphene (LEG) electrodes via cyclic voltammetry. The data in **Appendix B, Fig.B-10a** show that the electrochemical behaviors of our LEG electrodes, LEG-MIP electrodes before template (Trp) extraction, and the LEG-MIP electrodes after template (Trp) extraction show very small variation, indicating the high reproducibility and reliability of our MIP preparation process. To further verify the reliability of the LEG-MIP sensor, 5 different sensor batches (3 sensors per batch) were prepared to evaluate the reproducibility in sensitivity and selectivity for both electroactive (Trp) and non-electroactive (Leu) targets. As illustrated in **Appendix B, Fig.B-10b,c** the Trp and Leu LEG-MIP sensors from all batches exhibited very similar sensitivities with relative standard deviations of 5.16% and 2.14%, respectively (n=15) in the presence of the same concentration of target analytes. The Trp and Leu sensors obtained from all batches also showed high selectivity for

the target over other amino acids with similar structures (as shown in **Appendix B, Fig.B-10d,e**).

The characterization of the multi-MIP BCAA sensors. To ensure the multi-MIP BCAA sensors have same response to Leu, Ile, and Val, 5 mM of each target molecule was used to prepare the MIP film. Negative DPV from 0–-0.8 V was performed to characterize the LEG-AQCA-multi-MIP BCAA sensor in BCAA solutions (1:1:1), and a log-linear relationship between the peak height decrease and BCAA with sensitivity of 939.2 nA mm^{-2} per decade of concentration was observed (**Appendix B, Fig.B-12a,b**). The fabricated indirect LEG-AQCA-multi-MIP BCAA sensor can be regenerated *in situ* upon constant potential applied to the working electrode in both PBS buffer (**Appendix B, Fig.B-12c**) and raw sweat (**Appendix B, Fig.B-12d**).

Bibliography of Appendix B

1. Harvey, C. J., LeBouf, R. F. & Stefaniak, A. B. Formulation and stability of a novel artificial human sweat under conditions of storage and use. *Toxicology in Vitro* **24**, 1790–1796 (2010).
2. Liu, Y.-C., Hwang, B.-J., Jian, W.-J. & Santhanam, R. In situ cyclic voltammetry-surface-enhanced Raman spectroscopy: studies on the doping–undoping of polypyrrole film. *Thin Solid Films* **374**, 85–91 (2000).
3. Huang, B. *et al.* Electrochemical sensing platform based on molecularly imprinted polymer decorated N,S co-doped activated graphene for ultrasensitive and selective determination of cyclophosphamide. *Talanta* **164**, 601–607 (2017).

4. Sharma, P. S., Pietrzyk-Le, A., D'Souza, F. & Kutner, W. Electrochemically synthesized polymers in molecular imprinting for chemical sensing. *Analytical and Bioanalytical Chemistry* **402**, 3177–3204 (2012).
5. Software update: the ORCA program system, version 4.0 - Neese - 2018 - WIREs Computational Molecular Science - Wiley Online Library. https://wires.onlinelibrary.wiley.com/doi/abs/10.1002/wcms.1327.
6. Dechtrirat, D. *et al.* An electrochemical MIP sensor for selective detection of salbutamol based on a graphene/PEDOT:PSS modified screen printed carbon electrode. *RSC Advances* **8**, 206–212 (2018).
7. Liang, H.-J., Ling, T.-R., Rick, J. F. & Chou, T.-C. Molecularly imprinted electrochemical sensor able to enantroselectivly recognize d and l-tyrosine. *Analytica Chimica Acta* **542**, 83–89 (2005).
8. Poma, A., Turner, A. P. F. & Piletsky, S. A. Advances in the manufacture of MIP nanoparticles. *Trends in Biotechnology* **28**, 629–637 (2010).
9. BelBruno, J. J. Molecularly imprinted polymers. *Chemical Reviews* **119**, 94–119 (2019).
10. Haupt, K. & Mosbach, K. Molecularly imprinted polymers and their use in biomimetic sensors. *Chemical Reviews* **100**, 2495–2504 (2000).

C h a p t e r 4

LASER-ENGRAVED MICROFLUIDICS FOR SWEAT SAMPLING

Materials from this chapter appears in "Yang, Y.; Gao, W. Wearable and flexible electronics for continuous molecular monitoring. *Chemical Society Reviews* **48**, 1465–1491 (2019) doi: 10.1039/C7CS00730B", "Min, J.; Tu, J.; Xu, C.; Lukas, H.; Shin, S.; Yang, Y.; Solomon, S.; Mukasa, D.; Gao, W. Skin-interfaced wearable sweat sensors for precision medicine. *Chemical Reviews*, *Manuscript Submitted*","Yang, Y.; Song, Y.; Bo, X.; Min, J.; Pak, O. S.; Zhu, L.; Wang, M.; Tu, J.; Kogan, A.; Zhang, H.; Hsiai, T. K.; Li, Z.; Gao, W. A laser-engraved wearable sensor for sensitive detection of uric acid and tyrosine in sweat. *Nature Biotechnology* 38, 217–224 (2020) doi:10.1038/s41587-019-0321-x" and "Wang, M.; Yang, Y.; Min, J.; Song, Y.; Tu, J.; Mukasa, D.; Ye, C.; Xu, C.; Heflin, N.; McCune, J. S.; Hsiai, T. K.; Li, Z.; Gao, W. A wearable electrochemical biosensor for the monitoring of metabolites and nutrients. *Nature Biomedical Engineering* 1–11 (2022) doi: 10.1038/s41551-022-00916-z".

4.1 Introduction

The fast progress in sweat sensing platforms has expedited research on sweat sampling. The continuity and reliability of sweat sensor data are fundamental for achieving continuous health monitoring. Effective sweat sampling is the first step toward achieving continuous and accurate biomarker analysis. Early sweat sampling methods for analyzing biomarkers in sweat were often confounded by discrepancies due to skin contamination, sweat evaporation, sweat stimulation methods, and sweat rate effects.[1–4] Recent development in sweat sampling microfluidics offers a great solution to tackle these challenges, but most devices were based on PDMS technology requiring cleanroom fabrication, which could be costly and time-consuming.[5,6] In Chapter 4.2, we will summarize our efforts done to achieve scalable fabrication of sweat-sampling microfluidics via laser engraving.

On the other hand, sweat can be induced in various manners, such as thermal stimulation, exercise, natural secretion, and iontophoresis. While past sweat studies rely heavily on exercise and thermal stress, large variations in sweat rate could be expected and hampered the collection on sedentary individuals.[2,3,7,8] Iontophoresis was developed to achieve sweat stimulation in sedentary individuals. Iontophoresis is a procedure where a small current delivers a cholinergic drug loaded in hydrogel into the skin. Two pieces of hydrogels are attached to the skin; the anode hydrogel contains a cholinergic agent while the cathode hydrogel contains electrolytes to facilitate current flow (**Fig. 4-1**). As the cholinergic agent stimulates the M3 muscarinic receptors on sweat glands, a direct sweat response is elicited. Depending on nicotinic receptor specificity, the iontophoretic drug may induce peripheral sudomotor axon reflex sweating.[9] Different cholinergic agonists could be used to induce sweating and the sweating response varies in duration and area, determined by the receptor activity and susceptibility to acetylcholinesterase (AChE) hydrolysis. Although a few recent reports use pilocarpine gel-based iontophoresis for sedentary sweat sampling,[10–12] this approach suffers from short sweat periods and low sensing accuracy due to the mixing of sweat and gel fluid and the lack of

dynamic sweat sampling. In the Chapter 4.3, we will elaborate our laser-engraved microfluidics for on-demand sweat stimulation and continuous sweat sampling.

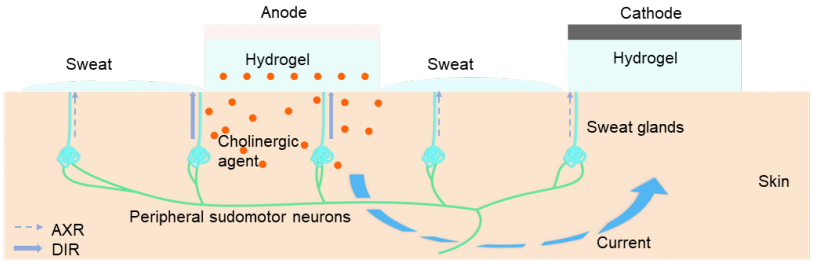

Figure 4-1. Scheme of iontophoresis-based sweat induction. AXR: Axon-reflex mediated sweating. DIR: direct stimulated sweating.

4.2 Laser-engraved Microfluidics for Exercise-induced Sweat

4.2.1 Materials and Methodology

Materials

Medical adhesives were purchased from Adhesives Research. Polyimide film (75 µm thick) and PET (12 µm and 75 µm thick) were purchased from DuPont and McMASTER-CARR, respectively.

Fabrication and characterization of microfluidic channels

A double-sided medical adhesive was attached to a substrate in the above-mentioned laser cutter. One layer of medical adhesive was cut through to make the channels and the reservoir, and another layer of medical adhesive was used to interface skin with inlets. The cylindrical reservoir has a radius of 2.13 mm, a thickness of 140 µm (medical tape) and its volume can thus be calculated as ~2 µl. The microfluidic channels have a depth of 140 µm and a width of 175 µm. Between two layers lies a thin (12 µm) and transparent PET film. The optimized laser cutter parameters were power 1%, speed 1.5%, PPI 1,000 for reservoir outline and channels, and power 2%, speed 1%, PPI 1,000 for inlet outlines, all in vector mode. The sweat rates were measured via optical image analysis on the basis of the photographs of a microfluidic patch taken sequentially on the different body parts

of the subjects. The estimated sweat rates were calculated by the sweat volume changes divided by the time intervals. For **Fig. 4-3f**, black dye was dropped in the reservoir, and a transparent 75-μm PET film was used instead of the polyimide layer to prepare the microfluidics for better visibility. An assembled flow patch was attached onto a subject's arm after an iontophoresis session implemented using a Model 3700 Macroduct Sweat Collection System. The flow tests were done with a syringe pump (Thermo Fisher Scientific, 78-01001) and set concentrations of UA and Tyr in ABS. The DPV data were wirelessly transmitted to a laptop computer and automatically converted to concentration via custom-developed software.

Refreshing time analysis and simulations

A ballpark estimate of the concentration refreshing time T_c can be obtained by considering the mass balance of a standard well-mixed model: $dC/dt+(C-C_i)Q/V_r=0$, where C_i and Q denote, respectively, the new solute concentration and total flow rate into the reservoir, and V_r represents the reservoir volume. This simple ordinary differential equation can be solved analytically to obtain the solute concentration in the reservoir as a function of time t: $C(t)=C_i-(C_i-C_0)e^{-Qt/V_r}$, where C_0 is the initial concentration in the reservoir. Hence, the refreshing time taken for the reservoir to reach a concentration of kC_i can be readily calculated as $T_c=\frac{V_r}{Q}ln\frac{1-C_0/C_i}{1-k}$. For an experimentally measured sweat rate of Q = 1.5 μL min^{-1} and concentration change from C_0 = 20 μM to C_i = 80 μM, we estimate that the designed reservoir volume V_r = 2 mm^3 leads to a refreshing time $T_c \approx$ 2.7 minutes to reach k = 90% of the new concentration. This simple analysis provides an order of magnitude estimate of the required refreshing time by assuming perfect mixing. To obtain more realistic estimates, a three-dimensional model was created with the same geometry of the device. The mass transport process was simulated using a finite-element software COMSOL Multiphysics by numerically solving the Stokes equation for an incompressible flow

$$\nabla p = \mu \nabla^2 \boldsymbol{v}, \nabla \cdot \boldsymbol{v} = 0,$$

coupled with the convection-diffusion equation

$$\frac{\partial C}{\partial t} + \boldsymbol{v} \cdot \nabla C = D \nabla^2 C.$$

Here p and $\boldsymbol{v}$ denote, respectively, pressure and flow velocity, whereas μ and D denote, respectively, solvent viscosity and solute diffusivity. The Stokes equation is applicable here because the Reynolds number is on the order of 10^{-2} for this microfluidic device. The solute concentration in the chamber is tracked by computing the average concentration over the bottom surface of the chamber. A flow rate of 0.15 μL min^{-1} is prescribed at each inlet, with the no-slip boundary condition on all channel walls.

The simulated refreshing time as a function of the number of inlets is displayed in Fig. 3c. The refreshing time decreases as the number of inlets increases; for ten inlets with a total inlet flow rate of 1.5 μl min^{-1}, the simulated 90% refreshing time is ~2.5 min, slightly less than the ballpark estimate on the basis of perfect mixing (~2.7 min). In **Fig. 4-3d**, the time evolution of the average concentration under different total inlet flow rates is displayed. In Fig. 3c, the concentration distribution over the bottom surface of the chamber is displayed at different time instances. Similarly, numerical simulation was performed on the basis of the actual design of the microfluidic module used in this work (**Appendix C, Fig. C-3**).

4.2.2 Results and Discussion

The microfluidic module consists of multiple layers engraved by the laser cutter: microfluidic channels patterned on a double-sided medical adhesive and inlet-engraved polyethylene terephthalate (PET) and medical adhesive layers (**Fig. 4-2** and **Appendix C, Fig. C-1,2**).

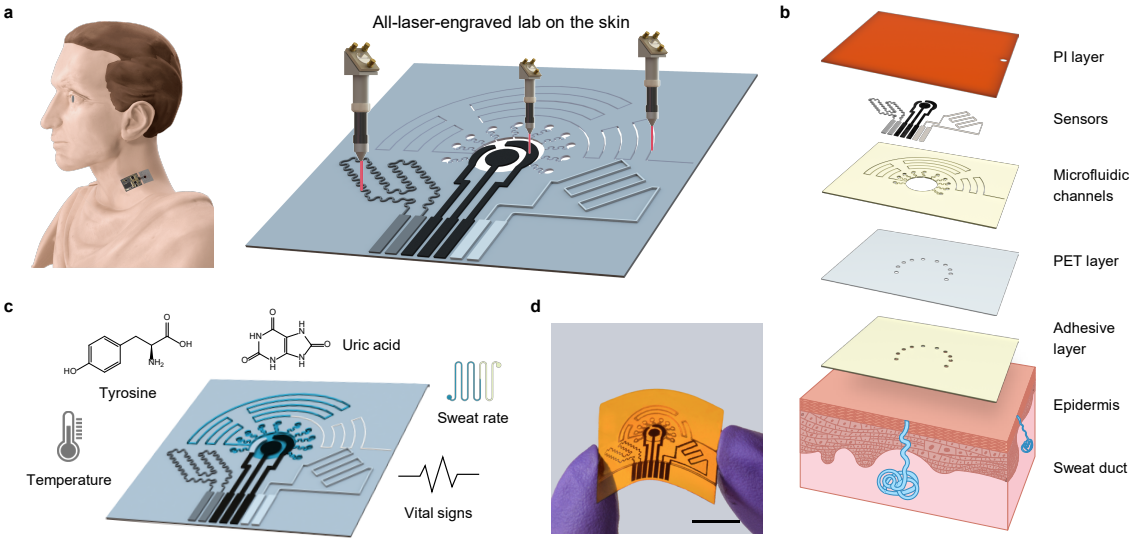

Figure 4-2. Schematics and photo of the microfluidic sweat sensing patch. **a**, The sensor with entirely laser-engraved components: the microfluidic module and the LEG-based chemical and physical sensors. **b**, Layers of the sensor, from the bottom layer in contact with epidermis to the top layer. **c**, Multiple functions of the microfluidic sensor: ultrasensitive sweat UA and Tyr detection, sweat rate estimation, temperature sensing and vital-sign (for example, heart rate and respiration rate) monitoring. **d**, Photographic image of a flexible microfluidic patch.

Design and performance characterization of the laser-engraved microfluidics

Laser engraving enables rapid bulk manufacturing of microfluidic devices. The microfluidic module is fabricated in vector mode to fully cut through double-sided adhesives (**Fig. 4-3a,b**). The use of microfluidics enhanced the sweat sampling process and achieved higher temporal resolution for wearable sensing by constantly supplying newly secreted sweat to the sensor. In response to inflow of solutions at a new solute concentration, the time taken for the solute concentration in the reservoir to adjust to the new concentration (referred to as the refreshing time hereafter) is a key performance indicator of the microfluidic module. We used numerical simulations to determine the effects of the inlet number and flow rates on the refreshing time (**Fig. 4-3c,d**). For the case of ten inlets, with an experimentally measured sweat rate ($1.5\ \mu l\ min^{-1}$) as the inlet flow rate, the

refreshing time taken to reach 90% of the new solute concentration was around 2.5 min, for a change of solute concentration from 20 μM to 80 μM (**Fig. 4-3e**).

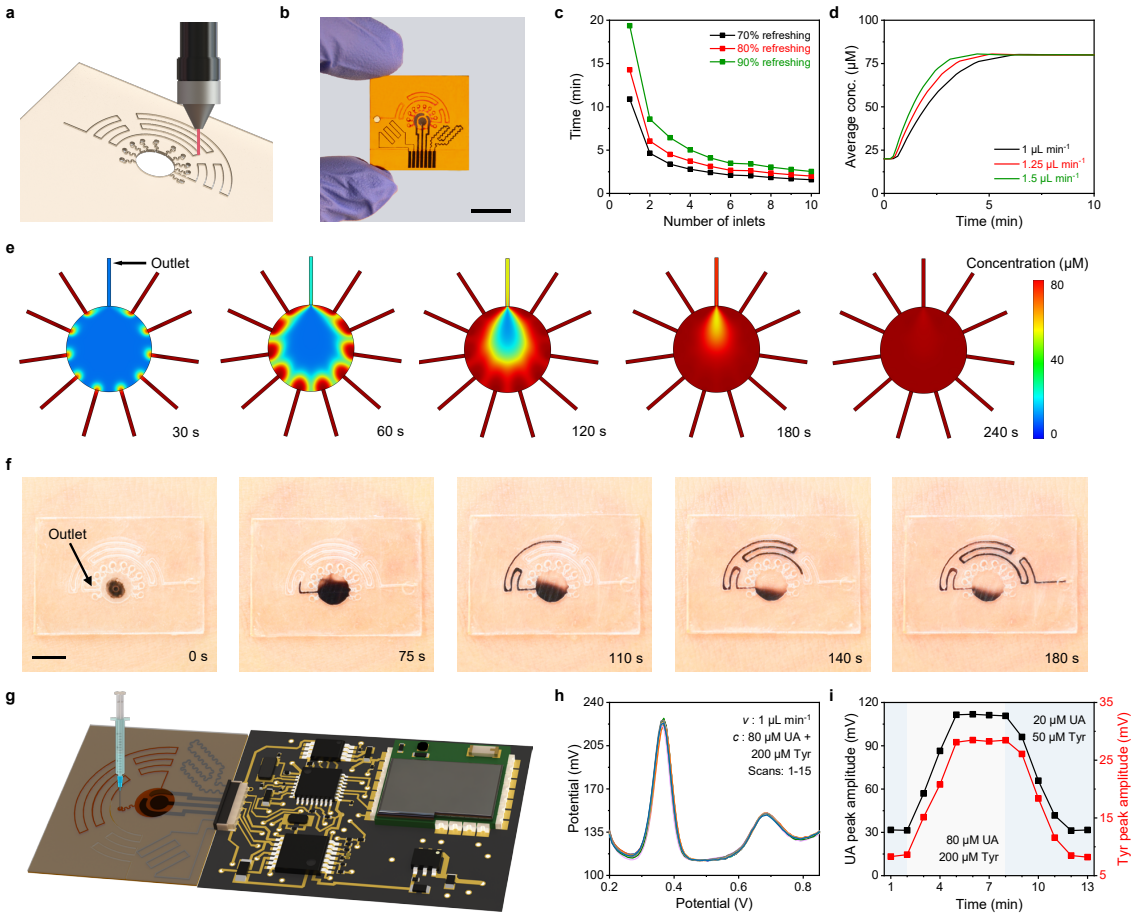

Figure 4-3. Design and characterization of the laser-engraved microfluidics. **a**, Schematic of vector-mode laser cutting for microfluidic fabrication. **b**, Photographic image of the microfluidic channels. Scale bar, 1 cm. **c**, Numerical simulation of the refreshing time required for the average concentration to reach 70%, 80% and 90% of the new solute concentration (that is, from 20 μM UA to 80 μM UA). Flow rate for each inlet, 0.15 μl min^{-1}. **d**, Simulations of the time evolution of the average concentration at different total inlet flow rates. **e**, Simulations of the distributions of solute concentration over the bottom surface of the reservoir at different time instances (inlet flow rate, 1.5 μl min^{-1}). **f**, Photographic images of the microfluidic sweat sampling during an iontophoresis-

induced sweat secretion process. Scale bar, 5 mm. **g**, Setup of the flow test to wirelessly monitor the analyte levels. A syringe pump is used to inject analyte solutions through an inlet. **h**, Successive DPV scans of 15 cycles in 80 μM UA and 200 μM Tyr with a fixed flow rate of 1 μl min^{-1}. The experiment was repeated three times independently with similar results. **i**, Dynamic and wireless UA sensing before and after switching the input UA and Tyr concentration from 20 and 50 μM, to 80 and 200 μM, respectively.

During the on-body trials, the microfluidic patch effectively sampled sweat with high temporal resolution (**Fig. 4-3f** and **Appendix C, Fig. C-3**). Moreover, it monitored sweat rate or sweat loss on different body parts through optical image analysis[13] (**Fig. 4-4**).

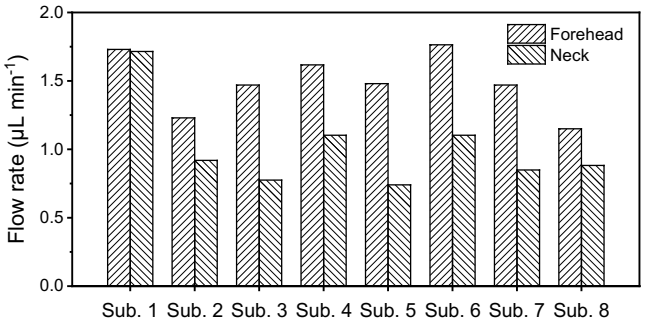

Figure 4-4. Inferred sweat rates from different locations of eight healthy subjects obtained via optical image analysis. Sub., subject.

Wireless and continuous sensing capabilities of the microfluidic-based sensor are performed via continuous analyte solution injection at physiological sweat rates (**Fig. 4-3g-i**).

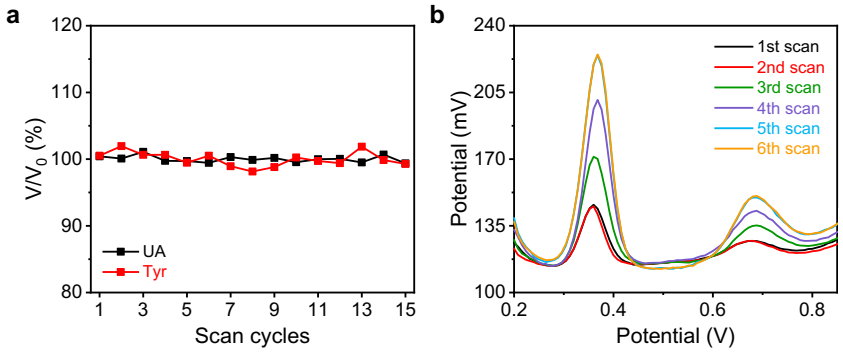

Figure 4-5. Characterization of the dynamics of the continuous microfluidic sensing. a, Stable peak amplitudes of twelve successive DPV scans in a solution containing 80 μM UA and 200 μM Tyr with a fixed flow rate of 1 μL min^{-1}. **b**, Dynamic DPV response of the microfluidic sensing when the inflow solution was switched from 20 μM UA and 50 μM Tyr to 80 μM UA and 200 μM Tyr with a fixed flow rate of 1 μL min^{-1}. A DPV scan was performed every minute (with a scan step of 8 mV and a scan cycle of 45 seconds).

The sensor patch reliably and continuously measured the UA and Tyr levels (±0.49% and ±1.07%, respectively) through successive DPV scans over a 15-cycle period (**Fig. 4-3h** and **Fig. 4-5a**). When the input solution was switched from 20 to 80 μM for UA and from 50 to 200 μM for Tyr, the patch took less than 3 min to reach a new stable reading with a hysteresis of ~1 min (**Fig. 4-3i** and **Fig. 4-5b**), indicating the high temporal resolution of the microfluidic sensing system. As illustrated in **Fig. 4-6**, with a 45-s scan cycle every 2.5 min, the microfluidic system showed very stable readings for UA and Tyr sensing during five successive scans (±1.25% and ±3.24 %, respectively) even when the flow rate was as small as 0.25 μl min^{-1}, indicating that the molecular depletion in the confined reservoir during DPV scans will not affect the sensing accuracy.

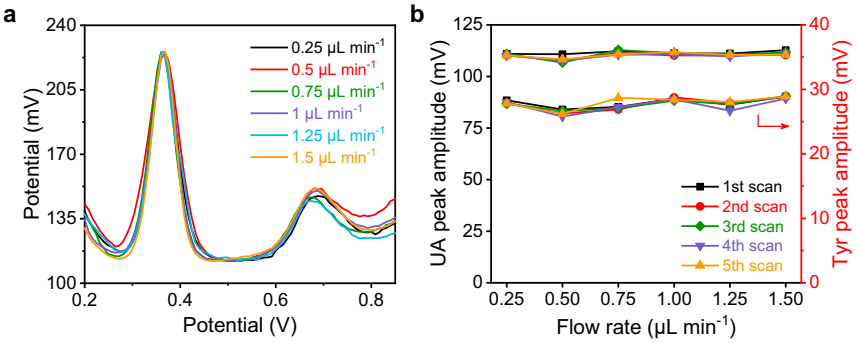

Figure 4-6. Characterization of continuous microfluidic sensing performance under different flow rates. a, The DPV plots of an LEG-CS for UA and Tyr sensing at different flow rates (from 0.25 to 1.5 μL min^{-1}). **b**, The peak amplitudes of UA and Tyr in 5 successive DPV scans (2.5 minutes per scan with a 45-s scan cycle length) with different flow rates (from 0.25 to 1.5 μL min^{-1}). Conditions, 80 μM UA and 200 μM Tyr.

4.2.3 Conclusion

The laser-engraved microfluidics presented above enables efficient microfluidic sweat sampling with fast filling and refreshing time for accurate continuous sensing of the target metabolites (Tyr and UA) in situ. Moreover, the laser-engraving manufacture technique endowed a great potential for mass production of such sweat microfluidics and the eventual realization of microfluidic sweat sensing.

4.3 Laser-engraved Microfluidics for Iontophoresis-induced Sweat

4.3.1 Materials and Methodology

Materials

Medical adhesives were purchased from 3 M and Adhesives Research. PI films (75 μm thick) were purchased from DuPont. PET films (12 μm thick) were purchased from McMaster-Carr.

Fabrication and characterization of microfluidic channels

The microfluidic module was fabricated using a 50 W CO_2 laser cutter (Universal Laser System) (**Appendix C, Fig.C-4**). Briefly, layers of double-sided and single-sided medical adhesives (3M) were patterned with channels, inlets, the iontophoresis gel outlines and reservoirs. For all microfluidic layers, the iontophoresis gel outlines were patterned to enable the current flow from the top PI electrode layer. The bottom layer, which is the double-sided adhesive layer in contact with the skin (accumulation layer), was patterned with a sweat accumulation well (3M 468MP, laser parameters: power 60%, speed 90%, PPI 1,000). The second layer (the inlet layer), in contact with the accumulation layer, was patterned with the multiple inlets (12-μm-thick PET, laser parameters: power 20%, speed 100%, PPI 1,000). The third layer (channel layer), in contact with the inlets layer, was patterned with microfluidic channels (Adhesives Research 93049, laser parameters: power 45%, speed 100%, PPI 1,000). The fourth layer (reservoir layer), sandwiched between the channel layer and the electrode PI layer, was patterned with the reservoir and the outlet (3M 468MP, laser parameters: power 60%, speed 90%, PPI 1,000). The reservoir is an ellipse with a 5.442 mm major axis and a 4.253 mm minor axis to fully enclose the active sensing area. The thickness of the channel layer is ~0.1 mm (Adhesives Research 93049), and the thickness of the reservoir layer is 0.13 mm (3M 468MP). The reservoir area is 18.17 mm^2, and thus the reservoir volume can be calculated as the area multiplied by the thickness of the reservoir layer (0.13 mm), which totals 2.36 μl.

Fabrication of agonist agent hydrogels

Hydrogels containing muscarinic agent carbachol was prepared as follows. Briefly, for anode gel, agarose (3% w/w) was added into de-ionized water and then heated to 250 °C under constant stirring. After the mixture was fully boiled and became homogeneous without agarose grains, the mixture was cooled down to 165 °C and 1% carbachol was added to the above mixture. Subsequently, the cooled mixture was slowly poured into pre-made cylindrical moulds or into assembled microfluidic

patch and solidified for 10 min at 4 °C. The cathode gel was prepared similarly except that NaCl (1% w/w) was used instead of carbachol

Refreshing time analysis and simulations

The refreshing time analyses were performed using numerical simulations (COMSOL). Three-dimensional models of different microfluidic designs with same dimensions of the actual device were created in Rhinoceros and imported into COMSOL Multiphysics. The mass transport process was simulated by numerically solving the Stokes equation for an incompressible flow coupled with convection–diffusion equation.

$$\nabla p = \mu \nabla^2 \boldsymbol{v}$$

$$\frac{\partial C}{\partial t} = D\nabla^2 C - \boldsymbol{v} \cdot \nabla C$$

p: pressure

$\boldsymbol{v}$: flow velocity

μ: solvent viscosity (water viscosity)

D: solute diffusivity (Tryptophan diffusivity)[14]

The Stokes equation is applicable as the Reynolds number is on the order of 10^{-2} in this device. For all simulation results (graphical and quantitative data), a total flow rate of $0.15\ \mu l\ min^{-1}$ is prescribed with the non-slip boundary condition on all channel walls, with the initial Trp concentration C_0 as 20 μM and supplied new Trp concentration C_n as 80 μM.

4.3.2 Results and Discussion

The flexible and disposable sweat induction and sampling patch consists of two carbachol-loaded iontophoresis module and a multi-inlet microfluidic module (**Fig.4-7** and **Appendix C, Fig.C-4**).

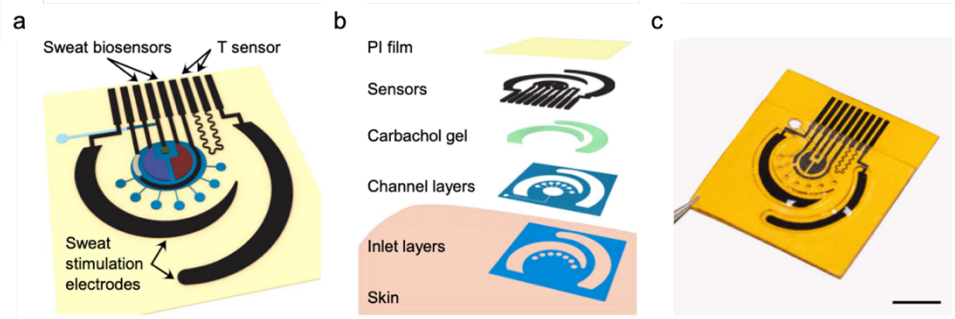

Figure 4-7. Schematic and optical photo of the microfluidic sweat induction and sampling patch. a,b, Schematic (**a**) and layer assembly (**b**) of the microfluidic 'NutriTrek' patch for sweat induction, sampling and biosensing. T, temperature. **c**, Images of a flexible sensor patch

Wearable system design for autonomous sweat induction, sampling, analysis and calibration

To enable on-body continuous metabolic and nutritional monitoring, the flexible sensor patch was designed to comprise an iontophoresis module for localized on-demand sweat induction, a multi-inlet microfluidic module for efficient sweat sampling, a multiplex LEG–MIP sweat nutrient sensor array for continuous AA analysis, and LEG-based temperature and electrolyte sensors for real-time AA sensor calibration (**Fig. 4-8a**).

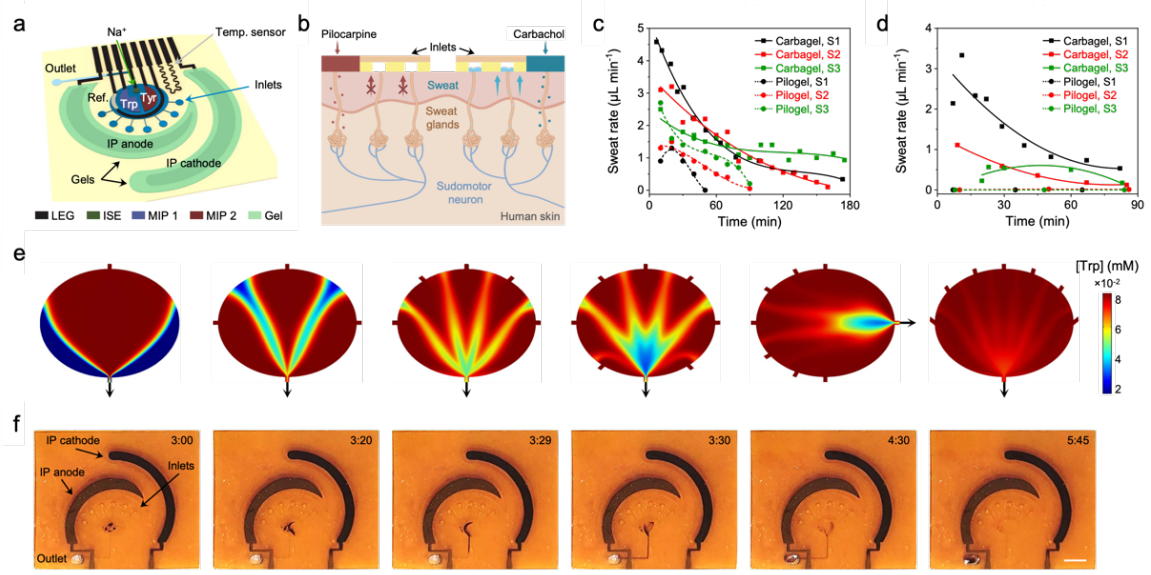

Figure 4-8. Wearable system design for autonomous sweat induction, sampling, analysis and calibration. **a**, Illustration of a multi-functional wearable sensor patch. ISE, ion-selective electrode. **b**, Schematic of localized sweat sampling based on iontophoretic sweat extraction with muscarinic agents: pilocarpine and carbachol. **c,d**, Localized sweat rates measured from the stimulated (**c**) and surrounding (**d**) skin areas after a 5-min iontophoresis with pilocarpine and carbachol. Solid and dashed curves represent quadratic-fit trendlines. S, subject. **e**, Numerically simulated Trp concentration ([Trp]) distributions in the microfluidic reservoir at 120 s after the inlet fluid changed from 20 to 80 μM Trp (flow rate 1.5 μl min^{-1}) (with varied designs in inlet number, angle span, and inlet and outlet orientation). **f**, On-body evaluation of the optimized flexible microfluidic patch for efficient carbachol-based iontophoretic sweat induction and surrounding sampling at rest. Timestamps represent the period (min) after a 5-min iontophoresis session. Black dye was used in the reservoir to facilitate the direct visualization of sweat flow in the microfluidics. Scale bar, 3 mm.

To make this wearable technology broadly applicable, particularly for sedentary individuals, we utilize here a custom-designed iontophoresis module consisting of the LEG anode and cathode coupled with hydrogels containing muscarinic agent for

sustainable sweat extraction. There are various muscarinic agent that could be used, but a careful selection was performed to enable a prolonged sweating session. Acetylcholine and methacholine are hydrolyzed by AChE and thus have a shorter sweating duration. On the other hand, the nicotinic activity of the cholinergic agents affects the indirect axon-reflex sweating and thus the area of the sweat response. For example, the β-methyl group of bethanechol limited the nicotinic activity and thus the sweating response is highly localized and mostly direct sweating underneath the placement of the iontophoresis gel. Detailed studies and summaries of the receptor activities and sweating response can be found in previous literature.[15–18] Carbachol was selected from various muscarinic agents as it allows the most efficient, repeatable and long-lasting sweat secretion from the surrounding sweat gland owing to its additional nicotinic effects[19] (**Fig. 4-8b-d**, **Fig. 4-9**, **Appendix C, Note C-1**).

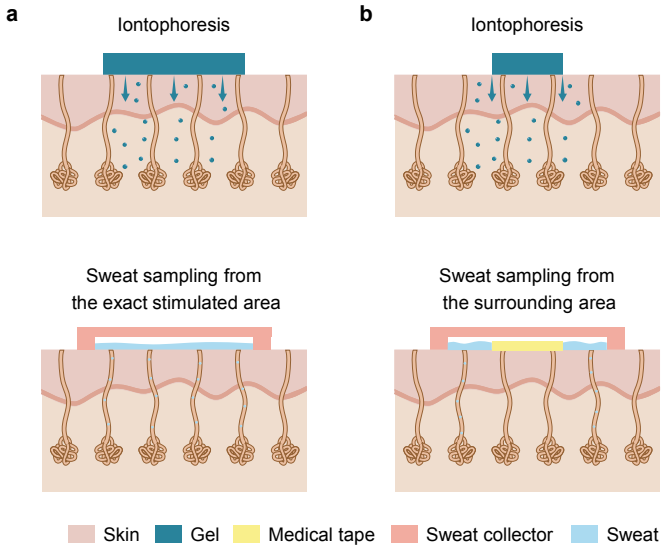

Figure 4-9. Investigation of the localized and surrounding sweat stimulation with muscarinic agents: carbachol and pilocarpine. a, Localized sweat stimulation with the muscarinic agent loaded hydrogels followed by periodic sweat collection from the exact stimulated skin area after hydrogel removal. The obtained sweat rate data over time was shown in **Fig. 4-8c**. **b**, Localized sweat stimulation with the muscarinic agent loaded hydrogels followed by periodic sweat collection

from the surrounding skin area with the exact stimulated skin area blocked by medical tape. The obtained sweat rate data over time was shown in **Fig. 4-8d**.

In contrast, the classic sweat-inducing agent—pilocarpine—used by the standard sweat test and previously reported wearable systems[10–12] offers only a short period of sweat and very limited sweat rate from the neighboring sweat glands (**Fig. 4-8b-d**). Furthermore, sampling the mixture of the leaked sweat underneath the pilocarpine gel and the gel fluid could result in substantial wearable sensor errors and fail to provide real-time information owing to the absence of efficient sweat refreshing. A very small current (50–100 μA) is used for our iontophoresis module, compared with commonly used 1–1.5 mA[10–12], greatly reducing the risk of skin irritation. To maximize the efficiency of low-volume sweat sampling and improve the temporal resolution of wearable sensing, a compact and flexible microfluidic module was carefully designed to isolate sweat sampling areas from iontophoresis gels. Numerical simulations were performed to optimize the geometric design of the microfluidic module, including inlet number, angle span, orientation and flow direction with respect to the reservoir geometry (**Fig. 4-8e**).

For all simulation runs (graphical and quantitative data), a total flow rate of 0.15 μl min^{-1} is prescribed with the non-slip boundary condition on all channel walls, with the initial Trp concentration C_0 as 20 μM and supplied new Trp concentration C_n as 80 μM. The concentration distribution over the bottom surface of the chamber is displayed at different time instances in **Figs.4-10, 4-11**; and the time for the average volume concentration to reach 90% C_n and 95% C_n is displayed in **Table 4-1**.

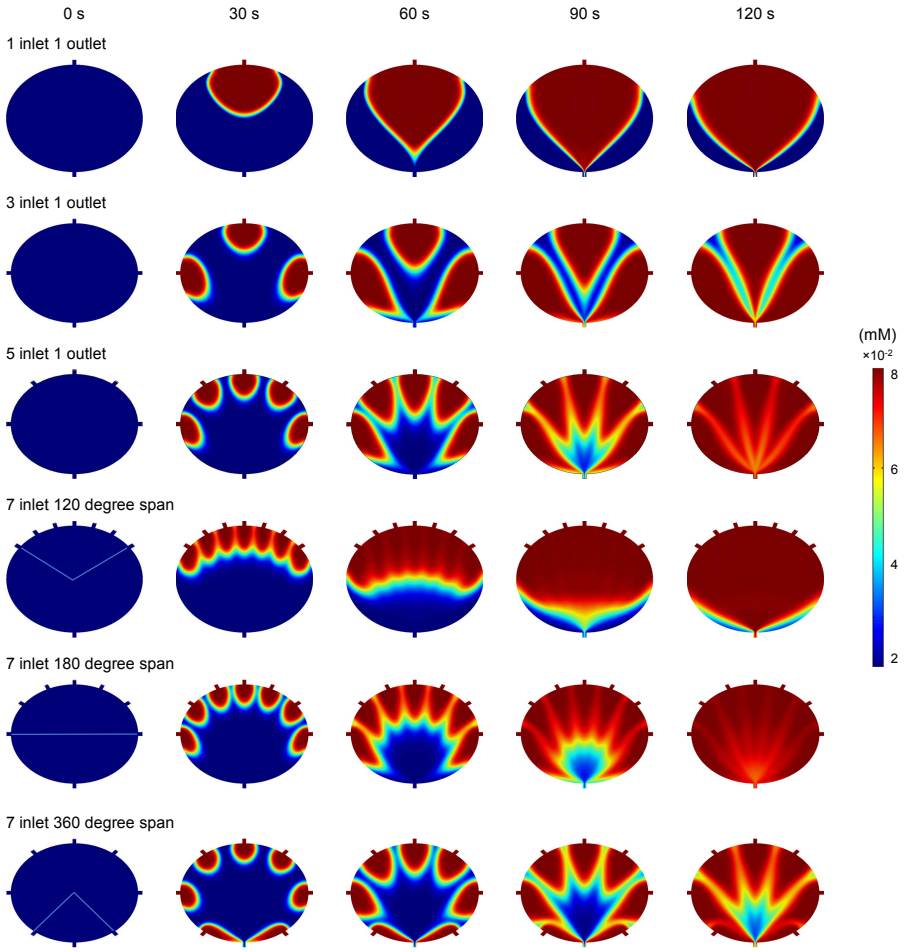

Figure 4-10. Effects of inlet numbers and inlet span of the microfluidics on target refreshing. The figure illustrates numerical simulation results of Trp level distributions at 120 s after switching the input from 20 to 80 μM Trp (flow rate, 1.5 μL min^{-1}) (with varied designs in inlet number and angle span). As shown in above, fewer inlets can lead to a uniform concentration near the inlet area, but a larger dispersion in the bottom edge area where sensors are located. The smaller angle span could also lead to dispersion in the area opposite to inlets; an angle span too large could yield a dispersion in the middle of the reservoir. Balancing the inlet number and ranges, the optimized condition is 7 inlets in 180° span.

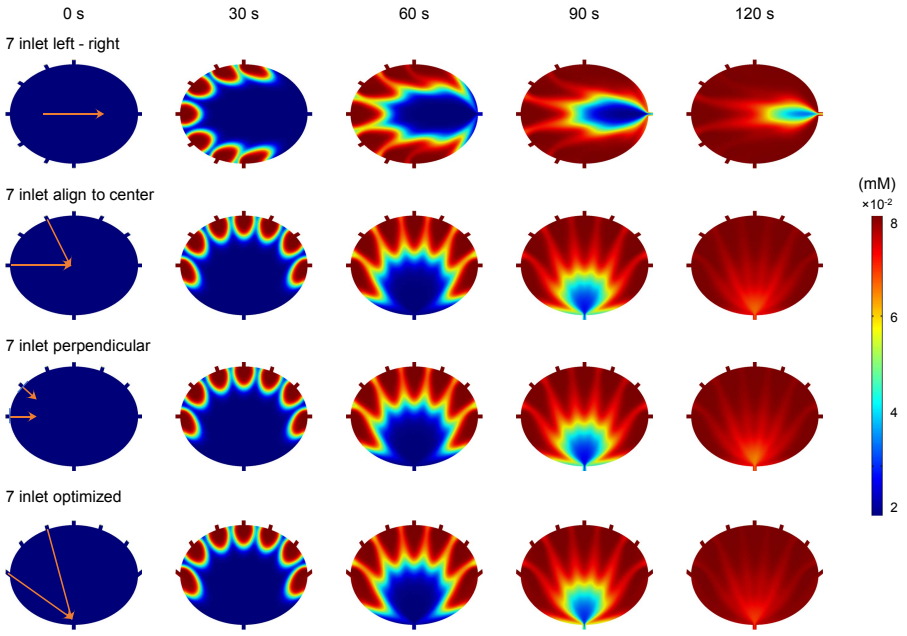

Figure 4-11. Effects of inlet-outlet orientations of the microfluidics on target refreshing. The figure illustrates numerical simulation results of Trp level distributions at 120 s after switching the input from 20 to 80 μM Trp (flow rate, 1.5 μL min^{-1}) (with varied designs in inlet-outlet orientation). When the inlets-outlet orientation is along the longer axis of the reservoir, much more time is needed to update the volume concentration. When the inlets are aligned to center of the reservoir (radial) or perpendicular to the edge of the reservoir, more time is needed to update the volume concentration compared to the optimized condition, where inlets are aligned towards the outlet.

Table 4-1. Numerically simulated time for average volumetric concentration to reach 90% and 95% of the newly supplied concentration. The conformation with 7 inlet, 180° span and aligned to outlet yields the smallest time for the average volumetric concentration to reach close to the newly updated concentration supplied at inlets (fastest refreshing time).

Comparison with different microfluidic designs (flow rate: 1.5 μL min^{-1}; [Trp]: 20-80 μM)

Inlet #	Span	Orientation	Flow direction (along long/short axis)	Time to reach 90% update (s)	Time to reach 95% update (s)
1	N/A	N/A	Short	133	182
3	180	Radial	Short	127.2	185
5	180	Radial	Short	98	118
7	180	Radial	Short	95	108.6
7	120	Radial	Short	93.7	111
7	270	Radial	Short	127.6	155
7	180	Radial	Long	103.8	123
7	180	Perpendicular to tangent	Short	95.6	109.7
7	180	Aligned to outlet	Short	91	104.7

We call this time to reach new concentration as refreshing time, and it is especially important as it captures how long it takes the sensor to detect an updated concentration in the reservoir. Specifically, increased number of inlets and a smaller angular span of the inlets improves the rate of refreshing, as shown in **Fig. 4-10** and **Table 4-1**. Therefore, we chose the 7-inlet with 120 angular span conformation. Based on this conformation, we further tuned the orientation of inlets and investigated if the inlet flow direction affects the refreshing time. As shown in **Fig. 4-11** and **Table 4-1**, the flow along the shorter axis of the reservoir with inlets aligned to the reservoir exit yields the shortest refreshing time. With numerical simulations of our optimized geometry design, as illustrated in **Fig. 4-10**, the time to reach 90% of the C_n is around 2 min (Trp, C_0 initially at 20 μM and C_n at 80 μM, sweat rate of 1.5 μL min^{-1}).

With the optimized design for sweat induction and sampling, sweat can be conveniently induced locally and readily sampled with the multi-inlet microfluidics

over a prolonged period (**Fig. 4-8c,f** and **Appendix C, Fig. C-5**). The simulation result on the refreshing time was also validated with an experimental flow test shown in **Fig. 4-12**. As demonstrated in **Fig. 4-13**, with a 30-s DPV scan cycle every 2.5 minutes, the LEG sensor displayed very stable reading for Trp sensing during 3 successive scans at a low flow rate of 0.15 µL min^{-1}, indicating that the refreshment in the confined reservoir under slow sweat rates will not affect the wearable sensing accuracy. Therefore, at the physiological sweat rates ranging from 0.15 µl min^{-1} to 3 µl min^{-1}, our wearable sensor patch could provide reliable and accurate analysis of the dynamic changes of the AA levels.

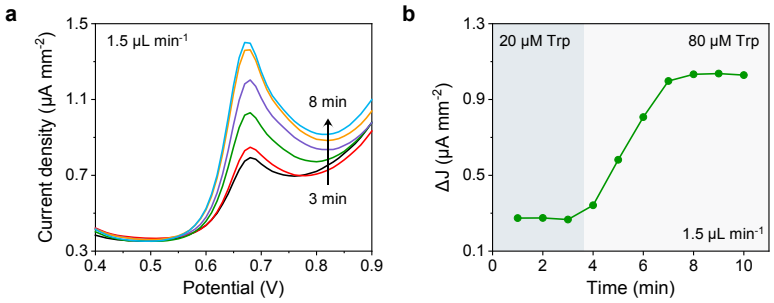

Figure 4-12. Characterization of the dynamics of the continuous microfluidic sensing. a,**b**, DPV voltammograms (**a**) and corresponding peak height current densities (**b**) of an LEG Trp sensor during a flow test with the input Trp level increased from 20 to 80 µM. A fixed flow rate of 1.5 µL min^{-1} was used and DPV scans were performed every minute.

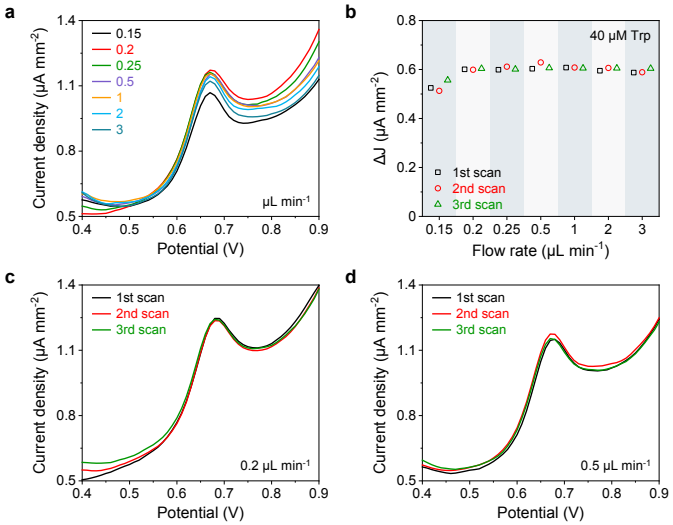

Figure 4-13. Characterization of continuous microfluidic sensing performance under different flow rates. a, The DPV voltammograms of an LEG Trp sensor at different flow rates (from 0.15 to 3 μL min^{-1}). **b**, The peak height current densities of the Trp sensor in 3 successive DPV scans under each flow rate. **c**,**d**, DPV voltammograms of an LEG Trp sensor in three repetitive scans at a flow rate of 0.2 μL min^{-1} (**c**) and 0.5 μL min^{-1} (**d**), respectively. Conditions, one scan every 2.5 min in 40 μM Trp.

4.3.3 Conclusion

As the majority of wearable biosensors rely on vigorous exercise to access sweat and are not suitable for daily continuous use, our mass-producible sweat induction and sampling microfluidics offer a great alternative for efficient on-demand sweat sensing in sedentary individuals. With optimized multi-inlet microfluidic sudomotor axon reflex sweat sampling, we envision that this wearable technology could play a crucial role in the realization of noninvasive in situ sweat monitoring for personalized medicine.

Bibliography of Chapter 4

1. Baker, L. B. Physiology of sweat gland function: The roles of sweating and sweat composition in human health. *Temperature* **6**, 211–259 (2019).
2. Harshman, S. W. *et al.* Metabolomic stability of exercise-induced sweat. *Journal of Chromatography B* **1126–1127**, 121763 (2019).
3. Harshman, S. W. *et al.* The proteomic and metabolomic characterization of exercise-induced sweat for human performance monitoring: A pilot investigation. *Plos One* **13**, e0203133 (2018).
4. Heikenfeld, J. *et al.* Accessing analytes in biofluids for peripheral biochemical monitoring. *Nature Biotechnology* **37**, 407–419 (2019).
5. Ray, T. R. *et al.* Soft, skin-interfaced sweat stickers for cystic fibrosis diagnosis and management. *Science Translational Medicine* **13**, eabd8109 (2021).
6. Choi, J., Kang, D., Han, S., Kim, S. B. & Rogers, J. A. Thin, soft, skin-mounted microfluidic networks with capillary bursting valves for chrono-sampling of sweat. *Advanced Healthcare Materials* **6**, 1601355 (2017).
7. Agrawal, K., Waller, J. D., Pedersen, T. L. & Newman, J. W. Effects of stimulation technique, anatomical region, and time on human sweat lipid mediator profiles. *Prostaglandins & Other Lipid Mediators* **134**, 84–92 (2018).
8. Bariya, M., Nyein, H. Y. Y. & Javey, A. Wearable sweat sensors. *Nature Electronics* **1**, 160–171 (2018).
9. Sonner, Z., Wilder, E., Gaillard, T., Kasting, G. & Heikenfeld, J. Integrated sudomotor axon reflex sweat stimulation for continuous sweat analyte analysis with individuals at rest. *Lab on a Chip* **17**, 2550–2560 (2017).

10. Sempionatto, J. R. *et al.* An epidermal patch for the simultaneous monitoring of haemodynamic and metabolic biomarkers. *Nature Biomedical Engineering* **5**, 737–748 (2021).

11. Emaminejad, S. *et al.* Autonomous sweat extraction and analysis applied to cystic fibrosis and glucose monitoring using a fully integrated wearable platform. *Proceedings of the National Academy of Sciences of the United States of America* **114**, 4625–4630 (2017).

12. Kim, J. *et al.* Noninvasive alcohol monitoring using a wearable tattoo-based iontophoretic-biosensing system. *ACS Sensors* **1**, 1011–1019 (2016).

13. Choi, J., Ghaffari, R., Baker, L. B. & Rogers, J. A. Skin-interfaced systems for sweat collection and analytics. *Science Advances* **4**, eaar3921 (2018).

14. Ma, Y., Zhu, C., Ma, P. & Yu, K. T. Studies on the diffusion coefficients of amino acids in aqueous solutions. *Journal of Chemical & Engineering Data* **50**, 1192–1196 (2005).

15. Low, P. A., Opfer-Gehrking, T. L. & Kihara, M. In vivo studies on receptor pharmacology of the human eccrine sweat gland. *Clinical Autonomic Research* **2**, 29–34 (1992).

16. Simmers, P., Li, S. K., Kasting, G. & Heikenfeld, J. Prolonged and localized sweat stimulation by iontophoretic delivery of the slowly-metabolized cholinergic agent carbachol. *Journal of Dermatological Science* **89**, 40–51 (2018).

17. Low, P. A., Caskey, P. E., Tuck, R. R., Fealey, R. D. & Dyck, P. J. Quantitative sudomotor axon reflex test in normal and neuropathic subjects. *Annals of Neurology* **14**, 573–580 (1983).

18. Aromdee, C., Fawcett, J. P., Ferguson, M. M. & Ledger, R. Serum pilocarpine esterase activity and response to oral pilocarpine. *Biochemical and Molecular Medicine* **59**, 57–61 (1996).

19. Riedl, B., Nischik, M., Birklein, F., Neundörfer, B. & Handwerker, H. O. Spatial extension of sudomotor axon reflex sweating in human skin. *Journal of the Autonomic Nervous System* **69**, 83–88 (1998).

A p p e n d i x C

SUPPLEMENTARY INFORMATION FOR CHAPTER 4

Materials from this chapter appears in "Yang, Y.; Song, Y.; Bo, X.; Min, J.; Pak, O. S.; Zhu, L.; Wang, M.; Tu, J.; Kogan, A.; Zhang, H.; Hsiai, T. K.; Li, Z.; Gao, W. A laser-engraved wearable sensor for sensitive detection of uric acid and tyrosine in sweat. *Nature biotechnology* **38**, 217–224 (2020) doi:10.1038/s41587-019-0321-x" and "Wang, M.; Yang, Y.; Min, J.; Song, Y.; Tu, J.; Mukasa, D.; Ye, C.; Xu, C.; Heflin, N.; McCune, J. S.; Hsiai, T. K.; Li, Z.; Gao, W. A wearable electrochemical biosensor for the monitoring of metabolites and nutrients. *Nature Biomedical Engineering* 1–11 (2022) doi: 10.1038/s41551-022-00916-z".

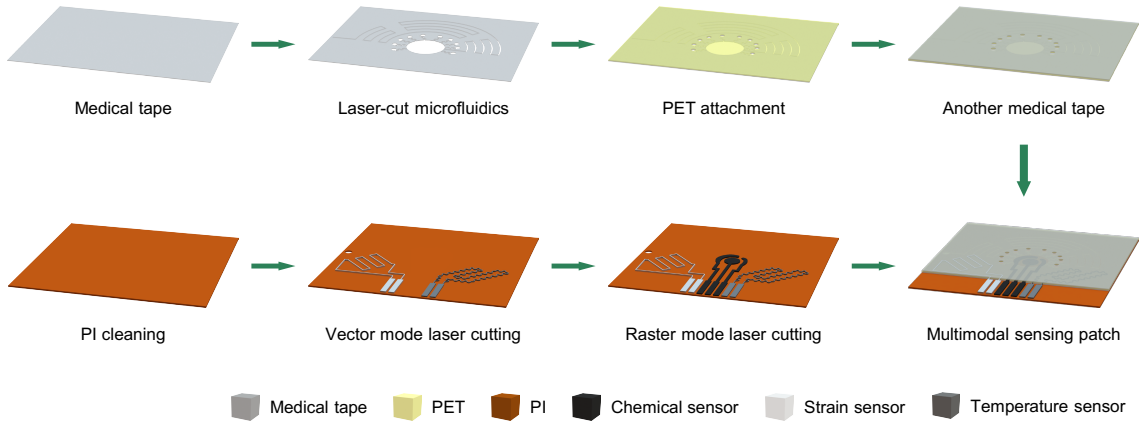

Figure C-1. Fabrication process of the microfluidic patch

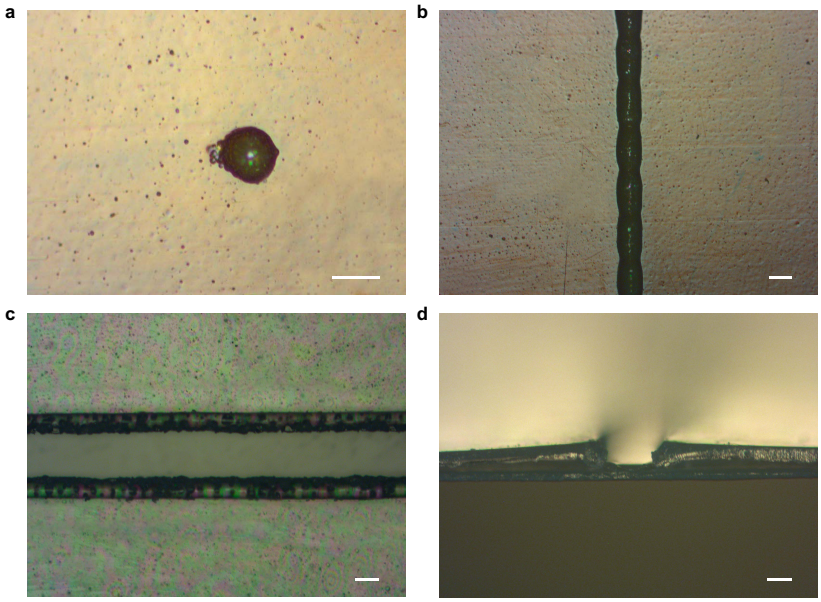

Figure C-2. Microscopic images showing the resolution of the laser engraving. a–d, a graphene microelectrode fabricated by the raster mode (a), a graphene micropattern fabricated by vector mode (b), and a microfluidic channel fabricated by vector mode under top view (c) and cross-sectional view (d). Scale bars, 100 μm

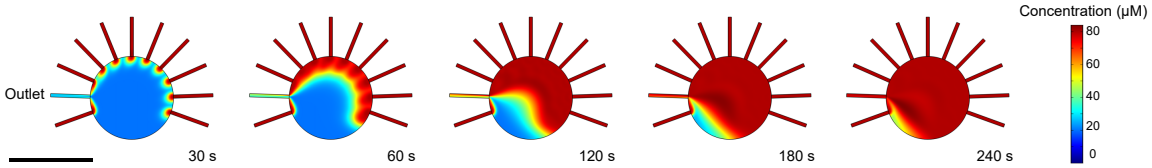

Figure C-3. The numerical simulation showing the fluidic dynamics in the reservoir of the lab-on-skin sensor patch. The dimension used here are based on actual sensor design used in this work. Scale bar, 5 mm.

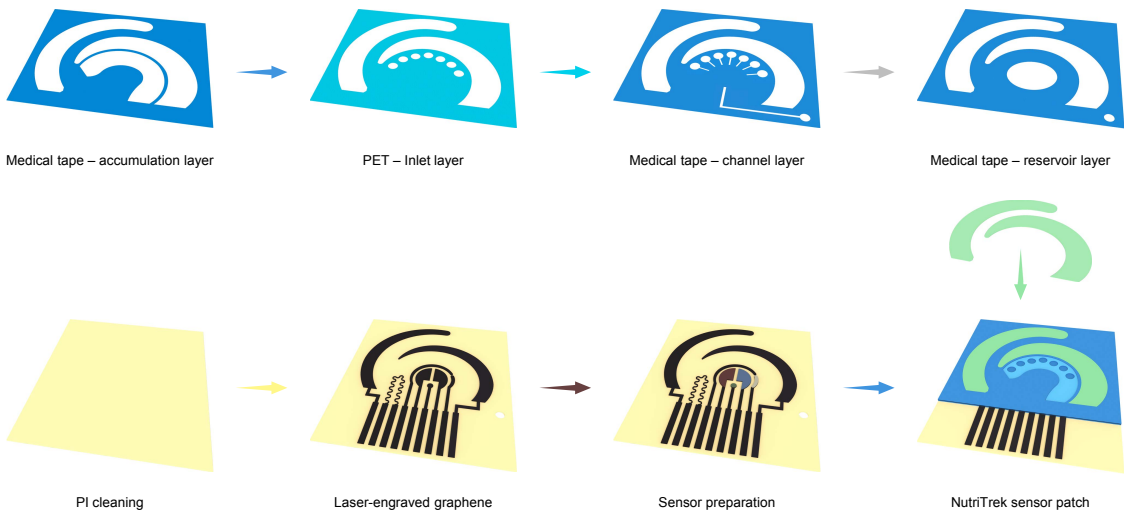

Figure C-4. Fabrication process of the multifunctional flexible wearable sensor patch.

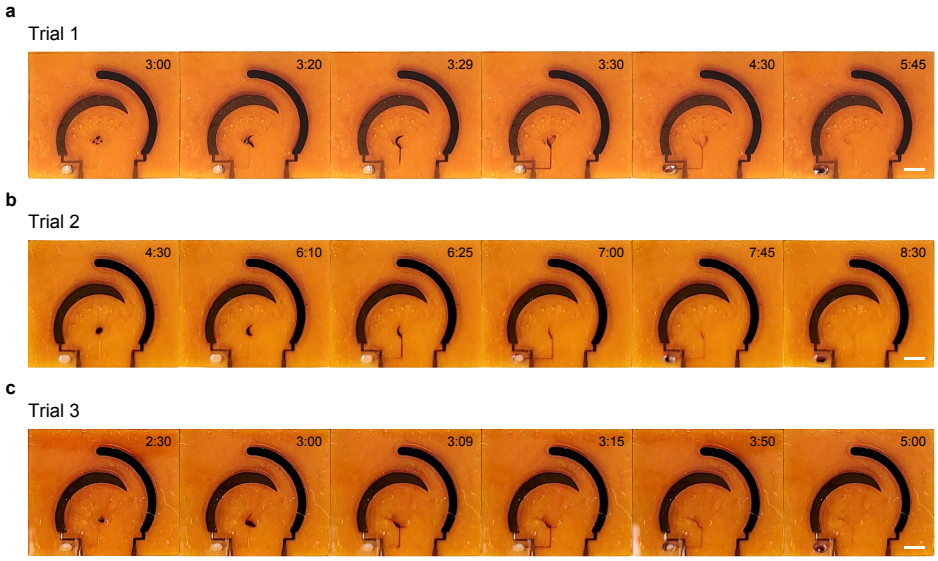

Figure C-5. On-body evaluation of the microfluidic flexible sensor patches for carbagel-based iontophoretic sweat stimulation and sampling at rest. Timestamps represent the period (min) after a 5-min iontophoresis session. Black dye was used in the reservoir to facilitate the direct visualization of sweat flow in the microfluidics. Scale bars, 3 mm

Note C-1. Iontophoresis-based localized sweat stimulation

Iontophoresis is a common procedure that enables on-demand sweat induction by transdermal delivery of a muscarinic agonist that stimulates sweat gland to produce sweat. Despite its widespread use in cystic fibrosis diagnosis, the choice of agonists is still mostly limited to pilocarpine and acetylcholine, which only affect the sweat glands where the agonist is delivered. Here we use carbachol, a muscarinic agonist that has nicotinic effects, which enable the sudomotor axon reflex sweating (SAR) and sweat glands neighboring the dosed area also produce sweat for sampling (**Fig. 4-8b**).[1] Carbachol is a cholinomimetic ester more resistant to acetylcholinesterase hydrolysis than acetylcholine and enables a prolonged sweat production time. Using a commercial iontophoresis device, we compared the sweat rate stimulated by commercial pilogels loaded with pilocarpine and custom made carbagels (**Fig. 4-9**),

both with the same geometry and the same dosing area (a circle with a 27 mm diameter). Using the same commercial sweat collectors and the same sampling area (a concentric circle with a 28.4 mm diameter), the total sweat rates (of the dosed area and the surrounding area) of three subjects induced by carbagels is much higher and lasts longer than those induced by commercial pilogels (**Fig. 4-8c**). Moreover, with the same dosing area (a 11 mm diameter circle) blocked (by a 13 mm diameter adhesive disk) and the same commercial sweat collector (a concentric circle with a 28.4 mm diameter), the carbagels elicited significant SAR sweat rates in 3 subjects compared to none by pilogels (**Fig. 4-8d**). To avoid the potential contamination from gel, we harvest only the SAR sweat and the high sweat rate obtained is sufficient for continuous chemical sensing (**Appendix C, Fig. C-5**).

Bibliography of Appendix C

1. Simmers, P., Li, S. K., Kasting, G. & Heikenfeld, J. Prolonged and localized sweat stimulation by iontophoretic delivery of the slowly-metabolized cholinergic agent carbachol. *Journal of Dermatological Science* **89**, 40–51 (2018).

C h a p t e r 5

INTEGRATED MICROFLUIDIC SWEAT SENSOR FOR METABOLIC MONITORING

Materials from this chapter appears in "Yang, Y.; Song, Y.; Bo, X.; Min, J.; Pak, O. S.; Zhu, L.; Wang, M.; Tu, J.; Kogan, A.; Zhang, H.; Hsiai, T. K.; Li, Z.; Gao, W. A laser-engraved wearable sensor for sensitive detection of uric acid and tyrosine in sweat. *Nature Biotechnology* **38**, 217–224 (2020) doi:10.1038/s41587-019-0321-x" and "Wang, M.; Yang, Y.; Min, J.; Song, Y.; Tu, J.; Mukasa, D.; Ye, C.; Xu, C.; Heflin, N.; McCune, J. S.; Hsiai, T. K.; Li, Z.; Gao, W. A wearable electrochemical biosensor for the monitoring of metabolites and nutrients. *Nature Biomedical Engineering* 1–11 (2022) doi: 10.1038/s41551-022-00916-z"

5.1 Introduction

Wearable devices[1,2], such as wearable sweat sensors[3–5], have the potential to capture changes in health rapidly, continuously, and non-invasively. In order to be suitable for wearable use, system-level integration is necessary for the development of wearable sweat sensors. In Chapter 5.2, our efforts on system integration evaluations are presented.

Sweat contains rich molecular information for probing personal health condition.[6] For example, chloride concentration in sweat is the gold standard to diagnose cystic fibrosis[7], and glucose concentration in sweat is being intensively explored for diabetes management. [5,7,8] In Chapter 5.3, our integrated microfluidic sweat sensing device is detailed for *in situ* monitoring towards metabolic health monitoring, with a focus on gout and metabolic syndrome management.

5.2 Wearable System Development and Validation

5.2.1 Wearable System Integration

The flexible and disposable sensor patch consists of carbachol-loaded iontophoresis electrodes, a multi-inlet microfluidic module, a multiplexed MIP nutrient sensor array, a temperature sensor, and an electrolyte sensor (**Fig. 5-1**). The sensor patch can be easily attached to skin with conformal contact and interfaces with a miniaturized electronic module in the form of a FPCB for on-demand iontophoresis control, *in situ* signal processing and wireless communication with the user interfaces through Bluetooth (**Fig. 5-1g** and **Appendix D, Fig. D-1,D-2**).

Figure 5-1. Schematics and images of the biomimetic wearable biosensor 'NutriTrek'. a, Circulating nutrients such as amino acids are associated with various physiological and metabolic conditions. **b**, Schematic of the wearable 'NutriTrek' that enables metabolic monitoring through a synergistic fusion of laser-engraved graphene, redox-active nanoreporters, and biomimetic 'artificial antibodies'. **c**,**d**, Schematic (**c**) and layer assembly (**d**) of the microfluidic 'NutriTrek' patch for sweat induction, sampling, and biosensing. T, temperature; PI, polyimide. **e**,**f**, Images of a

flexible sensor patch (**e**) and a skin-interfaced wearable system (**f**). Scale bars, 5 mm (**e**) and 2 cm (**f**). **g**, Block diagram of electronic system of 'NutriTrek'. The modules outlined in red dashes are included in the smartwatch version. ADC, analog-to-digital converter; DAC, digital-to-analog converter; CPU, central processing unit; GPIO, general-purpose input/output; POT, potentiometry; In-Amp, instrumentation amplifier; MCU, microcontroller; SPI, serial peripheral interface; TIA, transimpedance amplifier; UART, universal asynchronous receiver-transmitter. **h**, Custom mobile application for real-time metabolic and nutritional tracking. **i**, 'NutriTrek' smartwatch with a disposable sensor patch and an electrophoretic display. Scale bars, 1 cm (top) and 5 cm (bottom).

The block diagram of the electronic system (**Fig. 5-1g** and **Appendix D, Fig. D-2**) represents both the wearable electronic patch and the smart watch that can (i) induce sweat *via* iontophoresis and (ii) monitor sweat via electrochemical methods. The sweat induction and the sweat sensing procedures are initiated and controlled by the microcontroller when it receives a user command from the Bluetooth module. For sweat induction, programmable iontophoretic current is generated by a voltage controlled current source. For the optimized design, a 100-μA current (~2.6 μA mm^{-2}) was applied for on-body iontophoresis sweat induction using the flexible microfluidic patch, with current output check and protection circuit (**Appendix D, Note D-1**). For sweat sensing, the voltammetry involves controlled voltage potentials between the electrodes. A series voltage reference and a digital to analog converter (DAC) is used to generate a dynamic potential bias across the reference and working electrodes. A bipotentiostat circuit is constructed by a control amplifier and two transimpedance amplifiers. An instrumentation amplifier is used for potentiometric measurements and a voltage divider is used for the resistive temperature sensor. All analog voltage signals are acquired by the microcontroller's built-in analog-to-digital converter (ADC) channels, processed, then transmitted over Bluetooth to a user device. A custom mobile app 'NutriTrek' was developed to process, display, and store the dynamic metabolic information monitored by the

wearable sensors (**Fig. 5-1h**). The wearable system was also integrated into a smartwatch with an electronic paper display (**Fig. 5-1i**).

While on-board signal conditioning, processing and wireless transmission provides feasible scheme for wearable sensing, *in situ* sweat analysis poses more factors to consider to achieve accurate sensing outcome due to complex and interpersonally varied sweat composition and demands technological innovations for accurate on-body sensing, unlike classic bioaffinity sensors which operate in optimal buffers. For example, for direct LEG-MIP Trp sensing, a DPV scan in sweat even before target/MIP recognition could lead to an oxidation peak as a small amount of electroactive molecules (e.g., Trp and Tyr) can be oxidized on the surface of MIP layer; after recognition and binding of Trp into the MIP cavities, a substantially higher current peak height can be obtained; measuring difference of the two peak heights allows more accurate bound Trp measurement directly in sweat with high selectivity (**Fig. 5-2a-c**).

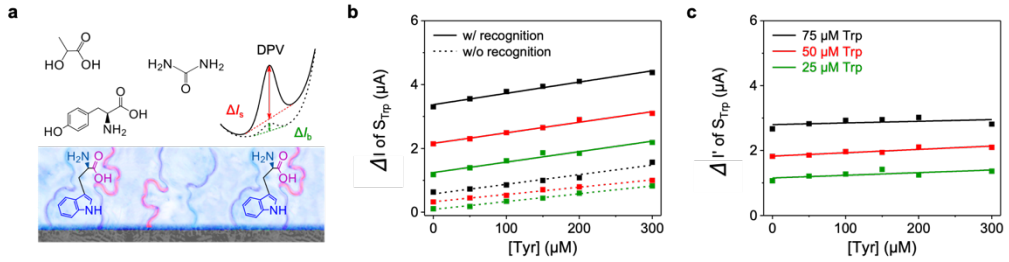

Figure 5-2. The two-scan sensor calibration strategy enabling selective Trp sensing in situ in the presence of Tyr. a, scheme of the two-scan strategy. **b,** peak height currents directly from the DPV scan before and after recognition incubation time. **c,** peak height difference caused by target recognition gives consistent sensing outcome in the presence of different Tyr levels. ΔI, peak height current; ΔI', peak height difference caused by target recognition.

Moreover, the sensing outcome is influenced by temperature and ionic strength (**Fig. 5-3**), so real-time readings from an LEG-based strain-resistive temperature sensor and an ion-selective Na^+ sensor can be used to calibrate the LEG-MIP reading(**Fig.**

5-4). Considering that sweat rate during exercise was reported to have influence on certain biomarker levels; we could use sweat Na^+ level (which showed a linear correlation with sweat rate) to further calibrate the nutrient levels for personalized analysis. This unique transduction strategy involving both the two-step DPV scans and the temperature/electrolyte calibrations allows us to obtain accurate reading continuously in sweat during on-body use (**Fig. 5-5**).

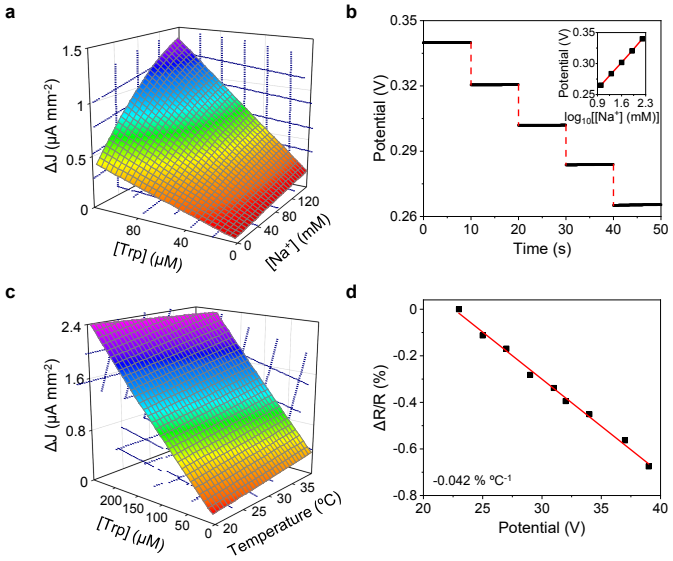

Figure 5-3. The performance of the LEG-MIP sensor under varied temperature and electrolyte levels. a, Color map showing the dependence of the LEG-MIP Trp sensor response on Trp and Na^+ concentrations. **b**, Open circuit potential responses of an LEG-based Na^+ sensor in the presence of varied Na^+ concentrations. Inset, calibration plot of an LEG-based Na^+ sensor. **c**, Color map showing the dependence of the LEG-MIP Trp sensor response on Trp and temperature. **d**, Calibration plot of an LEG-based temperature sensor in the physiological temperature range. Solid calibration lines in **b**,**d** represent linear fit trendlines.

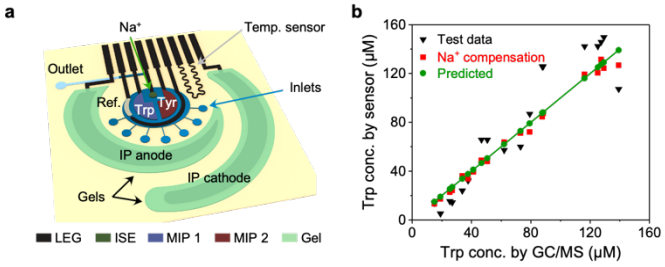

Figure 5-4. Mutiplexed sensing for calibrating MIP sensing outcome. **a**, Illustration of a multifunctional wearable sensor patch. **b**, Electrolyte calibration of the AA sensor reading.

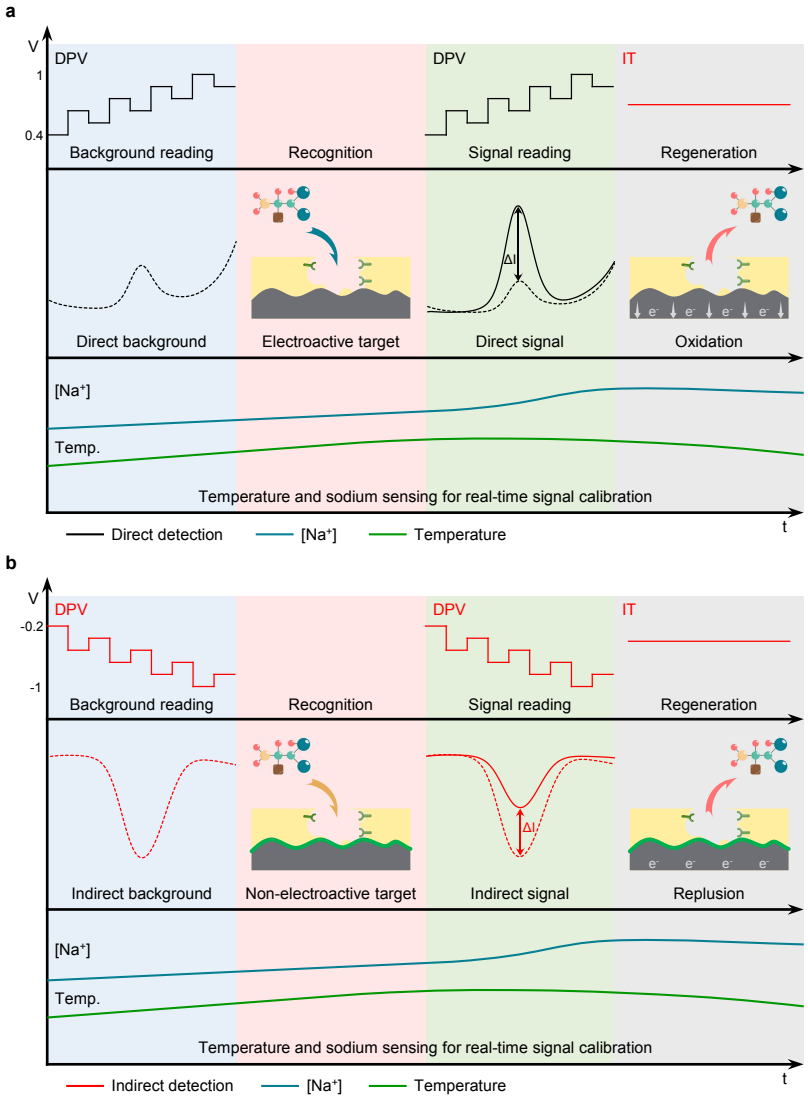

Figure 5-5. *In situ* calibration strategies of the wearable LEG-MIP sensors involving a two-step DPV-scan calibration and real-time temperature/electrolyte calibrations. (**A** and **B**) *In situ* calibration strategies of the MIP-LEG sensor with direct detection mechanism (**a**) and the MIP-RAR (AQCA used here for wearable sensing)-LEG sensor with indirect detection mechanism (**b**) to obtain accurate reading continuously during on-body use.

5.2.2 System Evaluation in Human Subjects

Evaluation of the wearable system was conducted first *via* sensing of sweat Trp and Tyr in human subjects during a constant-load cycling exercise trial (**Fig. 5-6a–d** and **Appendix D, Fig. D-3**). The DPV data from the sensors were wirelessly transmitted along with temperature and Na^+ sensor readings to the mobile app that automatically extracted the oxidation peaks using a custom developed iterative baseline correction algorithm (**Fig. 5-6e** and **Appendix D, Fig. D-4**) and performed calibration for the accurate quantification of sweat Tyr and Trp.

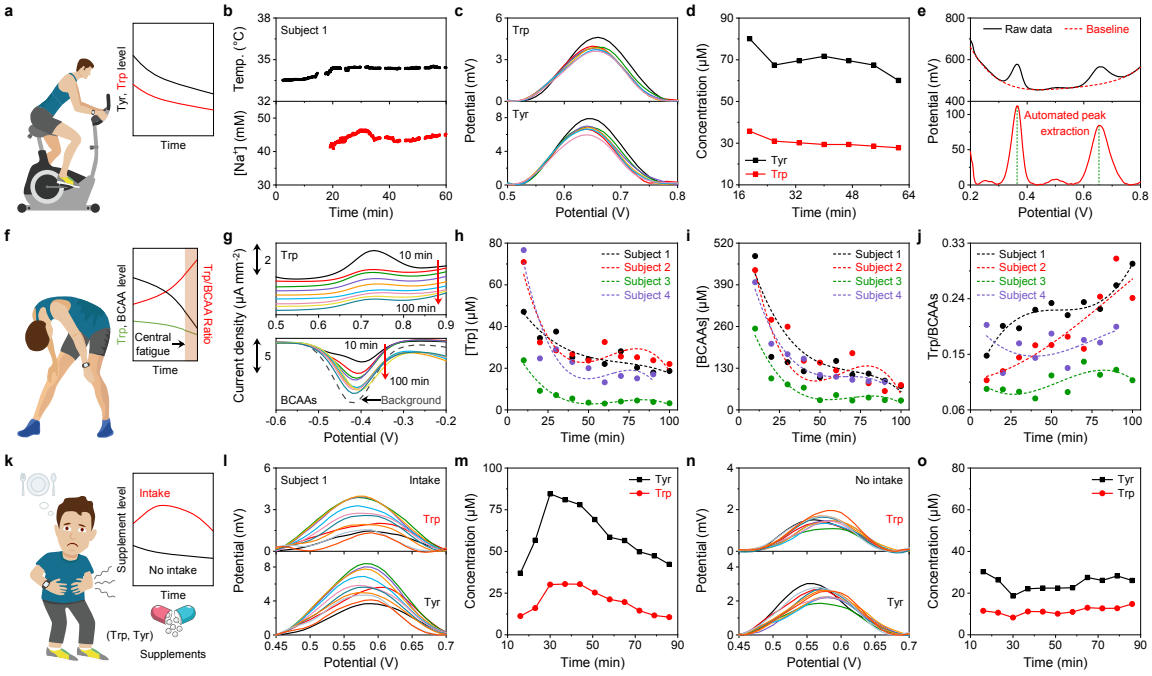

Figure 5-6. Wearable system evaluation across activities toward prolonged physiological and nutritional monitoring. a–d, Continuous on-body Trp and Tyr analysis using a wearable sensor array with real-time sensor calibrations during cycling exercise. **e**, Custom voltammogram analysis with an automatic peak extraction strategy based on a polynomial fitting and cut-off procedure. **f–j**, Dynamic sweat Trp and BCAA analysis during physical exercise toward central fatigue monitoring. **k–o**, Dynamic analysis of sweat AA levels with and without Trp and Tyr supplement intake at rest toward personalized nutritional monitoring.

Considering that AAs (e.g., Try and BCAAs) play a crucial role in central fatigue during physical exercise[9], a flexible Trp and BCAA sensor array was used to monitor the AA dynamics during vigorous exercise (**Fig. 5-6f–j** and **Fig. 5-7**). Both Trp and BCAA levels decreased during the exercise due to the serotonin synthesis and BCAA ingestion, respectively. The increased sweat Trp/BCAA ratio was observed which could potentially serve as an indicator for central fatigue, in agreement with a previous report on its plasma counterpart[9].

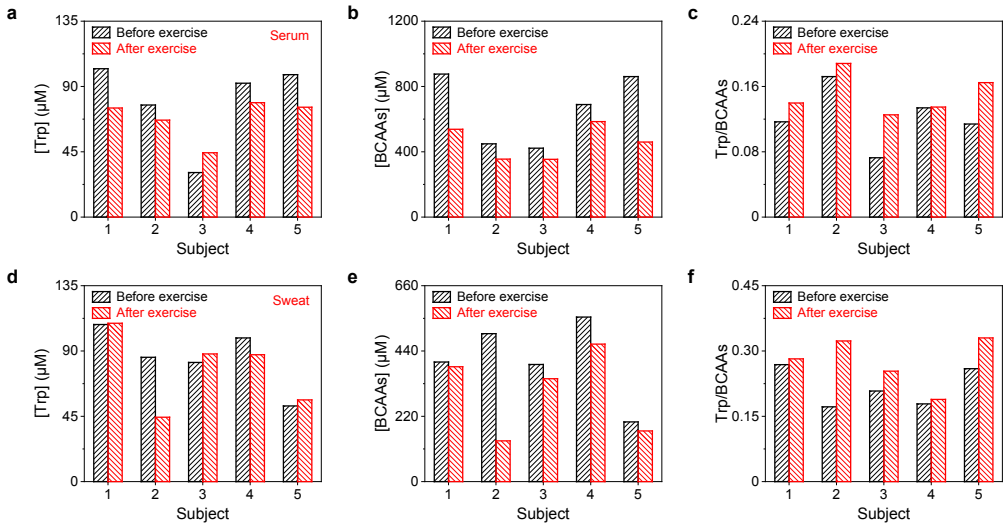

Figure 5-7. Dynamic monitoring of central fatigue using the Trp/BCAA sensor array patches. **a–c**, BCAA (**a**), Trp (**b**) and Trp/BCAA ratio (**c**) before exercise and after vigorous exercise until fatigue in human serum. **d–f**, BCAA (**d**), Trp (**e**) and Trp/BCAA ratio (**f**) before exercise and after vigorous exercise until fatigue in iontophoresis sweat.

The wearable iontophoresis-integrated patch enables daily continuous AA monitoring at rest beyond the physical exercise. As illustrated in **Fig. 5-6k–o** and **Appendix D, Figs. D-5-7**, rising Trp and Tyr levels in sweat were observed from all four subjects after Trp and Tyr supplement intake while the readings from the sensors remained stable during the studies without intake (**Fig. 5-8**). Such capability opens the door for personalized nutritional monitoring and management through

personalized sensor-guided dietary intervention. It should be noted that our pilot study showed that sweat nutrient and electrolyte levels were independent of sweat rate changes during the carbachol-based iontophoresis-induced sweat (**Appendix D, Fig. D-8**).

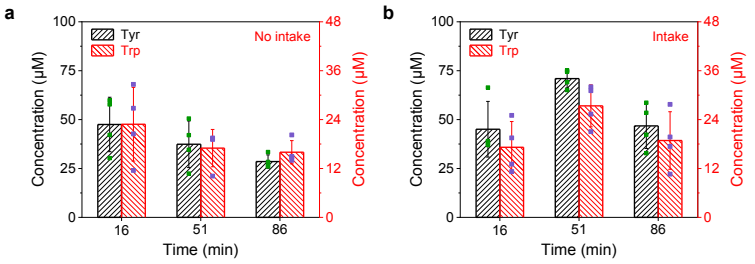

Figure 5-8. Tyr and Trp levels in continuous on-body Trp and Tyr sensing using wearable sensor arrays with and without supplement intake. Bars indicate the mean value of target; error bars represent the s.d. of measurements from all the subjects (n= 4).

5.3 Application of Wearable Sweat Sensors toward Gout and Metabolic Syndrome Management

Metabolic profiling and monitoring are a key approach to enabling precision nutrition and precision medicine.[10] Current gold standards in medical evaluation and metabolic testing heavily rely on blood analyses that are invasive and episodic, often requiring physical visits to medical facilities, labor-intensive sample processing and storage, and delicate instrumentation (for example, gas chromatography–mass spectrometry (GC–MS)).[11] As the current COVID-19 pandemic remains uncontrolled around the world, there is a pressing need for developing wearable and telemedicine sensors to monitor an individual's health state and to enable timely intervention under home- and community-based settings[12–14]. The progression from blood analyses to wearable sweat analyses could provide great potential for non-invasive, continuous monitoring of physiological biomarkers critical to human health. However, most clinically relevant nutrients and metabolites in sweat are rarely explored and undetectable by

existing wearable sensing technologies. In this section, we evaluated the use of sweat biomarkers for gout and metabolic syndrome management.

5.3.1 Gout Management

5.3.1.1 Introduction

As the global burden of gout is rising, management and treatment of gout have become a significant task.[15] Gout is often characterized by chronic hyperuricemia, an elevated UA level exceeding the physiological saturation threshold[16]. For gout patients, many risk factors, such as an increased intake of dietary purines and alcohol[17], can lead to gout attacks due to increased UA level in serum (Fig. 9a). Monitoring serum uric acid plays a crucial role in personalized gout treatment and management (e.g., urate-lower therapy, flare-up preventions, and dietary/nutritional control)[16]. The following sections delineate our effort in evaluating sweat UA toward non-invasive UA monitoring for gout management.

5.3.1.2 Methods

To evaluate the sensor performance toward gout management, a purine-rich diet study was performed on both healthy male and female subjects (**Fig. 5-9b-e** and **Appendix D, Fig. D-9**). The subjects reported to the lab after overnight fasting. Fresh capillary blood samples were collected using a finger-prick approach before the exercise. After cleaning the fingertip with alcohol wipe and allowing it to air dry, the skin was punctured with CareTouch lancing device. Samples were collected with centrifuge tubes after wiping off the first drop of blood with gauze. After the 90-min standardized clotting procedure finished, serum was separated by centrifuging at 6,000 rpm for 15 min, and instantly stored at −20 °C for HPLC analysis. A 20-min constant-load cycling exercise was immediately conducted on the subjects after the blood collection with the sweat information collected by the sensor patch from the forehead. The subjects were then given a purine-rich diet (250 g of canned sardines) followed by a 2-h rest. The blood collection and the cycling trial were then repeated. The plotted data for this study are based on the

first two successive complete DPV measurements. To further characterize the sweat UA sensing, six patients with gout, four subjects with hyperuricemia (without history of gout attack) and five healthy subjects were recruited (**Fig. 5-9f**). It should be noted that all of the six patients with gout (three currently under urate-lowering therapy, three not on any medical therapy) didn't receive any urate-lowering medication for at least 10 h ahead of the study. The sweat samples and blood samples were collected 2 h after their regular lunch and tested by the sensor patches and HPLC, respectively (same procedure as the after meal test in the meal challenge study). During the on-body test, sweat samples were collected periodically from the subjects using centrifuge tubes and then frozen at −20 °C for further sensor validation via HPLC analysis. For dynamic monitoring of UA before and after purine intake (**Fig. 5-9g**), a healthy subject underwent a finger-prick blood collection followed by a 20-min cycling test after overnight fasting, then consumed canned sardines. The blood collection and sweat test were repeated periodically every hour until 6 h after the intake. The collected blood samples were analyzed with HPLC. To investigate the medication influence on serum and sweat UA levels, a patient with gout underwent the sweat and blood sample tests on two days: on one day the patient received urate-lowering medication (allopurinol) 2 h before the test and on the other day the patient did not take medication for 24 h before the test. The sweat samples and blood samples were collected 2 h after their regular lunch and tested by the sensor patches and HPLC, respectively (same procedure as the after meal test in the meal challenge study). The correlation plot in **Fig. 9h** was based on data obtained from 15 subjects (including six patients with gout). The Pearson correlation coefficient was acquired through linear regression in Origin 2018 ($n = 46$).

5.3.1.3 Results and Discussion

To evaluate our sensor for gout management, we performed a controlled purine-diet study in healthy male and female subjects. For subjects with overnight fasting ($n = 6$), both serum and sweat UA levels increased after a purine-rich diet (**Fig. 9b-**

e and **Appendix D, Fig. D-9**). The subsequent human study, carried out 2 h after a regular lunch, indicated that higher sweat UA levels were identified from the subjects with hyperuricemia ($n = 4$) and patients with gout (without medication, $n = 6$) than from the healthy subjects ($n = 5$), with a similar trend in serum UA levels (**Fig. 5-9f** and validated in **Appendix D, Fig. D-10**, **Note D-2** with HPLC). This approach also shows promise for personalized dosage adjustment in urate-lowering therapy, as illustrated in **Fig. 5-10**. The dynamic changes of sweat UA before and after a purine-rich diet over a 7-h period measured by the wearable sensor (**Fig. 5-9g**) closely resembled those of serum UA. We obtained a high correlation coefficient of 0.864 between sweat and serum UA concentrations (**Fig. 5-3h**), suggesting the potential use of sweat UA as a biomarker for gout management.

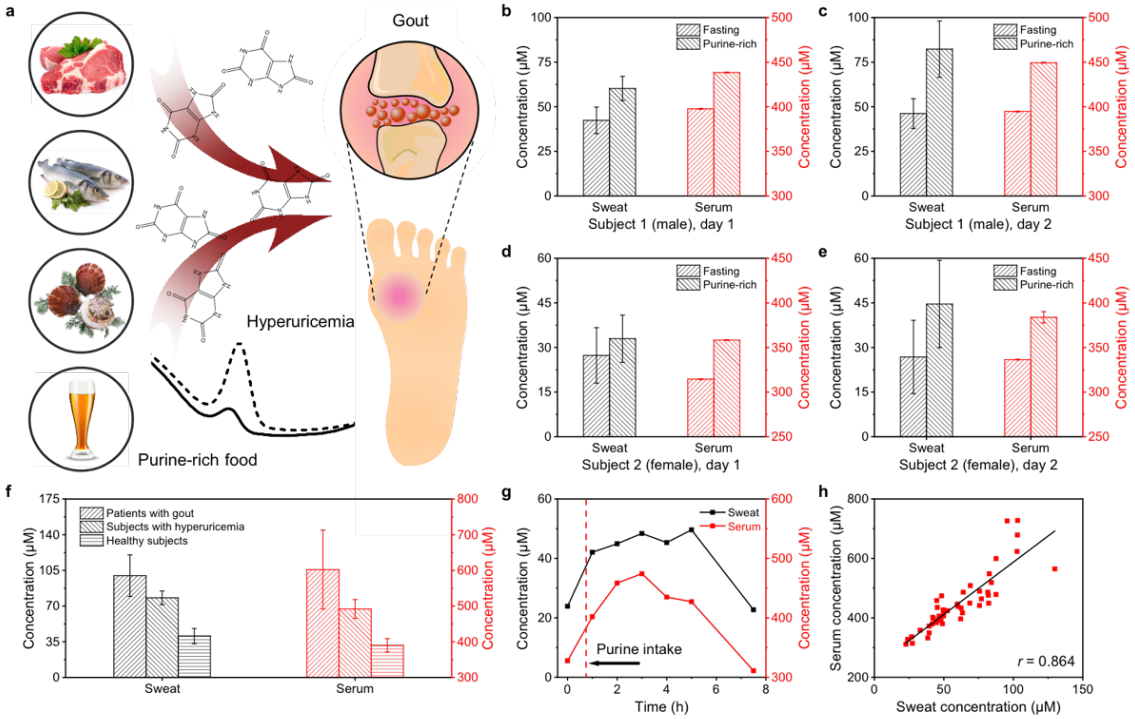

Figure 5-9. Non-invasive gout management with the sweat sensor. **a**, Purine-rich diets increase the risk of gout attacks. **b**–**e**, UA levels in sweat and serum of a healthy male (**b**,**c**) and a healthy female (**d**,**e**) subject under fasting condition, and after a purine-rich diet on two different days. Bars in **b**–**e** indicate the mean value of the first two successive measurements. **f**, The sweat and serum UA levels obtained using the

wearable sensors in patients with diagnosed gout, subjects with hyperuricemia and healthy individuals. Bars indicate the mean value of each category; error bars represent the s.d. of measurements from all the subjects in each category ($n = 6$ for patients with gout, $n = 4$ for subjects with hyperuricemia and $n = 5$ for healthy subjects). **g**, Dynamic changes of sweat and serum UA from one healthy subject before and after a purine-rich diet over a 7-h period. The experiment was repeated twice independently with similar results. **h**, The correlation of sweat and serum UA concentrations from the human studies. The Pearson correlation coefficient was acquired through linear regression ($n = 46$ biologically independent samples).

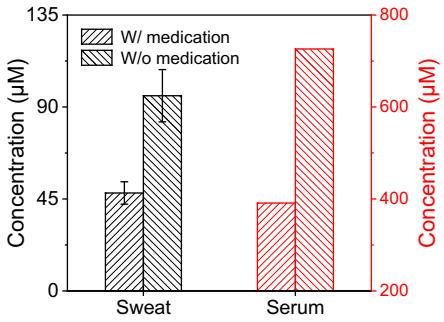

Figure 5-10. The influence of urate-lowering medication (allopurinol) on the sweat and serum UA levels. The sweat and blood tests were performed on the same gout patient on two days: on one day the patient received urate-lowering medication 2 hours before the test, and on the other day the patient did not take medication 24 hours before the test. Error bars represent the standard deviations of the first two successive measurements.

5.3.2 Non-invasive Monitoring of Metabolic Syndrome

5.3.2.1 Introduction

As the current COVID-19 pandemic remains uncontrolled around the world, there is a pressing need for developing wearable and telemedicine sensors to monitor an individual's health state and to enable timely intervention under home- and community-based settings[12–14]; it is also increasingly important to monitor a person's long-term cardiometabolic and nutritional health status after recovery

from severe COVID-19 infection using wearables to capture early signs of potential endocrinological complications such as T2DM.[18]

Metabolic syndrome, a metabolic disorder defined as glucose intolerance, obesity, hypertension and dyslipidemia, is a risk factor for atherosclerotic cardiovascular disease (ASCVD) and type 2 diabetes (T2DB)[19,20]. It doubles risk for ASCVD and increases risk for T2DB fivefold[20], and recent studies found that metabolic syndrome is associated with a significant risk of sudden cardiac death[21]. The prevalence of metabolic syndrome ranges from 10% to 40% worldwide, with a prevalence of 33% in the U. S.[19,22] The development of metabolic syndrome could be genetic and epigenetic, with risk factors such as central obesity, physical inactivity, and insulin resistance[19,23]. Despite chronic screening of the metabolic diseases, it is still of urgent need to detect and monitor the metabolic biomarkers, and an effective nutritional treatment could be personalized from different dietary interventions to ameliorate symptoms such as inflammation, glucose intolerance, etc.[24]

Branched-chain amino acids (BCAAs), including leucine, isoleucine, and valine, are essential amino acids usually associated with benefits on regulating body weight, muscle protein synthesis and glucose homeostasis. Many observational studies have concluded that elevated circulating BCAAs levels are associated with poor metabolic health. Specifically, increases in BCAAs are consistently observed in insulin-resistant obesity and Type 2 diabetes mellitus (T2DM) in both human patients and rodent models and have been linked to cardiovascular disease and metabolic syndrome[25–28] (**Fig. 5-11a**). Elevated blood BCAA levels are correlated positively with insulin resistance and HbA1c in various clinical studies[29–31], some of which reported that increase in blood BCAA levels are predictive of future insulin resistance or T2DM[32,33]. Despite all these findings, it is still unclear if BCAAs are the cause of IR and T2DM or a representative biomarker of impaired insulin action[34]. Some proposed that increased plasma BCAAs levels could be attributed to decreased BCAA metabolism in fat[29,35–37] and insulin resistance was

shown to correlate with reduced BCAA catabolic enzyme gene expression[29,38]. In addition, two mechanisms have been proposed for a causative link between increased plasma BCAAs levels and T2DM/IR. One proposed that elevated serum BCAAs level leads to persistent activation of rapamycin complex 1 signaling pathway, which uncouples insulin receptor from insulin signaling mediator and causing insulin resistance[25,29,39,40]. The other proposed that abnormal BCAA metabolism causes accumulated BCAA metabolites that trigger T2DM/IR-associated mitochondrial dysfunction and stress signaling[29,41]. Recent studies have shown the potential use of BCAAs supplementation as dietary intervention to ameliorate insulin resistance[42]. Monitoring changes in essential nutrient levels provides a highly sensitive early detection of metabolic syndrome risks, enabling effective personalized dietary intervention (**Fig. 5-11b**). In the following sections, we evaluate the use of sweat BCAA levels towards metabolic syndrome management.

Recently, various correlation analyses were performed on metabolites and COVID-19 severity. Increased leucine and phenylalanine showed a consistently significant association with COVID-19 severity and increased tyrosine showed notable association with COVID-19 severity[43]. The findings also suggested that for the severe COVID-19 cases, BCAAs accumulation in serum occurs in favor of cytosolic aerobic glycolysis[43]. Moreover, cytokine release syndrome, a major cause of the multi-organ injury and fatal outcome induced by SARS-CoV-2 infection, was found to be potentially modulated by metabolic interventions. Specifically, 14 inflammatory cytokines linked to CRS in severe patients were strongly correlated with tryptophan, and the decreased tryptophan and increased kynurenine reflect the hyperactivation of rate-limiting enzyme IDO1, which is reportedly involved in regulating hyperinflammatory responses[44]. Considering that circulating elevated Leu has been reported as a key metabolic fingerprint for the COVID-19 severity, we also evaluated our biosensors for analyzing the samples from patients with COVID-19 and healthy individuals in the following sections.

5.3.2.2 Methods

The validation and evaluation of the sweat sensor were performed using human subjects in compliance with all the ethical regulations under protocols (ID 19-0892 and 21-1079) that were approved by the institutional review board at California Institute of Technology. The participating subjects (aged over 18 years) were recruited from the California Institute of Technology campus and the neighbouring communities through advertisement. All subjects gave written informed consent before study participation. For wearable sensor evaluation, healthy subjects with a body mass index (BMI) of 18.5–24.9 kg m^{-2} with fasting serum glucose <100 mg dl^{-1} were recruited. For the BCAA study, inclusion criteria include: group I, individuals with normal weight who have a BMI of 18.5–24.9 kg m^{-2} with fasting serum glucose <100 mg dl^{-1} (healthy); group II, individuals with overweight/obesity who have a BMI of 25–35 kg m^{-2} and fasting serum glucose <6 mg dl^{-1} (overweight/obesity); group III, individuals with obesity who have a BMI of 25–35 kg m^{-2} and fasting serum glucose ≥126 mg dl^{-1} (obesity and T2DM). COVID-19-positive and COVID-19-negative serum samples were purchased from RayBiotech.

For the BCAA studies, the subjects were asked to consume 5 g BCAAs (2:1:1 Leu:Ile:Val) or a standardized snack including a protein drink (Fairlife, Core Power Elite) and a CLIF energy bar. An iontophoresis session was implemented with carbachol gels for sweat induction. Over the entire study period, the subject's sweat was sampled periodically and analysed by the sensor patch. Blood glucose level was recorded every 15 min with a commercial Care Touch Blood Glucose Meter. Fresh capillary blood samples were collected using a finger-prick approach during the human studies. After cleaning the fingertip with alcohol wipe and allowing it to air dry, the skin was punctured with a CareTouch lancing device. Samples were collected with centrifuge tubes after wiping off the first drop of blood with gauze. After the 90-min standardized clotting procedure finished, serum was separated by

centrifuging at 6,000 rpm for 15 min, and instantly stored at −20 °C for analysis with GC–MS, the LEG–MIP sensors and the custom insulin assay.

For the BCAA diet challenge study, the collected serum samples were analysed using a custom insulin sandwich immunoassay. The MBs were modified on the basis of a previous publication.[45] Briefly, 3 µl MBs were activated with 50 mg ml^{-1} EDC/sulfo-NHS in MES buffer (25 mM, pH 5) for 35 min followed by capture antibody immobilization (25 µg ml^{-1} in MES buffer) for 15 min. After de-activation with 1 M ethanolamine in phosphate buffer (0.1 M, pH 8), MBs were incubated in 25 µl standards prepared in 1% BSA or serum samples diluted five times in 1% BSA for 15 min. From here, the beads were rinsed with 1% BSA twice after each binding step. Next, the MBs were incubated in 25 µl of biotin-detector antibody (1.0 µg ml^{-1}) in 1% BSA for 30 min followed by 15 min in streptavidin–peroxidase conjugate (2,500×) prepared in 1% BSA. The amperometric detection was carried out by applying a constant potential of −0.2 V to MBs resuspended in 45 µl 1 mM hydroquinone, and 5 µl 5 mM H_2O_2 was pipetted onto the screen-printed carbon electrodes when background current stabilized.

5.3.2.3 Results and Discussion

To explore the use of sweat BCAAs as a non-invasive risk factor of metabolic syndrome, we performed a pilot study to investigate the correlations between serum and sweat BCAAs involving three groups of subjects: normal weight (I, $n = 10$), overweight/obesity (II, $n = 7$) and obesity with T2DM (III, $n = 3$) (**Fig. 5-11c,d**). Positive Pearson correlation coefficients of 0.66 ($n = 65$) and 0.69 ($n = 65$) were observed between sweat and serum levels (all analysed by the sensors) of Leu and total BCAA, respectively (**Fig. 5-11c**).

Compared with healthy participants in group I, substantially elevated sweat and serum Leu levels (analysed by the sensors) were observed in groups II and III (**Fig. 5-11d**), consistent with previous reports that higher circulating BCAA levels were identified in individuals with obesity and T2DM.[46] Considering the well-established role of BCAAs on insulin production and inhibition of glycogenolysis,

we also investigated the post-prandial response of sweat Leu/BCAAs and blood glucose/insulin after BCAA supplement and dietary intake in healthy subjects (**Fig. 5-11e,f**). All biomarkers remained stable during the fasting period; protein diet intake resulted in increases in both blood glucose and insulin, while BCAA intake only led to a rapid insulin increase. In both studies, sweat Leu and BCAAs first increased in the 30–60 min and then decreased. For subjects with different metabolic conditions, Leu levels in iontophoretic sweat after BCAA vary differently: although a substantial increase in sweat Leu levels was observed in all cases, healthy subjects showed a drastic percentage fluctuation and individuals with obesity/T2DM showed blunted fluctuation that may indicate the different metabolic stage of BCAA in those individuals (**Fig. 5-11g**).

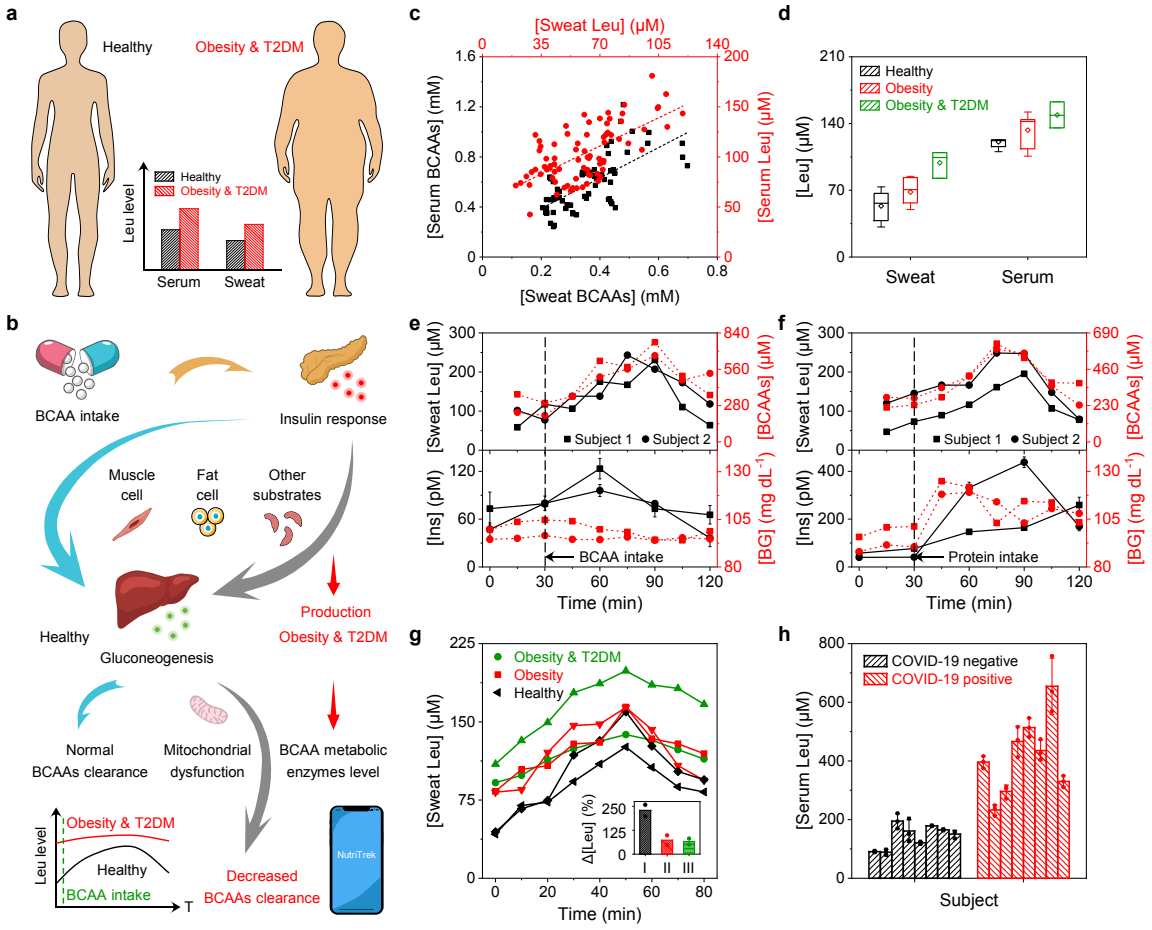

Figure 5-11. Personalized monitoring of metabolic syndrome risk factors using LEG–MIP BCAA sensors. a, Elevated BCAA levels identified in individuals with obesity and/or T2DM. b, The close associations between BCAA metabolism and insulin response in healthy and obesity/T2DM groups. c, Correlation of serum and sweat total BCAA and Leu levels obtained with the LEG–MIP sensors (n = 65). Dashed lines represent linear-fit trendlines. d, Box-and-whisker plot of measured Leu levels in iontophoresis-extracted sweat and serum in three groups of participants: normal weight (group I, n = 10), overweight or obesity (group II, n = 7) and obesity with T2DM (group III, n = 3), The bottom whisker represents the minimum, the top whisker represents the maximum and the square in the box represents the mean. e,f, Dynamic changes of sweat Leu and total BCAAs, serum insulin (Ins) and blood glucose (BG) levels from two healthy subjects with 5 g BCAAs (e) and standard protein diet (f) intakes. g, Sweat Leu dynamics collected from groups I–III after 5 g BCAA intake. Inset, ratio of the Leu level at 50 min after BCAA intake and the level before intake. h, Evaluation of Leu as a metabolic fingerprint for COVID-19 severity in serum samples from COVID-19-negative subjects (n = 8) and COVID-19-positive patients (n = 8). Error bars represent the s.d. from three measurements.

Considering that circulating elevated Leu has been reported as a key metabolic fingerprint for COVID-19 severity, we also evaluated our biosensors for analysing the samples from patients with COVID-19 and healthy individuals; substantially elevated Leu levels were identified in COVID-19-positive samples compared with the negative ones (415.6 ± 133.7 versus 151.5 ± 36.0 μM), indicating the great potential of our biosensors for at-home COVID-19 monitoring and management (**Fig. 5-11h**).

5.3.3 Conclusion

Metabolic profiling using wearable sensors has become increasingly crucial in precision nutrition and precision medicine, especially in the era of the COVID-19 pandemic, as it provides not only insights into COVID-19 severity but also guidance to stay metabolically healthy to minimize the risk of potential COVID-19

infection. As the pandemic remains rampant throughout the world and regular medical services are at risk of shortage, there is an urgent need to develop and apply wearable sensors that can monitor health conditions via metabolic profiling to achieve at-home diagnosis and timely intervention via telemedicine.

By integrating mass-producible LEG, multiplexed sensor array and system-level integration into a wireless wearable technology, with optimized multi-inlet microfluidic sweat sampling, in situ signal processing, calibration and wireless communication. Using this telemedicine technology, we have demonstrated the wearable and continuous monitoring of post-prandial UA and AA responses to identify risks for gout flareups and metabolic syndrome. The high correlations between sweat and serum BCAAs and between sweat and serum UA suggest that this technology holds great promise for use in metabolic syndrome risk and gout monitoring. The substantial difference in Leu between COVID-19-positive and COVID-19-negative blood samples indicates the potential of using this technology for at-home COVID-19 management. We envision that this wearable technology could play a crucial role in the realization of precision nutrition through continuous monitoring of circulating biomarkers and enabling personalized nutritional intervention. This technology could also be reconfigured to continuously monitor a variety of other biomarkers towards a wide range of personalized preventive, diagnostic and therapeutic applications.

Bibliography of Chapter 5

1. Kim, D.-H. *et al.* Epidermal Electronics. *Science* **333**, 838–843 (2011).
2. Someya, T., Bao, Z. & Malliaras, G. G. The rise of plastic bioelectronics. *Nature* **540**, 379–385 (2016).
3. Gao, W. *et al.* Fully integrated wearable sensor arrays for multiplexed in situ perspiration analysis. *Nature* **529**, 509–514 (2016).

4. Koh, A. *et al.* A soft, wearable microfluidic device for the capture, storage, and colorimetric sensing of sweat. *Science Translational Medicine* **8**, 366ra165-366ra165 (2016).
5. Lee, H. *et al.* A graphene-based electrochemical device with thermoresponsive microneedles for diabetes monitoring and therapy. *Nature Nanotechnology* **11**, 566–572 (2016).
6. Bariya, M., Nyein, H. Y. Y. & Javey, A. Wearable sweat sensors. *Nature Electronics* **1**, 160–171 (2018).
7. Emaminejad, S. *et al.* Autonomous sweat extraction and analysis applied to cystic fibrosis and glucose monitoring using a fully integrated wearable platform. Proceedings of the National Academy of Sciences of the United States of America **114**, 4625–4630 (2017).
8. Bandodkar, A. J. *et al.* Tattoo-based noninvasive glucose monitoring: a proof-of-concept study. *Analytical Chemistry* **87**, 394–398 (2015).
9. Newsholme, E. A. & Blomstrand, E. Branched-chain amino acids and central fatigue. *The Journal of Nutrition* **136**, 274S-276S (2006).
10. Wishart, D. S. Emerging applications of metabolomics in drug discovery and precision medicine. *Nature Reviews Drug Discovery* **15**, 473–484 (2016).
11. Dettmer, K., Aronov, P. A. & Hammock, B. D. Mass spectrometry-based metabolomics. *Mass Spectrometry Reviews* **26**, 51–78 (2007).
12. Ray, T. R. *et al.* Bio-integrated wearable systems: a comprehensive review. *Chemical Reviews* **119**, 5461–5533 (2019).
13. Hollander, J. E. & Carr, B. G. Virtually Perfect? Telemedicine for Covid-19. *New England Journal of Medicine* **382**, 1679–1681 (2020).
14. Ni, X. *et al.* Automated, multiparametric monitoring of respiratory biomarkers and vital signs in clinical and home settings for COVID-19 patients. *Proceedings of the National Academy of Sciences* **118**, e2026610118 (2021).
15. Smith, E. *et al.* The global burden of gout: estimates from the Global Burden of Disease 2010 study. *Annals of the Rheumatic Diseases* **73**, 1470–1476 (2014).

16. Terkeltaub, R. Update on gout: new therapeutic strategies and options. *Nature Reviews Rheumatology* **6**, 30–38 (2010).
17. Terkeltaub, R. A. Clinical practice. Gout. *New England Journal of Medicine* **349**, 1647–1655 (2003).
18. Stefan, N., Birkenfeld, A. L. & Schulze, M. B. Global pandemics interconnected — obesity, impaired metabolic health and COVID-19. *Nature Reviews Endocrinology* **17**, 135–149 (2021).
19. Grundy, S. M. Metabolic syndrome update. *Trends in Cardiovascular Medicine* **26**, 364–373 (2016).
20. Grundy Scott M. Metabolic syndrome pandemic. *Arteriosclerosis, Thrombosis, and Vascular Biology* **28**, 629–636 (2008).
21. Hess Paul L. *et al.* The metabolic syndrome and risk of sudden cardiac death: the atherosclerosis risk in communities study. *Journal of the American Heart Association* **6**, e006103.
22. Aguilar, M., Bhuket, T., Torres, S., Liu, B. & Wong, R. J. Prevalence of the metabolic syndrome in the United States, 2003-2012. *Journal of the American Medical Association* **313**, 1973–1974 (2015).
23. What is metabolic syndrome? *WebMD* https://www.webmd.com/heart/metabolic-syndrome/metabolic-syndrome-what-is-it.
24. Xu, H., Li, X., Adams, H., Kubena, K. & Guo, S. Etiology of metabolic syndrome and dietary intervention. *International Journal of Molecular Sciences* **20**, 128 (2019).
25. Newgard, C. B. *et al.* A branched-chain amino acid-related metabolic signature that differentiates obese and lean humans and contributes to insulin resistance. *Cell Metabolism* **9**, 311–326 (2009).
26. Newgard, C. B. Interplay between lipids and branched-chain amino acids in development of insulin resistance. *Cell Metabolism* **15**, 606–614 (2012).
27. Batch, B. C. *et al.* Branched chain amino acids are novel biomarkers for discrimination of metabolic wellness. *Metabolism* **62**, 961–969 (2013).

28. Huang, Y., Zhou, M., Sun, H. & Wang, Y. Branched-chain amino acid metabolism in heart disease: an epiphenomenon or a real culprit? *Cardiovascular Research* **90**, 220–223 (2011).

29. Lackey, D. E. *et al.* Regulation of adipose branched-chain amino acid catabolism enzyme expression and cross-adipose amino acid flux in human obesity. *American Journal of Physiology-Endocrinology and Metabolism* **304**, E1175–E1187 (2013).

30. Fiehn, O. *et al.* Plasma metabolomic profiles reflective of glucose homeostasis in non-diabetic and type 2 diabetic obese African-American women. *Plos One* **5**, e15234 (2010).

31. Badoud, F. *et al.* Serum and adipose tissue amino acid homeostasis in the metabolically healthy obese. *Journal of Proteome Research* **13**, 3455–3466 (2014).

32. Wang, T. J. *et al.* Metabolite profiles and the risk of developing diabetes. *Nature Medicine* **17**, 448–453 (2011).

33. McCormack, S. E. *et al.* Circulating branched-chain amino acid concentrations are associated with obesity and future insulin resistance in children and adolescents. *Pediatric Obesity* **8**, 52–61 (2013).

34. Lynch, C. J. & Adams, S. H. Branched-chain amino acids in metabolic signaling and insulin resistance. *Nature Reviews Endocrinology* **10**, 723–736 (2014).

35. She, P. *et al.* Obesity-related elevations in plasma leucine are associated with alterations in enzymes involved in branched-chain amino acid metabolism. *American Journal of Physiology-Endocrinology and Metabolism* **293**, E1552–E1563 (2007).

36. She, P. *et al.* Leucine and protein metabolism in obese zucker rats. *Plos One* **8**, e59443 (2013).

37. Adams, S. H. Emerging perspectives on essential amino acid metabolism in obesity and the insulin-resistant state. *Advances in Nutrition* **2**, 445–456 (2011).

38. Stančáková, A. *et al.* Hyperglycemia and a common variant of GCKR are associated with the levels of eight amino acids in 9,369 Finnish men. *Diabetes* **61**, 1895–1902 (2012).

39. Um, S. H. *et al.* Absence of S6K1 protects against age- and diet-induced obesity while enhancing insulin sensitivity. *Nature* **431**, 200–205 (2004).

40. Um, S. H., D'Alessio, D. & Thomas, G. Nutrient overload, insulin resistance, and ribosomal protein S6 kinase 1, S6K1. *Cell Metabolism* **3**, 393–402 (2006).

41. Olson, K. C., Chen, G., Xu, Y., Hajnal, A. & Lynch, C. J. Alloisoleucine differentiates the branched-chain aminoacidemia of Zucker and dietary obese rats. *Obesity* **22**, 1212–1215 (2014).

42. Layman, D. K. & Walker, D. A. Potential importance of leucine in treatment of obesity and the metabolic syndrome. *The Journal of Nutrition* **136**, 319S-323S (2006).

43. Dierckx, T. *et al.* The metabolic fingerprint of COVID-19 severity. http://medrxiv.org/lookup/doi/10.1101/2020.11.09.20228221 (2020) doi:10.1101/2020.11.09.20228221.

44. Xiao, N. *et al.* Integrated cytokine and metabolite analysis reveals immunometabolic reprogramming in COVID-19 patients with therapeutic implications. *Nature Communications* **12**, 1618 (2021).

45. Torrente-Rodríguez, R. M. *et al.* Rapid endoglin determination in serum samples using an amperometric magneto-actuated disposable immunosensing platform. *Journal of Pharmaceutical and Biomedical Analysis* **129**, 288–293 (2016).

46. Lynch, C. J. & Adams, S. H. Branched-chain amino acids in metabolic signaling and insulin resistance. *Nature Reviews Endocrinology* **10**, 723–736 (2014).

A p p e n d i x D

SUPPLEMENTARY INFORMATION FOR CHAPTER 5

Materials from this chapter appears in "Yang, Y.; Song, Y.; Bo, X.; Min, J.; Pak, O. S.; Zhu, L.; Wang, M.; Tu, J.; Kogan, A.; Zhang, H.; Hsiai, T. K.; Li, Z.; Gao, W. A laser-engraved wearable sensor for sensitive detection of uric acid and tyrosine in sweat. *Nature Biotechnology* **38**, 217–224 (2020) doi:10.1038/s41587-019-0321-x" and "Wang, M.; Yang, Y.; Min, J.; Song, Y.; Tu, J.; Mukasa, D.; Ye, C.; Xu, C.; Heflin, N.; McCune, J. S.; Hsiai, T. K.; Li, Z.; Gao, W. A wearable electrochemical biosensor for the monitoring of metabolites and nutrients. *Nature Biomedical Engineering* 1–11 (2022) doi: 10.1038/s41551-022-00916-z".

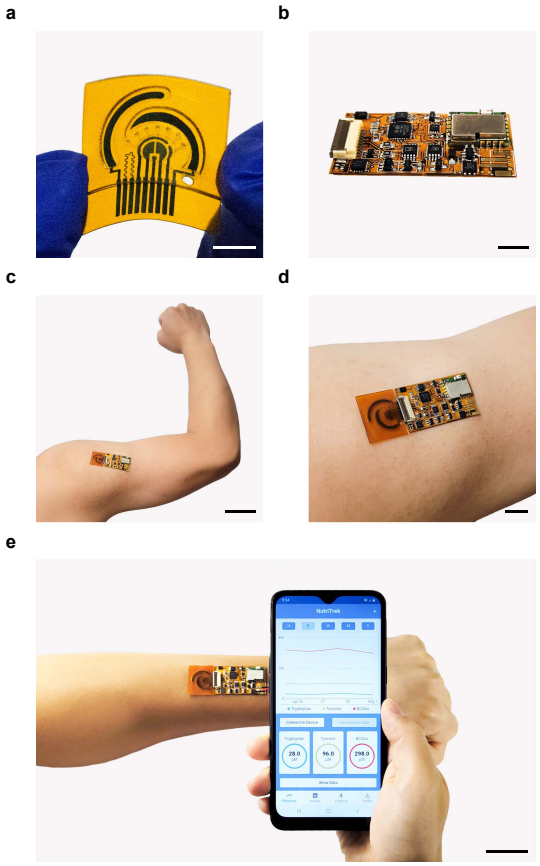

Figure D-1. Integrated flexible NutriTrek prototype for personalized nutritional monitoring. a,**b**, Optical photos of a wearable NutriTrek prototype consisting of a flexible, disposable microfluidic sensor patch (**a**) for autonomous sweat stimulation and sweat analysis and a flexible printed circuit board (FPCB) (**b**) for *in situ* electrochemical control, signal processing, and wireless communication. Scale bars, 5 mm (**a**) and 1 cm (**b**). **c**,**d**, Optical photos of the integrated system on the body. Scale bars, 5 cm (**c**) and 1 cm (**d**). **e**, Optical photo of a flexible NutriTrek patch interfacing with the custom cell phone app for real-time data collection. Scale bar, 3 cm.

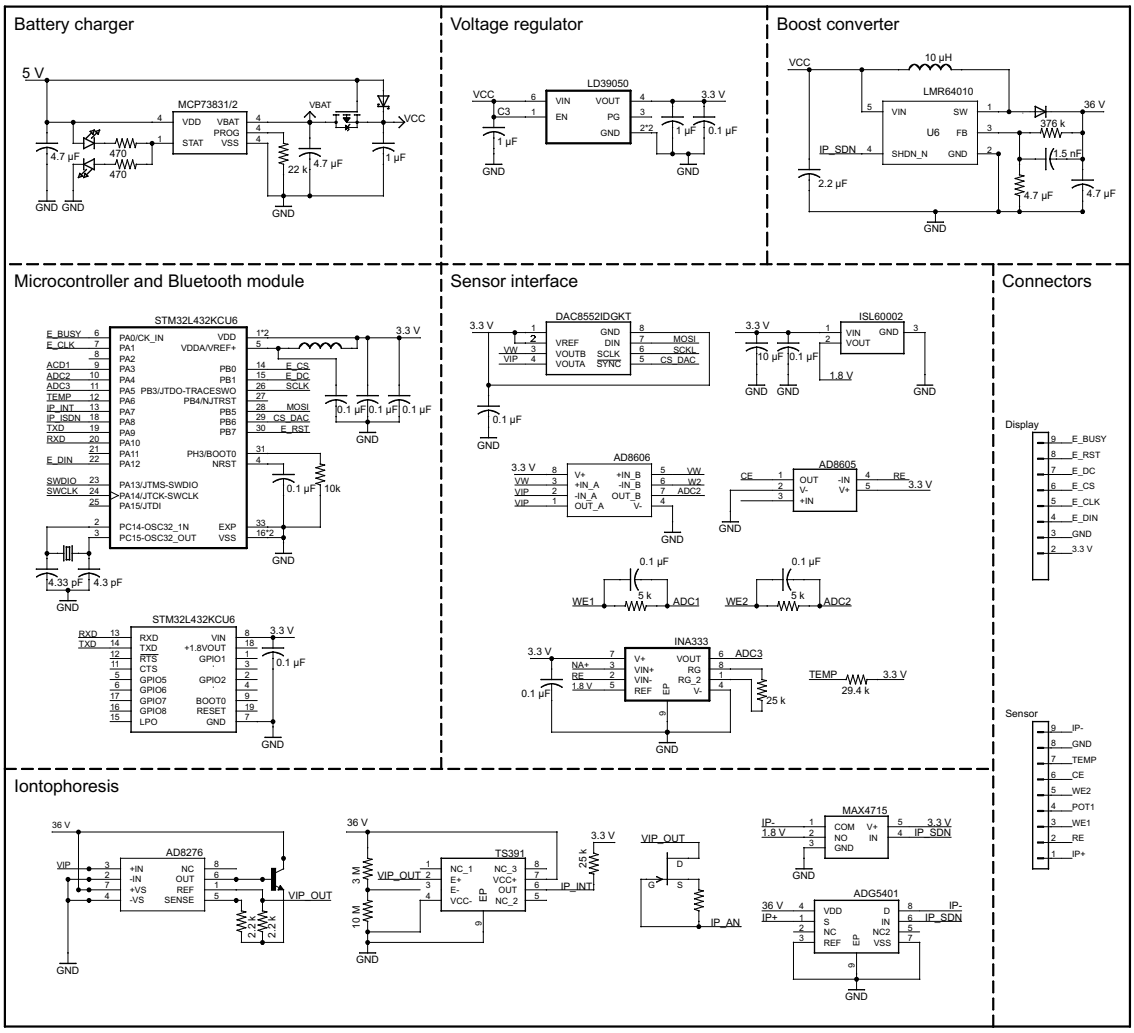

Figure D-2. The detailed circuit diagram of the NutriTrek.

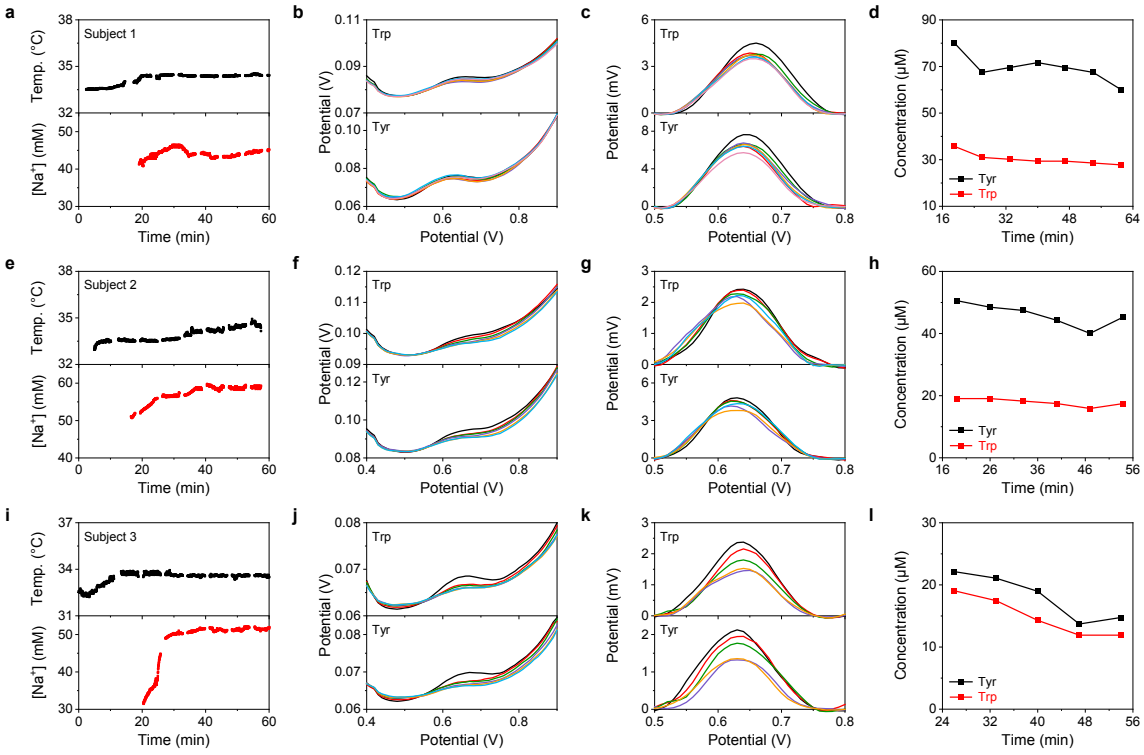

Fig. D-3. Continuous on-body Trp and Tyr analysis with real-time sensor calibrations using a wearable sensor array on three subjects during a constant-load cycling exercise. b,**f**,**j** represent the raw signals obtained from the on body measurement while **c**,**g**,**k** represent the corresponding data obtained with automated voltammogram analysis.

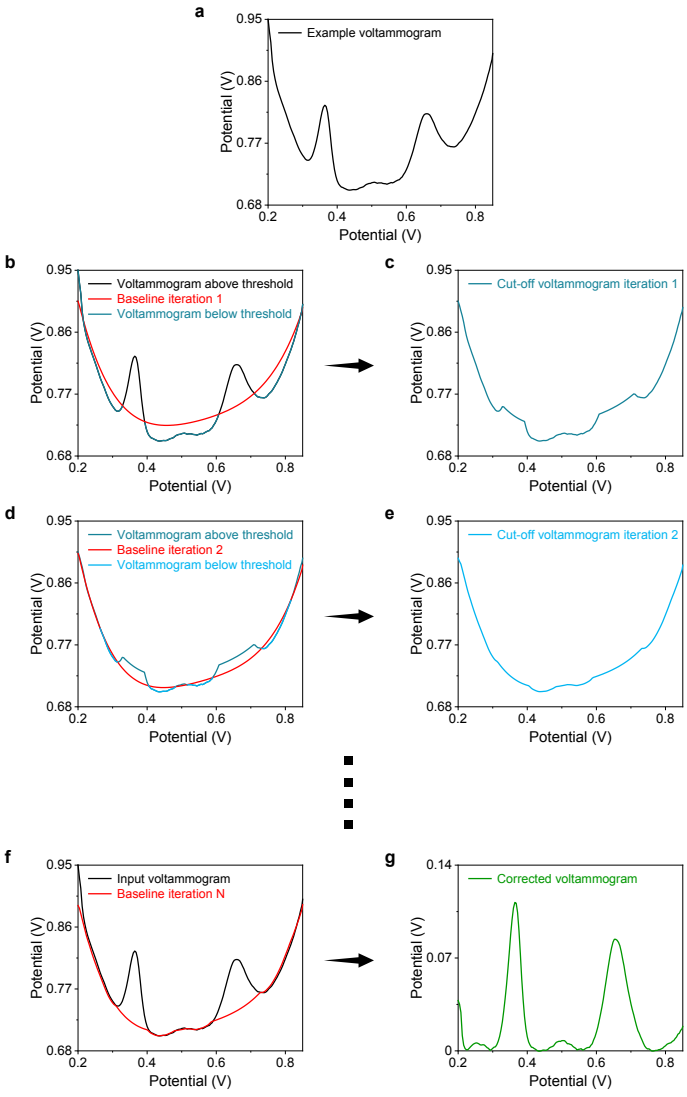

Figure D-4. Automated voltammogram analysis. A sample input voltammogram (**a**) is approximated by a polynomial baseline that acts as a threshold (**b**) for the input voltammogram. The voltammogram below the threshold is retained, while the voltammogram above the threshold is replaced by the polynomial baseline to generate the first iteration cut-off voltammogram (**c**). The polynomial fitting and cutting-off procedure is iterated a specified number of times (**d**,**e**). After the iterative baseline correction, the original input voltammogram is subtracted by the final baseline to yield a corrected voltammogram (**f**,**g**). A simple peak detection algorithm is employed to calculate the peak height and location of the corrected voltammogram.

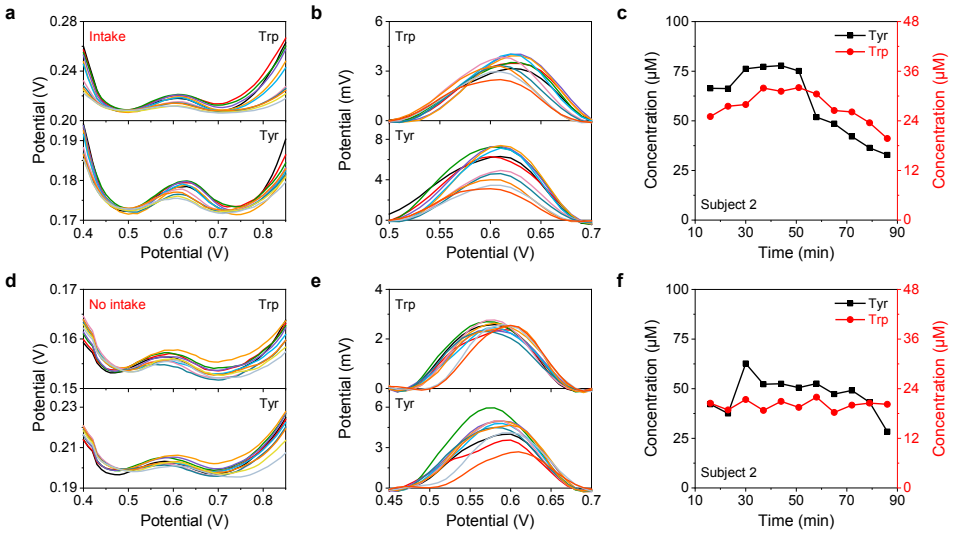

Figure D-5. Iontophoresis-based continuous on-body Trp and Tyr analysis using a wearable sensor array with and without supplement intake (Subject 2). **a–c**, The raw voltammograms (**a**), automatically corrected voltammograms (**b**), and calibrated biomarker trends (**c**) collected during an on-body study with the supplement intake (Trp and Tyr, 1 g each). **d–f**, The raw voltammograms (**d**), automatically corrected voltammograms (**e**), and calibrated biomarker trends (**f**) collected during an on-body study without the supplement intake.

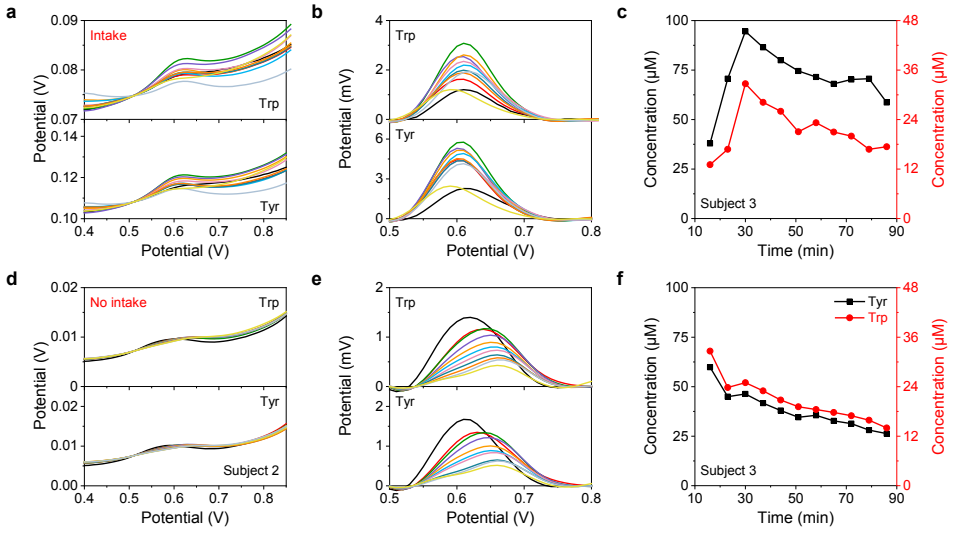

Figure D-6. Iontophoresis-based continuous on-body Trp and Tyr analysis using a wearable sensor array with and without supplement intake (Subject 3). **a–c**, The raw voltammograms (**a**), automatically corrected voltammograms (**b**), and calibrated biomarker trends (**c**) collected during an on-body study with the supplement intake (Trp and Tyr, 1 g each). **d–f**, The raw voltammograms (**d**), automatically corrected voltammograms (**e**), and calibrated biomarker trends (**f**) collected during an on-body study without the supplement intake.

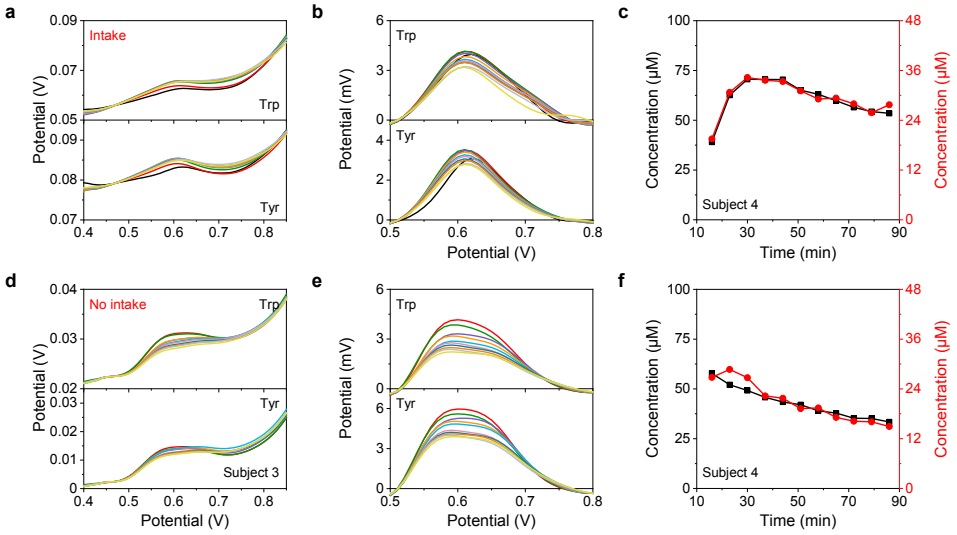

Figure D-7. Iontophoresis-based continuous on-body Trp and Tyr analysis using a wearable sensor array with and without supplement intake (Subject 4). **a–c**, The raw voltammograms (**a**), automatically corrected voltammograms (**b**), and calibrated biomarker trends (**c**) collected during an on-body study with the supplement intake (Trp and Tyr, 1 g each). **d–f**, The raw voltammograms (**d**), automatically corrected voltammograms (**e**), and calibrated biomarker trends (**f**) collected during an on-body study without the supplement intake.

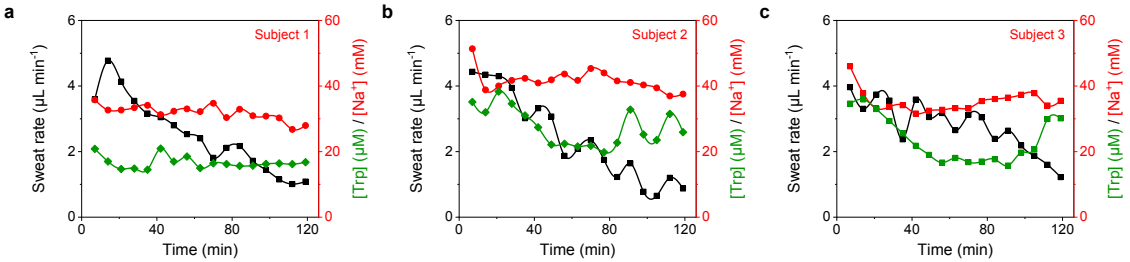

Figure D-8. Sweat rate and the concentrations of amino acids (Trp here) and Na^+ on human subjects. The sweat was induced with the proposed carbachol-based iontophoresis.

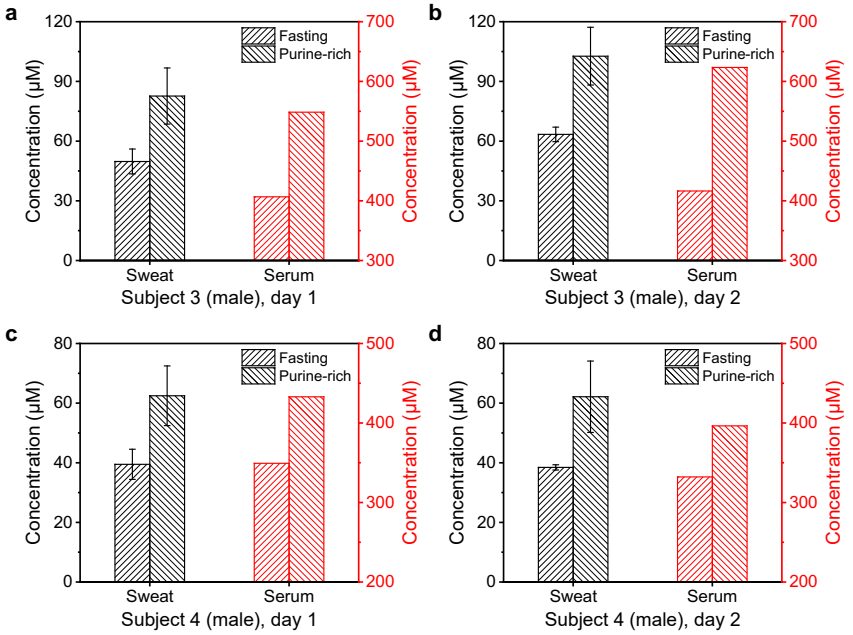

Figure D-9. Investigation of the sweat and serum UA levels using a purine-rich diet challenge. UA levels in sweat and serum of two heathy subjects under fasting condition, and after a purine-rich diet on two different days.

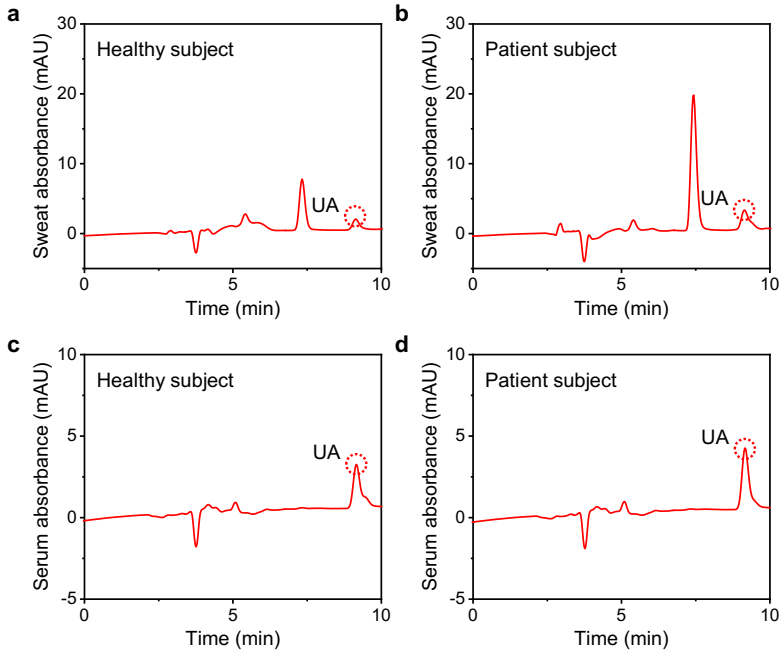

Figure D-10. HPLC analyses of the sweat (a,b) and serum (c,d) UA levels of a healthy subject (a,c) and a patient with gout (b,d).

Eluent A	Eluent B	Flow rate	Time (min)	Percentage eluent B (%)
0.1% Formic acid	Acetonitrile 100%	0.34 mL min^{-1}	0	0
			6	0
			6.2	100
			7.5	100
			7.9	0
			15	0

Table D-1. UA HPLC gradient method

Eluent A	Eluent B	Flow rate	Time (min)	Percentage eluent B (%)
50 mM KH_2PO_4-H_3PO_4 buffer pH 3.0	Methanol 100%	0.425 mL min^{-1}	0	9.1
			4	9.1
			8	80
			12	80
			15	9.1
			20	9.1

Table D-2. Tyr HPLC gradient method

Note D-1. Signal conditioning, processing and wireless transmission for the wearable sensor.

The sweat induction and the sweat sensing procedures are initiated and controlled by the microcontroller (STM32L432KC, STMicroelectronics) when it receives a user command from the Bluetooth module over Universal Asynchronous Receiver/Transmitter (UART) communication.

Sweat induction: Programmable iontophoretic current is generated by a voltage controlled current source that consists of a unity-gain difference amplifier (AD8276, Analog Devices) and a boost transistor (BC846, ON Semiconductor). The circuit is supplied by the output of a boost converter (LMR64010) that boosts the 3.7 V battery voltage to 36 V. The microcontroller controls the digital to analog converter (DAC) (DAC8552, Texas Instruments) over serial peripheral interface (SPI) to set the control voltage of the current source. The current source output is checked by a comparator (TS391, STMicroelectronics) and the microcontroller is interrupted through its general-purpose input/output (GPIO) pin at output failure. The protection circuit consists of a current limiter (MMBF5457, ON Semiconductor) and analog switches (MAX4715, Maxim Integrated; ADG5401, Analog Devices). The microcontroller's GPIO is also used to enable or disable the iontophoresis circuit. For the optimized design, a 100-μA current (~2.6 μA mm^{-2}) was applied for on-body iontophoresis sweat induction using the flexible microfluidic patch.

Power analysis: When powered at 3.3 V, the electronic system consumes ~28 mA during an active electrochemical measurement and ~61 mA during iontophoresis. The microcontroller and Bluetooth module each consume ~12 mA; the sensor interface consumes ~4 mA; the boost converter and iontophoresis module consumes ~33 mA, and the display module consumes an additional ~8 mA when refreshing its screen.

Sweat sensing: The sweat sensing circuitry can perform two channel simultaneous DPV, as well as potentiometric and temperature measurements. A bipotentiostat circuit is constructed by a control amplifier (AD8605) and two transimpedance

amplifiers (AD8606). A series voltage reference (ISL60002, Renesas Electronics) and a DAC (DAC8552, Texas Instruments) is used to generate a dynamic potential bias across the reference and working electrodes. In instrumentation amplifier (INA333, Texas Instruments) is used for potentiometric measurements; and a voltage divider is used for the resistive temperature sensor. All analog voltage signals are acquired by the microcontroller's built-in analog-to-digital converter (ADC) channels, processed, then transmitted over Bluetooth to a user device.

Custom mobile application design. The custom mobile application was developed with the cross-platform Flutter framework. The mobile application can wirelessly communicate with the wearable devices via Bluetooth to send commands, and to acquire, process, and visualize the sweat biomarker levels. The application establishes a secure Bluetooth connection to the wearable sensor. The home page plots the user's historical biomarker levels, and highlights the most recently measured analyte concentrations. When a sweat biomarker measurement is prompted, the user can switch over to the measurement page that plots the sweat sensors' voltammograms in real time. Following the voltammetric measurement, the app extracts the voltammograms' peak currents using a custom baseline correction algorithm, then converts the peak currents to corresponding biomarker concentrations. This measurement data is added to the list of historic analyte levels in the home page.

Note D-2. HPLC analysis for sensor validation and sample analysis.

HPLC tests of UA and Tyr were done on HP Agilent 1100 HPLC using an Agilent Eclipse XDB-C18 5 μm 3×250 mm column. Tests of UA and Tyr were done with gradient methods, and the gradient profiles are shown in **Tables D-1,2.** Detection wavelengths for UA and Tyr were 245 nm and 274 nm, respectively. Retention times were ~9 minutes and ~4 minutes for UA and Tyr, respectively. Sweat samples were diluted 3 times and serum samples were diluted 20 times, both with water.

Chapter 6

CONCLUSION AND FUTURE OUTLOOK

Materials from this chapter appear in "Min, J.; Tu, J.; Xu, C.; Lukas, H.; Shin, S.; Yang, Y.; Solomon, S.; Mukasa, D.; Gao, W. Skin-interfaced wearable sweat sensors for precision medicine. *Chemical Reviews*, Manuscript Submitted"

The fast progress in the development of sweat sensing platforms has opened the door for practical applications in non-invasive monitoring of fitness and health conditions. Early prototypes of wearable sweat sensors faced challenges in several aspects. First, the existent sensing strategies based on enzymes and ionophores limit the range of detection spectrum and sensitivity; second, previous prototypes relied on direct contact of flexible sensor electrode to the skin and can yield inaccurate sensing results due to contamination from skin, sweat evaporation and long refreshing time. Third, the manufacture procedure of previous prototypes was complex, including cleanroom fabrications which could be costly and time-consuming and limit the feasibility for mass production. Fourth, the lack of evaluation of sweat biomarkers for clinical conditions beyond cystic fibrosis hinders the wide application of wearable sweat sensing.

This thesis have summarized our efforts to tackle these challenges. Using mass-producible laser-engraving technique and differential pulse voltammetry, we have developed highly sensitive graphene sensors able to detect, for the first time, various electroactive targets (e.g. UA and Tyr) in sweat. Building on the pristine LEG, we developed MIP-based sensing strategies to further improve the sensor's selectivity in complex matrix and to widen the detection spectrum of the ultralow-level, non-electroactive metabolites. Besides chemical sensors, LEG-based strain sensor and temperature sensor were developed and consolidated in the same sensing patch to provide vital signs detection and calibration for real-time chemical sensing. In addition to graphene-based sensors, we used the laser-engraving technique to create efficient sweat induction and sampling microfluidics to enable fast refreshing for improved chronoaccuracy and on-demand sweat induction in sedentary individuals. With the multiplexed microfluidic sweat sensors, we have evaluated the use of sweat UA for gout management and the use of BCAAs for metabolic syndrome management.

While the aforementioned innovations helped to advance wearable sweat sensing, there are lingering and emerging challenges for future research and studies to resolve

before the eventual application of sweat sensing technology. Current sweat extraction technologies still suffer from large interpersonal variations or insufficiencies in sweat volume or sweat duration. In order to cope with the potential low sweat rates, fast-sampling microfluidics with low dead volume and miniaturized sensors with high sensitivity are necessary but yet to be achieved. While enzymatic sensors and ion-selective electrodes have been extensively developed for the detection of common sweat electrolytes and metabolites that are relatively high in concentration, many trace-level biomarkers including hormones and lipids are challenging to assess continuously with traditional sensing mechanisms. In addition to developing novel high-performance sensors, it is also important to improve selectivity and stability for long-term use in the complex fouling media and potential mechanical strains. For compact and robust system-integration, low-power and precise electronic circuitry should be coupled with a compact power source.

While sweat sensing technology has been significantly developed in the past decade, the sweat gland physiology, secretion and partitioning of the sweat metabolites are waiting more research efforts. Even with full understanding of the partitioning mechanism of a certain sweat metabolite, evaluation of such sweat biomarker for a clinical condition remains to be investigated at a larger scale considering inter-person and inter-group variations. The evaluation will undoubtedly become a multi-factor problem, and the use of big data and machine learning may help pool crucial factors together for a more comprehensive correlation of multi-biomarkers to the clinical condition at stake. However, with an influx of sensitive health data uploaded to the cloud, data privacy issues can arise. Additionally, considering that conventional von Neumann computing strategies are inefficient at processing large volumes of unstructured cloud data, neuromorphic edge computing technologies embedded in wearable devices have the potential to process data more securely and efficiently.

The previously illustrated challenges and considerations leave plenty of room for exciting future directions and opportunities for advancing the field of wearable sweat sensing. The continual research into the final product will undoubtedly unite concepts

and skills from various disciplines, from fundamental chemistry and materials innovations, practical device and system-level engineering, to physiological and clinical studies. Ultimately, the seamless integration of wearable sweat sensors into our daily life can be envisioned to enhance precision medicine and healthcare.